IMAGING COSMIC AND RARE UNDERGROUND SIGNALS

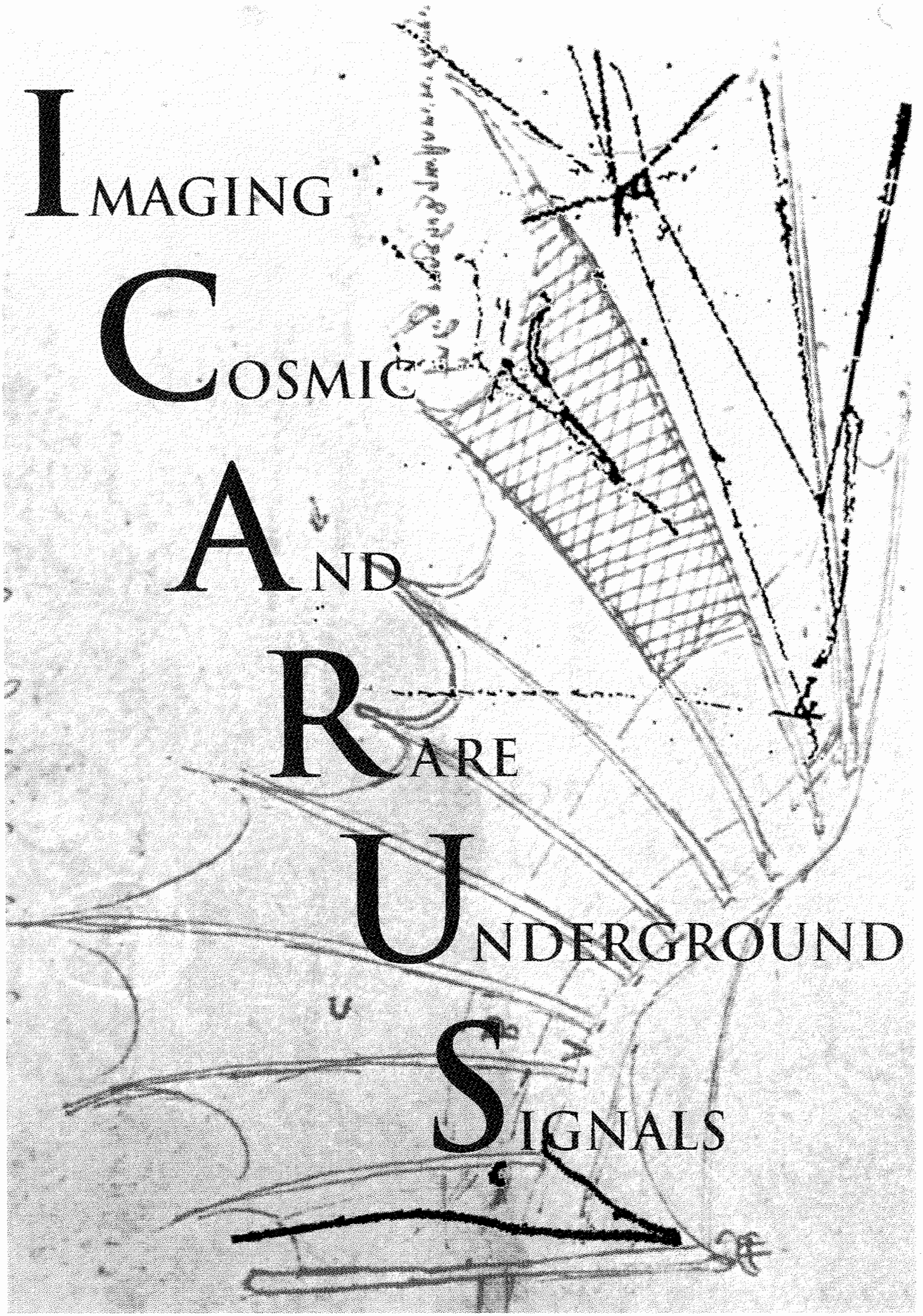

ICARUS II
A SECOND-GENERATION PROTON DECAY EXPERIMENT
AND
NEUTRINO OBSERVATORY AT THE GRAN SASSO LABORATORY

PROPOSAL

by the ICARUS Collaboration

Volume I

22 September 1993

P. Cennini, S. Cittolin, G.Maurin, A. Placci, J.P. Revol, C. Rubbia, W.H. Tian

CERN, CH-1211, Geneva 23, Switzerland

J.M. Ma, L.K. Ding, Y. Li, F. Lu, J.F. Qiu, H.Y. Sheng, K.L Tung, J.Y. Zeng, B. Zhang

Institute of High Energy Physics, Beijing, People's Republic of China

D. Giudice, X. Li, P. Picchi

Lab. Naz. di Frascati dell'INFN, via E.Fermi 40, Frascati (Roma), Italy

F. Cavanna, G. Piano Mortari, M. Verdecchia

Dipartimento di Fisica e INFN, Università dell'Aquila, via Vetoio, Coppito (AQ), Italy

D. Cline, S. Lazic, Y. Liu, G. Muratori, S. Otwinowski, J. Park, H.G. Wang, M. Zhou

Department of Physics, UCLA, Los Angeles, CA 90024, USA

A. Bettini, F. Casagrande, S. Centro, C. De Vecchi, A. Pepato, F. Pietropaolo, P. Rossi, S. Ventura

Dipartimento di Fisica e INFN, Università di Padova, via Marzolo 8, Padova, Italy

P. Benetti, E. Calligarich, S. Cesana, R. Dolfini, A. Gigli Berzolari, F. Mauri, C. Montanari, A. Piazzoli, A. Rappoldi, G.L. Raselli, D. Scannicchio, M. Terrani

Dipartimento di Fisica e INFN, Università di Pavia, via Bassi 6, Pavia, Italy

L. Periale, S. Suzuki

ICGF del CNR di Torino, corso Fiume 4, Torino, Italy

E. Feynyves

University of Texas at Dallas, Dallas, Texas, USA

CONTENTS

I. FOREWORD

The original ICARUS proposal was submitted eight years ago. Since then, the intense Research and Development activity has put on firm ground the detector technology, and experimentally confirmed the basic assumptions of the proposal. The ICARUS research programme involves the systematic study of a large spectrum of physical phenomena that cover many orders of magnitude in the energy deposited in the detector: from a few MeV for solar neutrino interactions, to the order of a GeV for the proton decay, and up to the very high energies of cosmic neutrinos. By 1988 it became clear to the Collaboration that such a complex and ambitious programme cannot be realized with a single, universal detector which is simultaneously optimized for all processes. It appeared to be necessary to design instead detectors with more specialized goals.

We then decided to present an update of the original proposal, dividing the programme in two steps. The first step, called ICARUS I, addressed the solar neutrino problem. As a consequence the detector was designed to operate in the few-MeV energy region, with the highest spatial resolution and the lowest background from radioactivity. Quoting from our proposal update, "*the second phase of the programme, ICARUS II, will involve the construction and operation of a much larger volume of argon, (several thousand tons), optimized to study proton decay with very high invariant mass resolution, and neutrino interactions coming from cosmic rays or from space with energy deposition above the radioactive noise*". In this second device a slightly worse spatial resolution could be accepted, in view of the expected long tracks of the order of a metre, and of the very large sensitive volume. Slightly relaxed purity (radioactivity) level requirements could be tolerated and cheaper components could also be used in the construction.

In the meantime, we have developed the detector technique to the point that we are now confident that we can build and operate a multi-kiloton detector. We therefore propose to go directly to the ultimate phase of the project.

The present document constitutes the first part of our ICARUS II proposal. In view of the numerous physics issues under consideration in our scientific programme, we have separated the proposal into two volumes:

Volume I

- The physics programme
- The results of the CERN 3-ton prototype tests

Volume II

- Engineering design
- Timetable
- Sharing of responsibility and cost

We should note in addition that the success of our prototype tests at CERN, together with the importance of the physics programme envisaged, have triggered renewed interest in the ICARUS project, resulting in a strengthening of the Collaboration.

II. INTRODUCTION

1. ICARUS: an innovative detector technology

Since the initial ICARUS proposal [1] and the subsequent update [2], intense activity in research and development has firmly established the technology of using ultra-pure argon, and the readout technique of ionization data, for very large sensitive volumes, first proposed in 1977 [3].

A 3-ton liquid-argon time projection chamber working as an electronic bubble chamber with the ability to provide 3D-imaging of any ionizing event, together with an excellent calorimetric response, has been operating successfully for more than two years. Results have been published in [4], and are reproduced in Chapter V of the present document.

The steady operation of our 3-ton prototype since May 1991 is a major milestone in the ICARUS programme. The first events (Figure 1) provided by cosmic rays immediately reminded us of Gargamelle-type bubble-chamber events, with a 'bubble' size of $2 \times 2 \times 2$ mm^3. The major breakthroughs are that the readout is entirely electronic, each bubble gives a measurement of the energy deposited by a particle, and the technique can be extended to very large active volumes. In particular, the device is continuously sensitive and self-triggering.

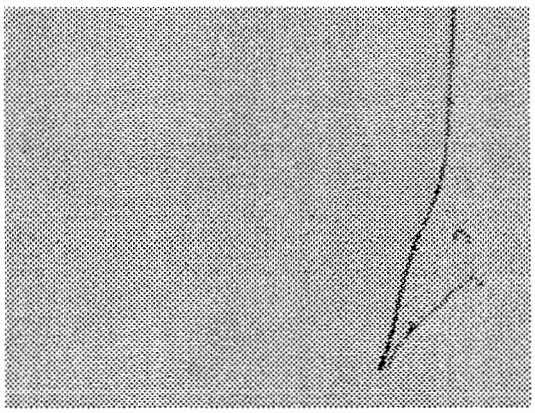

Figure 1a : Stopping muon with delayed decay electron. A Compton electron is also clearly visible. The drift direction is along the horizontal axis.

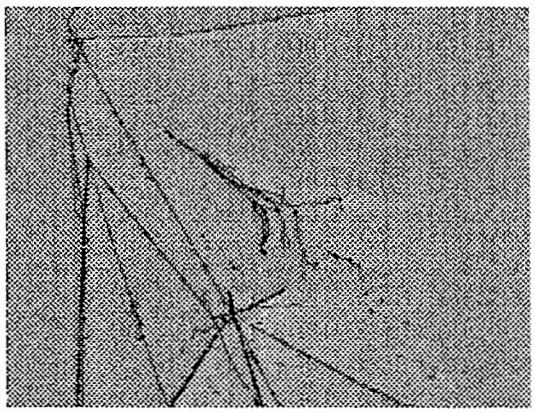

Figure 1b : Hadronic shower from a cosmic ray. A neutral particle (π^0/γ) produces an electromagnetic shower near the centre of the slide.

The main technological challenge was to adapt to a large-scale volume the techniques which had previously been established on a smaller scale, namely argon purification (less than 0.1 ppb of electronegative impurities is required), extreme cleanliness of the construction material employed, high reliability of feedthroughs to avoid leaks, the construction of high-precision wire planes able to resist thermal stresses, and the development of very low noise preamplifiers to collect small ionization charges.

The successful completion of the ICARUS R&D programme allows us now to define precisely the scientific scope of the full-scale experiment based on the construction and operation of a large volume of liquid argon (partitioned in three 5 000 ton modules) in the Gran Sasso tunnel.

2. Physics programme

The priority in the ICARUS programme at the Gran Sasso Laboratory goes to two main fundamental issues:

(a) the stability of the nucleon, which is the only way to access phenomena at the energy scale of Grand Unification. ICARUS will be the first high-resolution imaging study of such a phenomenon.

(b) the nature of neutrinos, in particular the question of the neutrino mass. This is being investigated in ICARUS both through the study of atmospheric neutrinos and through long baseline studies with a CERN neutrino beam (three orders of magnitude improvement in the length of baseline).

For all these issues the study can be done with a large safety margin since we are dealing with long tracks (of the order of a metre) and we are therefore not working at the edge of the detector capability. Also the background is not a critical issue since it can be easily controlled.

Even though ICARUS is not optimized to study solar neutrinos, the issue remains extremely interesting and therefore solar neutrinos are also an important part of our programme. The determination of the ultimate sensitivity of ICARUS depends, in this case, on the precise knowledge of the background from radioactive contaminants which will determine the detection threshold.

Finally astrophysical and cosmological neutrinos from supernova or any unexpected event which might occur during the lifetime ($\geq$ 10 years) of the experiment will deserve all our attention.

2.1 Proton decay

The question of baryonic matter stability is of paramount importance since it is directly linked to the understanding of the evolution and present state of our universe. For ordinary matter to dominate today over antimatter, the early universe must have been a gigantic scene of baryonic number violation. Cosmological theories require, at some level, transformation of initial energy into baryonic matter. Detailed balance considerations imply that, in principle, baryonic matter cannot live for ever. A simple practical conclusion is that the proton must decay. The proton lifetime is representative of the mass scale of the phenomenon responsible for the decay: $\tau_{decay} \sim M^4$. If the relevant scale is the Planck mass, about 10^{19} GeV, then the corresponding lifetime of the order of 10^{44} years would make it a hopeless case for observation by any human means. However, there are many reasons to believe that the relevant mass scale is in fact much lower. In particular, now that the electromagnetic, weak, and strong coupling constants have been measured with improved precision at LEP, it is clear that their extrapolation to large energies does not cross in one place [5] (Figure 2a). One simple remedy for this situation is to invoke a supersymmetric version of SU(5) (Figure 2b). Taking that approach, the SUSY particle mass scale may be in the TeV mass range, and as far as proton decay is concerned, the dominant decay mode would be $p \rightarrow \bar{\nu} K^+$ with a lifetime of 10^{32} to 10^{36} years. Therefore SUSY

Grand Unified Theories (GUTs) provide the next challenge for the proton decay searches.

Other models also exist, such as the Pati–Salam model [6], in which proton decay involves higher order diagrams with $\Delta(B-L) = -2$ and an energy scale as low as $10^{12\pm2}$ GeV, corresponding to proton lifetimes of 10^{30} to 10^{33} years. If this is the case, then why has proton decay not yet been observed? The answer may be an inadequate experimental technique. It has been argued recently, for instance, that the apparent anomalous atmospheric neutrino data from Kamiokande [7] and IMB-3 [8] may not be due to neutrino oscillations, a scenario which requires unexpectedly large mixing angles and large masses, but is rather a manifestation of proton decay [9]! The issue of proton decay, even for modest lifetimes, is therefore still entirely open and challenging.

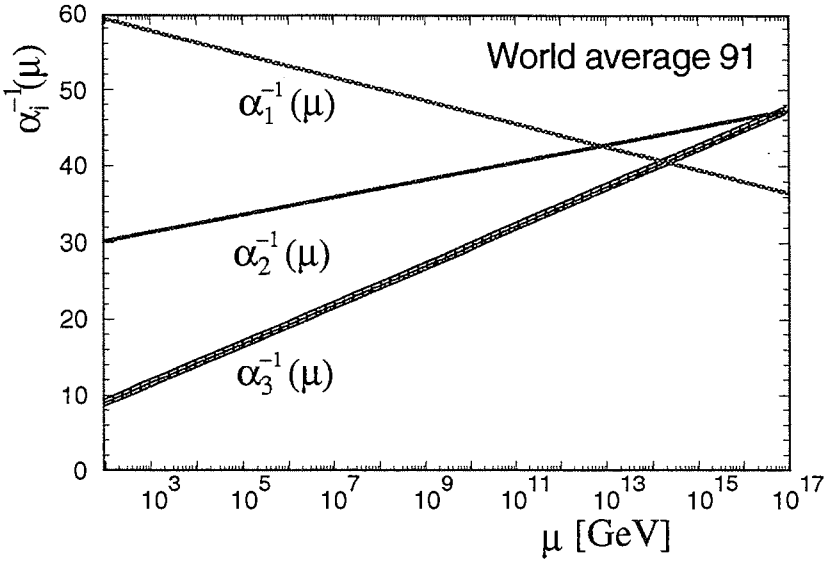

Figure 2a : Extrapolation of the weak, electromagnetic and strong coupling constants in the framework of the Standard Model. They miss one another by 9 standard deviations

Proton decay experiments with dedicated detectors started in the early 1980s, mainly motivated by the SU(5) GUT which predicted a lifetime of 10^{31} years for the dominant decay mode $p \rightarrow e^+\pi^0$. However, after a few years of data-taking, the lower limits obtained by the various experiments definitely ruled out the SU(5) model, extending the proton lifetime limit to a few times 10^{32} years, but at the same time exhausting the range of the experiments. A true second-generation experiment is therefore needed to explore the region of interest which may start as low as 10^{31} years if channels such as $p \rightarrow e^+ \nu \nu$ exist, and extend up to 10^{35} years if SUSY GUTs are the relevant theories.

Most theoretical ideas and models require some new, very high, intermediate mass scale. Such a mass scale most likely will never be reached with today's acceleration techniques. However, its role is absolutely fundamental in our understanding of the present elementary particle physics. Proton decay, if detectable, is probably the only way to explore experimentally the phenomenology at such high energies. Similarly to β decay and the study of neutral currents, which taught us almost everything

about the Standard Model, proton decay, if observed, would permit in a truly unique way, to study physics at the unification energy scale.

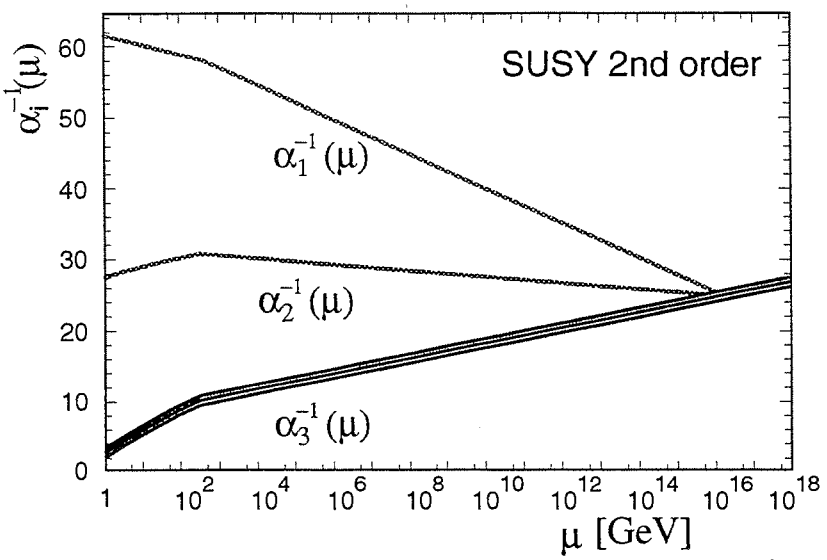

Figure 2b : Extrapolation of the weak, electromagnetic and strong coupling constants in the framework of the Minimal SUSY model. They naturally meet in one point

ICARUS is ideally suited to take up such a challenge by providing both a large sensitive mass (5 000 tons of liquid argon per module) and a new detector technique which can best be thought of as a modern version of the bubble chamber, using the electron drift imaging techniques developed by the Collaboration. As will be described in detail below, a proton decay will provide unambiguous, background-free, spectacular, metre-long tracks easy to reconstruct with superb particle identification. The proton decay search will be carried out in many exclusive channels, simultaneously. A clear advantage of the ICARUS technique is that discovery will be possible down to a single event, while any other existing or proposed experiment will have to rely on statistical background subtraction to eventually show the existence of a signal.

In view of the importance of the scientific issue at stake and armed with a technological breakthrough in experimental technique now to hand, the ICARUS Collaboration considers the search for the proton decay as the priority of the experiment.

2.2 Neutrino physics

Even though proton decay in itself justifies fully the ICARUS effort, several other important physics issues will also be studied concurrently.

2.2.1 Atmospheric neutrino studies

Since the original suggestion by Pontecorvo [10] of the possibility of neutrino oscillations, extensive experimental and theoretical work has been devoted to this issue. Hints of neutrino oscillations have been claimed several times in the past. However, evidence from accelerator and reactor

experiments has meanwhile disappeared, leaving the observed solar neutrino deficit as the only possible strong indication.

A further search for neutrino oscillation has been proposed and pioneered by the Kamiokande experiment, using the flux of atmospheric neutrinos, i.e. those neutrinos produced in the atmosphere by the interaction of primary cosmic rays with air nuclei, via the subsequent decay of π's, K's and μ's.

The Kamiokande II and IMB collaborations observed an anomaly in the contained, charged-current neutrino event samples, in their water Cherenkov detectors [7, 8]. The ratio of muons to electron, measured by both experiments, is smaller than that predicted by several theoretical calculations. The simplest and often made hypothesis is that the contained events anomaly is explained through ($\nu_\mu \leftrightarrow \nu_\tau$) oscillations. In contrast, other experiments such as NUSEX and Fréjus, adopting a different experimental technique, do not see this effect [11].

To definitively clarify this crucial issue, a new-generation experiment is required. The ICARUS technique can provide a high electron to muon discrimination, a precise energy measurement, a good neutrino direction reconstruction, and a partial neutrino to antineutrino separation (by means of the different capture to decay ratio for μ^+ and μ^- in argon). In particular, the unambiguous separation between upward-going neutrinos and downward-going neutrinos will allow the effective exploitation of the long baseline range (up to 12 000 km) provided by the Earth to study ($\nu_e \leftrightarrow \nu_\mu$), ($\nu_e \leftrightarrow \nu_\tau$) and ($\nu_\mu \leftrightarrow \nu_\tau$) oscillations. In the first two cases, matter effect in enhancing the transition probability can be relevant. In fact, if the solar neutrinos undergo oscillations, enhanced by the presence of electron-rich matter along the neutrino path between the core of the sun and a detector on the Earth [12], we expect to observe the same effect for atmospheric neutrinos crossing the Earth, from the matter resonance condition expressed, in the two neutrino families scheme, as:

$$\frac{E(MeV)}{\Delta m^2(eV^2)} = \frac{\cos(2\theta)}{2\sqrt{2}G_F N_e}$$

For a fixed difference of the neutrino squared mass eigenvalues [Δm^2] and a fixed vacuum mixing parameter [$\cos(2\theta)$], the resonance energy varies as the inverse of the electron density [N_e]. If a resonance occurs in the sun, for neutrino energies ranging from about 1 to 15 MeV, since the density of the Earth is about 10 to 100 times smaller than that of the sun, we can expect to reproduce the effect in the Earth, for energies of the order of 20 to 2000 MeV. This range is especially well covered by the atmospheric-neutrino energy spectrum.

ICARUS can detect neutrino interactions down to the energy threshold for charged-current reactions on argon nuclei (about 25 MeV for electron neutrino reactions). This allows the collection of the full atmospheric neutrino statistics of about 1 200 event per year per 5 kton module in 4π steradians (assuming no oscillations).

As we shall show in the following, the analysis of the upward-going neutrino data sample (about 45% of the total statistics) provides the opportunity to extend the sensitivity to oscillations to the very low Δm^2

values of few times 10^{-5} eV^2. This possibility represents a unique occasion to study, independently and under different conditions, the intriguing phenomenon possibly at work at the heart of the sun, adding precious redundancy in the experimental data on the subject.

2.2.2 Long-baseline neutrino oscillations

One interesting complementary way to study neutrino oscillations is to extend the baseline outside the limits of the laboratory [26]. A feasibility study [13] has shown that it is possible to send a CERN ν_μ beam to Gran Sasso, which happens to lie in a favourable azimuthal direction, at a distance of 732 km, taking advantage of a planned LHC beam transfer gallery (Fig. 3).

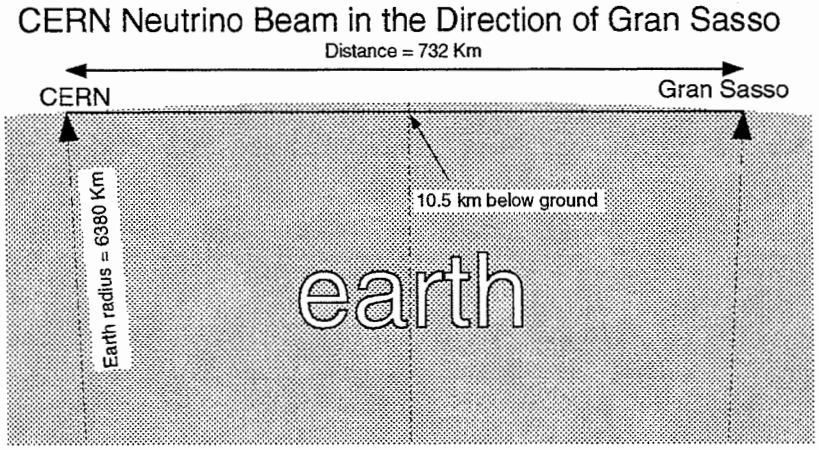

Figure 3 : Cross-sectional view of the Earth showing the path of the CERN neutrino beam traveling through 732 km of matter before reaching the Gran Sasso Laboratory

The planned neutrino beam represents a new type of international scientific cooperation between two distant laboratories when a high-energy particle beam produced at CERN is used for physics in a detector installed in another laboratory. Before reaching Gran Sasso, the neutrinos from CERN will have travelled under France, Switzerland and Italy (Figure 4).

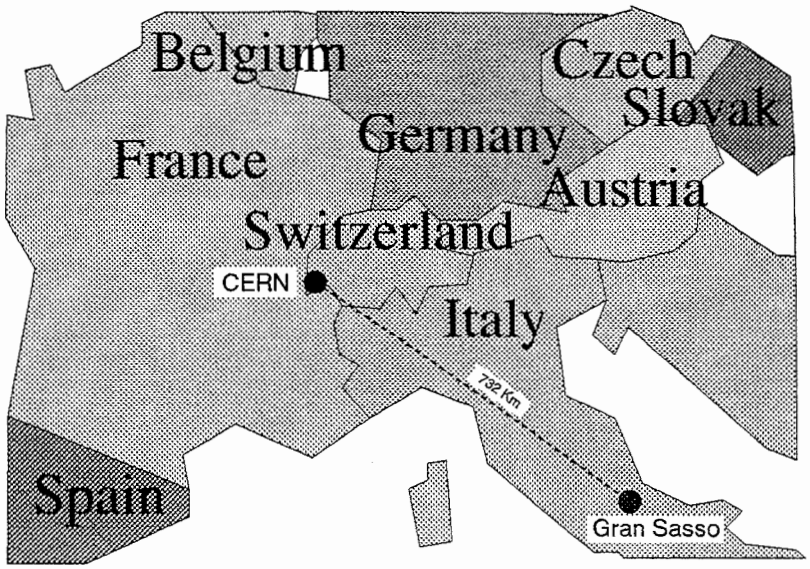

Figure 4 : Geographic configuration of the planned neutrino beam from CERN to Gran Sasso

Neutrino beams offer several clear advantages: (a) The energy spectrum is known, peaked, and can be tuned to the desired range; (b) One can switch between neutrinos and antineutrinos (interesting for matter effects); (c) The known direction and timing allow efficient background rejection; (4) The initial beam composition is known (almost entirely ν_μ or $\bar{\nu}_\mu$); (d) High rates will provide high statistical accuracy; (e) Most important for ICARUS, the accelerator neutrino beam can be used to calibrate the neutrino background to proton decay by providing neutrinos of the appropriate energy.

If the CERN neutrino beam does become available it will add a unique window of physics to the ICARUS programme, allowing us to investigate in addition to vacuum neutrino oscillations the possibility of matter effects of the Earth between CERN and Gran Sasso [14].

The sensitivity of ICARUS will largely cover, for $\nu_\mu \leftrightarrow \nu_e$ oscillations, the interesting region corresponding to the present area determined by atmospheric neutrino observations. In addition, the beam energy will be above threshold for production of τ's, and, therefore, oscillations $\nu_\mu \leftrightarrow \nu_\tau$ can be directly studied. In all cases the experiment can easily be repeated, switching the beam to antineutrinos, a specially attractive possibility if matter effects were detected.

With the CERN neutrino beam ICARUS will extend the baseline by more than two orders of magnitude, break new ground in the study of artificially produced neutrinos travelling through matter, and, in addition, use the beam to calibrate the background to proton decay.

2.2.3 Solar neutrinos

A recent status of solar neutrino experiments can be found in the review by J.N. Bahcall [15]. Let us simply recall here the latest results for each of the four experiments currently taking data.

a) Kamiokande using water Cherenkov techniques:

- Kamiokande II: Data/SSM = 0.46 ± 0.05 (stat.) ± 0.06 (syst.) [16]
- Kamiokande III: Data/SSM = 0.55 ± 0.07 (stat.) ± 0.06 (syst.) [17] where SSM stands for Standard Solar Model, usually according to J. Bahcall's model [18].

b) Homestake, SAGE, and GALLEX using radiochemical techniques:

- Homestake: 2.2 ± 0.2 SNU [19] vs 8.0 ± 3.0 (Bahcall) [18] and 6.4 ± 1.4 SNU (Turck-Chièze) [20]
- GALLEX: $83^{+18}_{-17} \pm 8$ SNU [21] vs 132^{+7}_{-6} SNU (Bahcall) [18] and 124 ± 5 SNU (Turck-Chièze) [20]
- SAGE (combined): 58^{+17}_{-24} SNU [22]; 1991 alone: 85^{+22}_{-32} SNU [22].

Combining all of these results, one probably gets a significant deficit of neutrinos coming from the sun, as compared with current solar models. However, the precise significance of the effect is hard to determine since it depends on the error attributed to the theory, which is the object of some controversy [23]. The most popular explanation for the apparent deficit of solar neutrinos, is the Mikheyev–Smirnov–Wolfenstein (MSW) mechanism [12], implying (if the data are to be interpreted as a mixing of solar ν_e's with

ν_μ's) $\Delta m_{\mu e}^2 \equiv m_{\nu 2}^2 - m_{\nu 1}^2 \sim 10^{-5}$ eV^2 and two values of the vacuum mixing parameter: $\sin^2(2\theta_{e\mu}) = 7 \times 10^{-3}$ and 0.6. Figure 5 shows the present experimental status of $\nu_e \leftrightarrow \nu_\mu$ oscillations, in the plane $\Delta m_{\mu e}^2$ versus mixing parameter. However, the available data are insufficient to distinguish even between the MSW effect and, for instance, simple vacuum oscillations [24] which imply $\Delta m_{\mu e}^2 \sim 10^{-10}$ eV^2. It is unlikely that the present experiments will resolve the puzzle, since none of them individually can distinguish effects coming from the nature of neutrinos from effects due to the neutrino production mechanism inside the sun. A new generation of experiments is therefore needed to provide: (a) real-time data with high statistics, good energy and direction resolution; (b) solar-model-independent measurements.

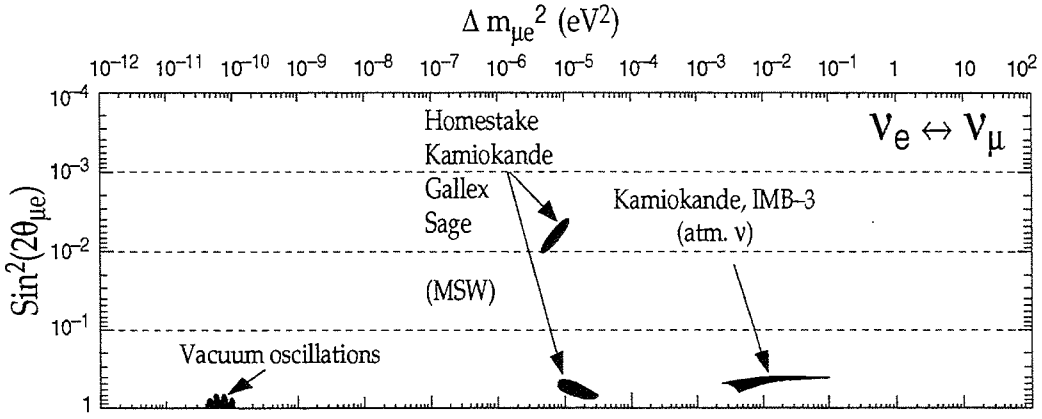

Figure 5 : MSW and vacuum oscillation solutions to the solar neutrino measured rate in the $\Delta m_{\mu e}^2$ versus mixing parameter plan. The atmospheric neutrino area determined by Kamiokande and IMB-3 is also indicated.

In addition to the indirect study using atmospheric neutrinos, ICARUS intends to directly observe solar neutrinos produced by the ^{8}B part of the sun's thermonuclear cycle, using on the one hand the reaction: $\nu_x + e^- \rightarrow \nu_x + e^-$ ($x = e, \mu, \tau$) for which the SSM predicts 3200 events per year and per module. On the other hand, the independence from the SSM is obtained by simultaneously observing the absorption reaction: $\nu_e + {}^{40}Ar \rightarrow {}^{40}K^* + e^-$, dominated by the super-allowed transition [25] to the isotopic analogue state at 4.38 MeV above the ground state of ^{40}K, followed by $^{40}K^* \rightarrow {}^{40}K + 1$ or 2 γ [2 MeV], for which the SSM predicts 2 800 events per year and per module (taking into account 70% detection efficiency in ICARUS for $E_{th}^e = 5$ MeV). The electron energy threshold depends on the details of the wire-chamber design and on the radioactive background. Presumably, experience with the large statistics of real data which will be accumulated should help in studying the background in order to reach the lowest possible threshold.

It should also be noted in this context that the outer argon layers play the role of a neutron shield for the inner part of the argon volume. The central part of the detector may prove to be free of the most dangerous background: neutrons from the natural radioactivity of the rocks and of the detector steel structure. It is therefore hoped that, at least in a limited fiducial volume, it will be possible to observe solar neutrinos with an electron energy threshold as low as 5 MeV.

The distinctive properties of the recoil electron energy spectrum together with the detection of photon energy associated with the $^{40}K^*$ decay allow one to distinguish the two reactions (electron scattering and absorption) and measure the ratio R of their cross-sections. Since the first reaction is sensitive to all neutrino species and the second one to only the electron neutrino, the ratio R provides a direct measurement of the fraction of ν_e's which converted to ν_μ's or ν_τ's through oscillations (Figure 6), independently of the absolute value of the solar neutrino flux.

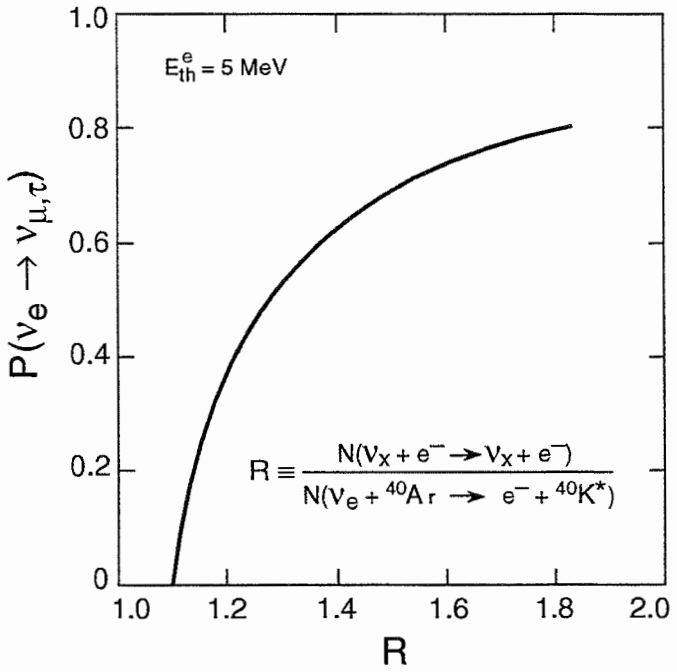

Figure 6 : Probability $P(\nu_e \rightarrow \nu_{\mu,\tau})$ of ν_e oscillations versus the ratio *R*

2.2.4 Astrophysical and cosmological phenomena

There are several classes of astrophysical and cosmological phenomena that can be studied with a neutrino telescope such as ICARUS.

i) In addition to the study of intrinsic neutrino properties, solar neutrinos constitute a window for the understanding of the neutrino production mechanism inside stars. The electron recoil energy distribution for elastic scattering and absorption events, and their fluxes, may provide direct and detailed information on ^8B solar neutrinos.

ii) The search for neutrino bursts from supernova collapses (mainly in our Galaxy) could provide important new constraints on present models. The search for new sources of low-energy neutrinos or antineutrinos is based on the reaction ν_X e $\rightarrow$ ν_X e, where ν_X stands for any type of neutrino or antineutrino. A practical threshold is near E_e = 5 MeV, which is to be compared with the energy of supernova neutrinos above 10 MeV. There exists in fact a unique energy window above the solar ^8B and hep neutrinos and below atmospheric neutrinos where one could detect neutrinos coming from all the supernovae which have occurred in the history of the universe. These neutrinos are expected to be redshifted but not thermalized.

More generally, it is expected that the observation of cosmic neutrinos will complement the observation in other channels (γ rays, etc.). The fact that ICARUS is continuously sensitive makes it ideally suited for the detection of any unexpected sporadic neutrino source, the most common of them being supernova explosions.

As we will discuss, ICARUS is sensitive to at least three classes of neutrino sources, the sun, cosmic-ray interactions with the Earth's atmosphere, and supernovae. Hence the physics potential of ICARUS is very broad in the neutrino sector, in addition to proton decay.

2.3 Conclusion

The ICARUS Collaboration intends to concentrate mainly on the search for proton decay and on some of the most important aspects of neutrino physics (atmospheric neutrinos, solar neutrinos, long-baseline neutrino oscillations, and astrophysical and cosmological neutrinos). Our experimental strategy consists in giving the priority to the high-energy phenomena: the search for proton decay, the study of atmospheric neutrinos, and the long-baseline neutrino oscillations. Very significant advance in all these sectors will be achieved.

ICARUS should open a new window in our understanding of the universe both on the infinitely small scale and on the cosmological scale.

2.4 References

[1] CERN-Harvard-Milano-Padova-Roma-Tokyo-Wisconsin Collaboration, INFN/AE-85/7, Frascati (1985).

[2] ICARUS Collaboration, ICARUS I: An optimized, real time detector of solar neutrinos, INFN- LNF- 89/005 (R), 1989.

[3] C. Rubbia, CERN-EP Internal Report 77-8 (1977).

[4] P. Benetti et al., Nucl. Instrum. Meth. **A332** (1993) 395.

[5] U. Amaldi, W. de Boer and H. Fürstenau, Phys. Lett. **B 260** (1991) 447.

[6] J. Pati, A. Salam and U. Sarkar, Phys. Lett. **B133** (1983) 330; J. Pati, Phys. Rev. **D29** (1984) 1549.

[7] K.S. Hirata et al., Kamiokande Collaboration, Phys. Lett. **B280** (1992) 146–52.

[8] D. Casper et al., IMB Collaboration, Phys. Rev. Lett. **66** (1991) 2561.

[9] W.A. Mann, T. Kafka and W. Leeson, Phys. Lett. **B291** (1992) 200.

[10] B Pontecorvo, Zh. Eksp. Teor. Fiz. 7 (1958) 172 [Sov. Phys. JETP **34** (1958) 247].

[11] Ch. Berger et al., Fréjus Collaboration, Phys. Lett. **B245** (1990) 305; M. Aglietta et al., NUSEX Collaboration, Europhys. Lett. 8 (1989) 611.

[12] L. Wolfenstein, Phys. Rev. **D17** (1978) 2369; **D20** (1979) 2634; S.P. Mikheyev and A.Yu. Smirnov, Yad. Fiz. **42** (1985) 1441; Nuovo Cim. **9C** (1986) 17; H. Bethe, Phys. Rev. Lett. **56** (1986) 1305.

[13] A. Ball, B. Bianchi, J.P. Revol, G.R. Stevenson and E. Weisse, CERN Beams for Long Baseline Neutrino Oscillations Experiments, CERN-SL/Note 92–75 (BT).

[14] G. Fiorentini and B. Ricci, Old and New Interactions in Long Baseline Neutrino Experiments, INFN Ferrara 06-93, Proc. of Workshop on Neutrino Telescopes, Venice, March 1993, ed. M. Baldo-Ceolin.
[15] J.N. Bahcall, Solar Models and Experiments, Proc. Les Rencontres de Physique de la Vallée d'Aoste, La Thuile, March 1993.
[16] K.S. Hirata et al., Phys. Rev. Lett. **65** (1990) 1297.
[17] Y. Suzuki, Kamiokande Results, Proc. Int. Symp. on Neutrino Astrophysics, Takayama, Japan, 1992.
[18] J.N. Bahcall and M.H. Pinsonneault, Rev. Mod. Phys. **64** (1992) 885.
[19] R. Davis Jr., BNL-508-79, The Status and Future of Solar Neutrino Research, 1 (1978), ed. G. Friedlander; R. Davis Jr., Workshop on Neutrino Telescopes, ed. M. Baldo-Ceolin, Palazzo Loredan, Venice, Feb. 1990, pp. 1–13.
[20] S. Turck-Chièze et al., Astrophys. J. **335** (1988) 415; S. Turck-Chièze, Proc. Int. Conf. Inside the Sun, Versailles, 1989, eds. G. Berthomieu and M. Cribier (Kluwer Acad. Publ., Dordrecht, 1989), p. 125; S. Turck-Chièze and I. Lopez, Inside the Stars, Vienna, 1992, Saclay Report, SAp 1992/64, to appear in Astrophys. J. (1993).
[21] P. Anselbaum et al., Phys. Lett. **B285** (1992) 376 and 390; M. Spiro, Proc. Int. Europhys. Conf. on High Energy Physics, Marseille, 1993.
[22] V.N. Gavrin, Int. Conf. on High Energy Physics, Singapore, 1990, Vol. 1, p. 693; Phys. Rev. Lett. **67** (1991) 3332; Int. Conf. on High Energy Physics, Dallas, Texas, USA (1992); T. Bowles, Moriond Conf., Villars, Switzerland, Jan.-Feb. 1993.
[23] D.R.O. Morrison, Is there a Solar Neutrino Problem? Review of Theory and Experiments, Moriond Conf., Villars, Switzerland, Jan.-Feb. 1993.
[24] V. Barger, R.J.N. Phillips and K. Whisnant, Long Wavelength Oscillations and the GALLEX Solar Neutrino Signal, MAD/PH/708, IS-J 4700, Jul. 1991.
[25] J.N. Bahcall, M. Baldo-Ceolin, D. Cline, and C. Rubbia, Phys. Lett. **B178** (1986) 324; R.S. Raghavan, Bell Labs, T.M. 79–1131–31 (79) unpublished.
[26] A. Capone et al., 'A Possible Accelerator Experiment to Solve the Solar-Neutrino Puzzle', Il Nuovo Cimento, Vol. 98A (1987) 211.

III. GENERAL DETECTOR CONCEPT

Even though the detailed description of the detector belongs to Volume II of this proposal, it is useful to give here the main features of the proposed detector in order to better comprehend the potential of the ICARUS physics programme. We are still in the process of defining the final configuration of the detector; we describe here one of the possible designs.

1. The mechanics

ICARUS consists of up to three cryostat modules of cylindrical shape, making optimal use of the experimental Hall C in the Gran Sasso Underground Laboratory (Figure 1a and 1b). The mechanical design that will be chosen will be an optimization given the three basic requirements:

- Detector performance and reliability
- Safety
- Mechanical feasibility and related cost.

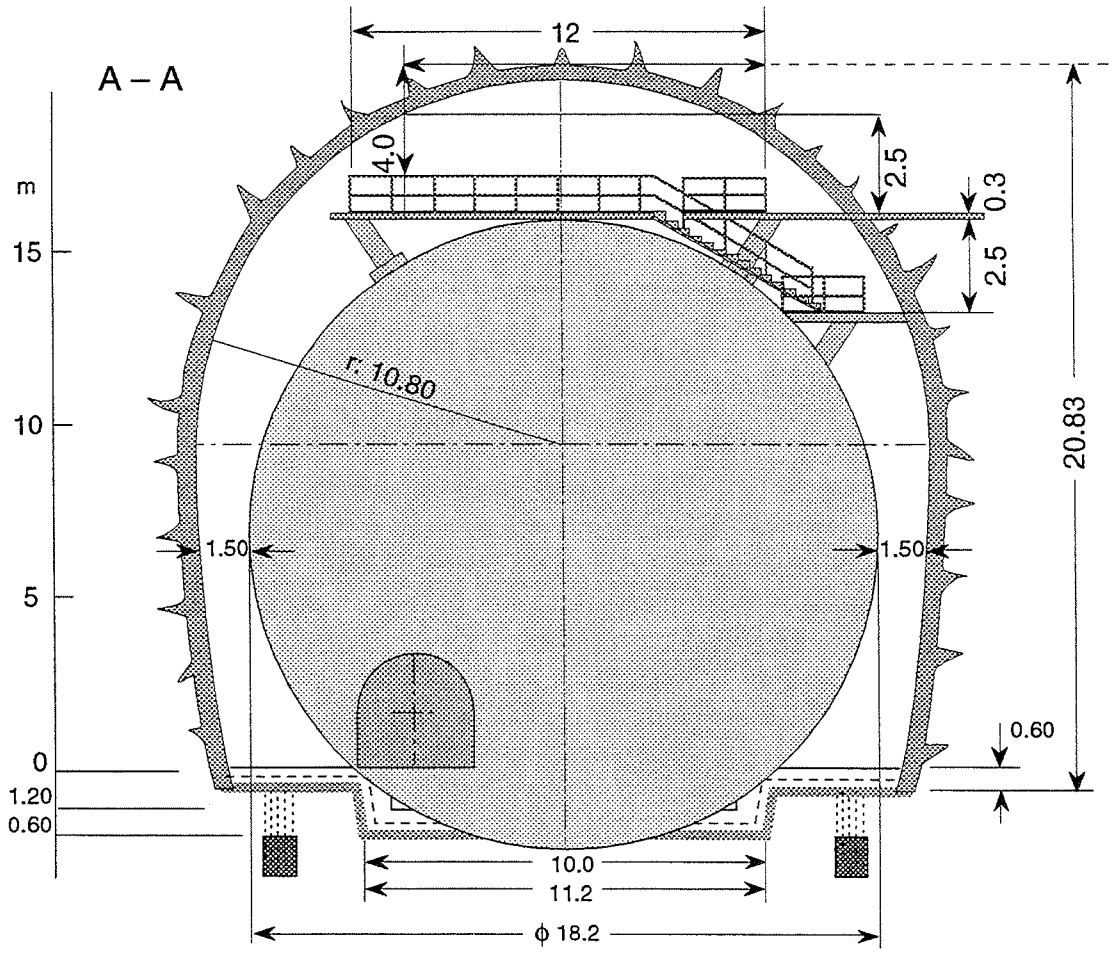

Figure 1a : Conceptual view of Hall C at Gran Sasso with the ICARUS detector

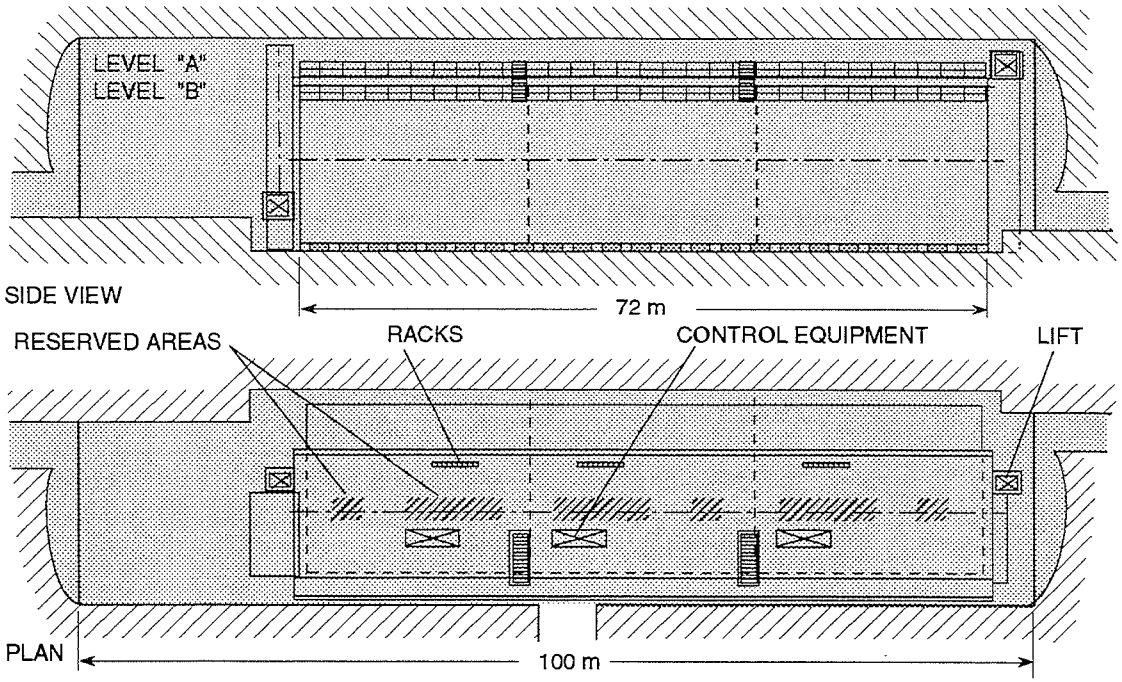

Figure 1b : Longitudinal view of Hall C at Gran Sasso showing conceptually the installation of the three ICARUS cryostat modules

The present concept, driven by the above design criteria, was chosen in order to fit the largest possible volume of liquid argon in the available cavern, and to minimise the risk of liquid argon spill and liquid argon contamination. It is a modular construction of identical and independent cryogenic vessels. The fiducial mass of each module will be 4 700 tons of liquid argon. The main features (Table 1) are the following:

– an inner vessel containing about 4 180 m^3 of sensitive liquid argon protected by an evacuated double wall;

– an outer vessel (about 18 m diameter and 25 m long) to provide thermal insulation (evacuated super-insulation), and a further protection against argon spill. The outer vessel is made of FeNi (9%) alloy, a standard construction material for liquid CH_4 containers. If this alloy fulfills the stringent surface cleanliness requirements of ICARUS, it will also be used for the inner vessel, which otherwise will be made of 304L stainless steel;

– all openings for instrumentation, feedthroughs, main holes, etc. are located on the top of the cryostat;

– the ionization information is read by several double-sided wire chambers separated by high-voltage cathode planes. High-voltage race-tracks running parallel to the module axis provide the desired uniform electric field configuration.

Figure 2 is an artist's view of the detector, showing the principle of the wire plane arrangements, and the relative size of one module. However, the detailed wire chamber configuration is under study and will be described in Volume II of this proposal.

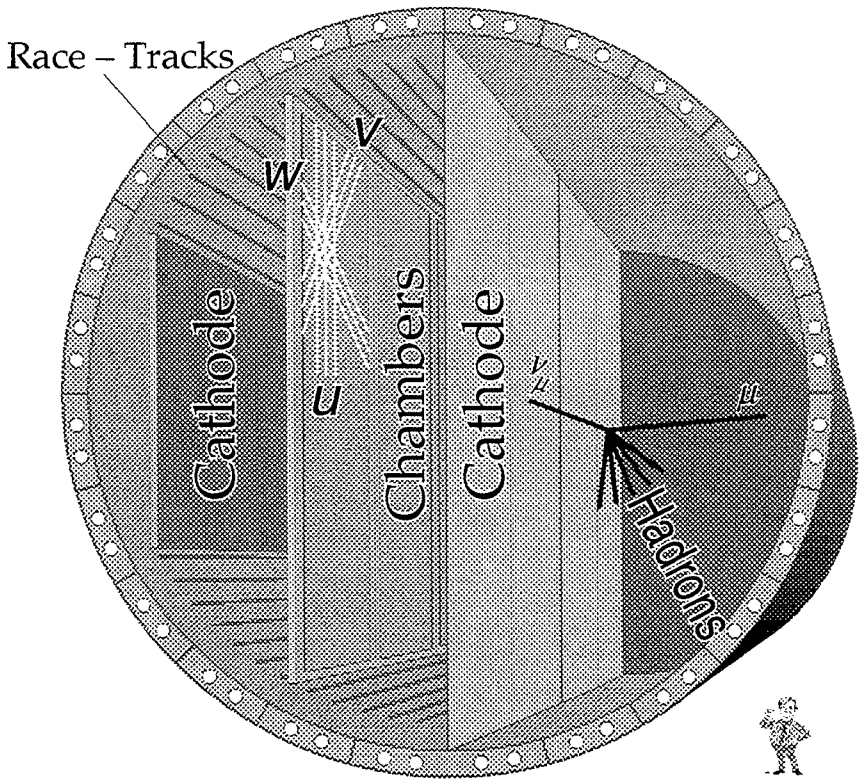

Figure 2 : An artist's view of one ICARUS module for Gran Sasso

Table 1 : The ICARUS cryostat parameters

	Internal vessel	External vessel
Shape	Horizontal cylinder with domed ends	Horizontal cylinder with flat ends
Diameter	16.0 m net	18.2 m external
Length	20.0 m net	24.8 m external
Volume	4 180 m^3 net, total	–
Filling ratio	0.90 to 0.95	–
Design pressure	0.2 + hydro.	0.1 MPa external
Design temperature	85°K	20°C
Material	AISI 304L	9% Ni steel
Hull structure	Double, compartment	Single, reinforced rings
Ends' structure	Double, compartment	Sandwich, partially open
Body weight	~ 750 t total	~ 500 t total

2. The electronics and readout

The 50 000-channel ICARUS imaging readout is similar to the one developed for the 3-ton prototype (Figure 3), but with a wider dynamic range because of the broad spectrum of phenomena to be observed, and with the addition of a hit-finder processor (ASIC), allowing real-time pulse identification. This system provides continuous readout of the whole detector without dead time, and is based on commercially available standard components used in television applications (SAMUX, FADC, VDRAM).

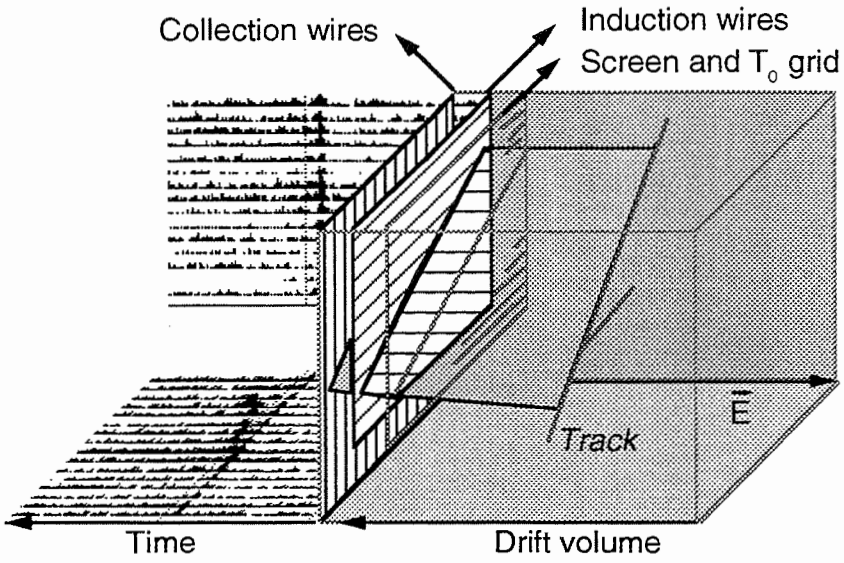

Figure 3 : Principle of the wire readout in the 3-ton ICARUS prototype

The detector wire signals (Figure 4) are amplified, shaped, and multiplexed in groups of eight. The composite signal is transmitted to the digital electronics consisting of a receiver and of a 20 MHz Flash ADC, equivalent to a sampling period of 400 ns per channel. In order to compress the data, the digital output may be filtered by a custom-built processor. It is then saved into a dual-port video memory with a total capacity of 128 kbyte (equivalent to 16 kbyte per channel) providing a maximum recording time of 6.4 ms at 2.5 MHz.

The hit-finder processor (ASIC) has performance and functionality similar to those of the digital signal-processing elements in development at CERN for application to the next generation of experiments at LHC. The readout of the whole system is based on industry-standard crates and commercial processing modules. The data acquisition will be controlled by desktop workstations interfaced to VME and to high-density popular video recorders.

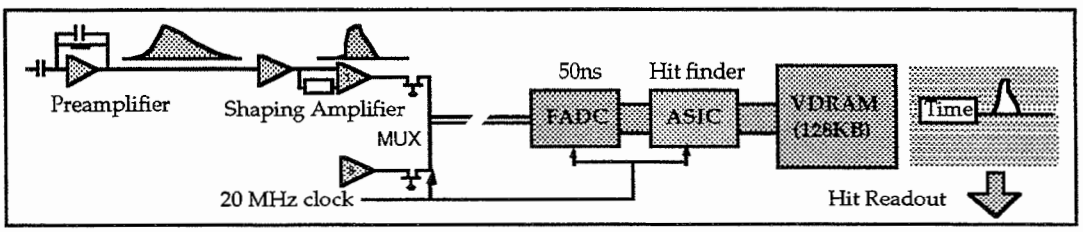

Figure 4 : Block diagram of the front-end readout electronics for ICARUS

In summary the readout for ICARUS is a straightforward extrapolation of the technique studied in the proposal for ICARUS I and tested with the 3-ton prototype, however, some options are considered in view of possible future evolutions in the technology and the results of the present LHC programme for detector R&D.

IV. THE ICARUS PHYSICS PROGRAMME

1. The search for proton decay

One of the most intriguing problems in the physics of the last few years concerns the stability of ordinary matter. From gauge theories we know that absolute charge conservation is directly linked to gauge invariance and to the existence of long-range interactions. This is the case of electric charge conservation. Searches have been conducted for a long time in Eötvös-type experiments for evidence of a long-range field coupled to the baryon number [1]. At present there is no indication that such a field exists up to a level of 10^{-9} times the gravitational force and so, although baryon number conservation has been tested to a much higher level with respect to the electric charge, there is in principle no reason to believe that such a conservation is exact and is not instead a low-energy phenomenological behaviour of baryon-violating interactions. On the other hand, to explain the observed predominance of matter over antimatter and the current ratio between photons and baryons in the universe, cosmological theories must assume that, in the very hot initial stages of the Big Bang, there were frequent baryon non-conserving interactions coupled at some level to CP violating processes [2]. Moreover, baryon non-conservation is a natural consequence of all the Grand Unification Theories (GUTs). The scale of the process is determined by the mass of the Grand Unification bosons which are in turn expected to be, from the extrapolation of the running coupling constants, around 10^{16} GeV. Such a colossal energy is far above that of any known elementary process occurring at present, but must have been reached in the very early stages of the life of our universe (very broadly, from 10^{-40} to 10^{-35} seconds from the Big Bang), so GUTs can provide a natural explanation of the problem of the matter–antimatter asymmetry.

One of the consequences of any GUT, most important from the experimental point of view, is that the proton is not stable. In most GUTs, the effective interactions responsible for proton decay conserve (B–L), leading to the selection rule $\Delta B = \Delta L$. Possible proton decay modes are therefore of the form: $p \rightarrow \ell^+ + X$, where X denotes any hadronic particle(s), while the modes $p \rightarrow \ell^- + X$ are forbidden. [Note that neutron decays are related to the proton decay modes by isospin symmetry; $\Gamma(p \rightarrow e^+\pi^0) = 1/2\ \Gamma(n \rightarrow e^+\pi^-)$, for example.] The typical proton lifetime, based on the 4-fermion interaction, mediated by gauge bosons and not taking into account any Higgs-mediated interactions, is of the form [3]:

$$\tau \sim \frac{M_X^4}{\alpha_G^2 m_p^5} = \frac{10^{34}\,year}{\alpha_G^2}\left(\frac{M_X}{2.5\times10^{16}}\right)^4 \qquad (1)$$

where α_G is the square of some typical coupling constant at the unification scale. A desert-scenario SU(5) GUT predicts a value of M_X at $O(10^{14})$ GeV, which via $p \rightarrow e^+\pi^0$ yields a lifetime for the proton of $\tau_p = 10^{31\pm1}$ year, a value somewhat below the current experimental limit $\tau_p > 10^{32}$ year [4]; this was the basis for excluding such models some years ago. It is important to keep in mind, however, that unification within the Standard Model (SM) is still

possible and plausible [5] if the GUT gauge group becomes more complicated and has an intermediate step of symmetry breaking, for example, an SO(10) breaking into SU(3) × SU(2) × SU(2) × U(1) at $M_X \sim 10^{16}$ GeV. The predicted M_X of an intermediate threshold SM GUT can then be large enough to push the proton lifetime beyond the experimental limits; the lifetime in this case is rather model-dependent.

However, recent LEP precision measurements of $\sin^2\theta_W$ and $\alpha_S(M_Z)$ have generated renewed interest in GUTs. Extrapolation of the gauge coupling constants to higher energy shows [6] that they meet at a point when evolved within the context of a minimal supersymmetric theory (MSSM) which has a unification scale M_X at $O(10^{16}$ GeV), while the couplings fail to unify within the SM, which rules out the simplest one-step GUT models, like a desert-scenario SU(5), SO(10), etc. Alternatively, one may accurately predict the value of $\sin^2\theta_W$ from the assumption of unification and the LEP measurement of $\alpha_S(M_Z)$. In this way, within the context of the MSSM one predicts $\sin^2\theta_W = 0.2315 \pm 0.0026$, in striking agreement with the experimental value of $\sin^2\theta_W = 0.2325 \pm 0.0007$. The same procedure in the context of the Standard Model gives a value of $\sin^2\theta_W$ that is too small.

The proton lifetime prediction within the context of the MSSM GUT is, on the other hand, $\tau_p = 10^{38\pm1}$ year [7], based on the 4-fermion operator formula above, due to the higher value of $M_X \sim O(10^{16}$ GeV). In this class of models, however, there is the complication that, because of the presence of scalar particles that carry a baryon number, there exist dimension-5 baryon number-violating operators [8], which can mediate proton decay and possibly lead to too-rapid decay rates. The effective operator leading to such proton decay in general must change generation, so such channels are characterized by the presence of strange particles in the final state. This effective operator leads to the selection rule:

$$\frac{\Delta S}{\Delta B} = 0, 1 \qquad (2)$$

which tells us that $p \to \bar{\nu}\,\pi^+$ and $\bar{\nu}\,K^+$ are allowed, but that $p \to \bar{\nu}\,K^-\,\pi^+\,\pi^-$ and $n \to e^+\,K^-$ are forbidden. Other relations among the various decay modes can be obtained from the soft-pion theorems or non-relativistic SU(6) symmetry, or other model-dependent features [3]. One prediction for proton decay through the channel $p \to \bar{\nu}\,\pi^+$, for example, yields the lifetime $\tau_p = 10^{29\pm4}$ year, which is still marginally compatible with the experimental limit of $\tau_p > 10^{32}$ year [4], but in general the decay rates are largely determined by whatever means are used to suppress the dimension-5 interactions.

There exist classes of supergravity models which will obviously be tested by a combination of LEP and ICARUS, since they predict [9] that either $\tau(p \to \bar{\nu}\,K^+)$ will be smaller than 1.5×10^{33} years (which is well within ICARUS range) or that one of the gauginos ($\tilde{w}_1$) or one of the Higgs particles will be discovered at LEP200.

From the experimental point of view, all the decay modes mentioned above present a great interest and should certainly be searched for.

Another relevant point comes from the observation made by Mann, Kafka and Leeson [10] that the observed anomaly in the atmospheric ν_μ/ν_e ratio, normally ascribed to a ν_μ depletion due to neutrino oscillations, could

be explained as an excess of ν_e-like events coming from the decay $p \rightarrow e^+ \nu \nu$ with a mean lifetime $\tau/Br. \approx 4 \times 10^{31}$ years. $\Delta(B–L) = -2$ decay modes are possible in the context of a $SU(2)_L \times SU(2)_R \times SU(4)_{col}$ with a high-mass Higgs sector [11] (Figure 1). In particular, Pati has shown [12] that the Yukawa couplings of the theory can be adjusted in such a way that the decay $p \rightarrow e^+ \nu \nu$ is dominant with respect to either of the modes $p \rightarrow \ell$ + meson or $p \rightarrow \mu^+ \nu \nu$.

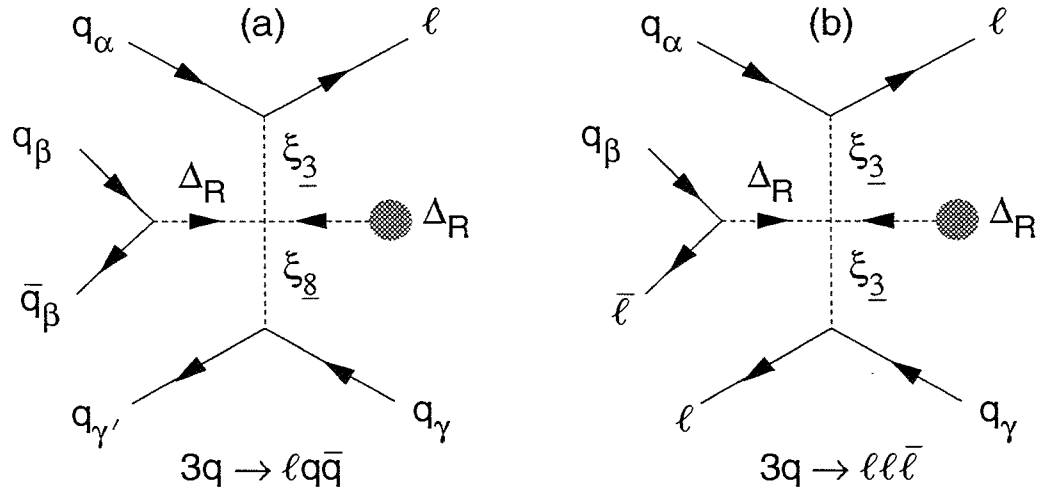

Figure 1 : Feynman diagrams for proton decay into (a) $\ell q \bar{q}$ and (b) $\ell \ell \bar{\ell}$ in the Pati–Salam model

Therefore proton decay may well be happening with a relatively short lifetime in certain specific channels. A new detector technique is obviously required to explore such channels and to go beyond the present experiment sensitivity in other channels.

Thanks to its large sensitive mass (4.7 kton) and to its spatial and energy resolution capabilities, ICARUS is an ideal device for nucleon decay detection, in particular for those channels that are not accessible to Cherenkov detectors due to the complicated event topology, or because the emitted particles are below the Cherenkov threshold ($K^\pm$). Unlike the other large detectors for proton decay, ICARUS, with its excellent tracking and particle identification capabilities providing a much more powerful background rejection, can perform exclusive decay modes measurements. In particular, it is possible to distinguish between atmospheric neutrino events and true nucleon decays. Our Monte Carlo simulation has already verified this point for a number of decay channels (Section 1.2).

We have performed a detailed event simulation based on the standard GEANT Monte Carlo code [13] and the realistic events obtained contain very long tracks with redundant information, allowing particle identification and measurement of their energies with great precision. See, for instance, the spectacular example of the SUSY-preferred decay mode of the proton $p \rightarrow \bar{\nu} K^+$ displayed in Figure 2. We can observe the increase in ionization deposition by the K^+ as it comes to rest. There is no ambiguity in the direction of the particle along its trajectory.

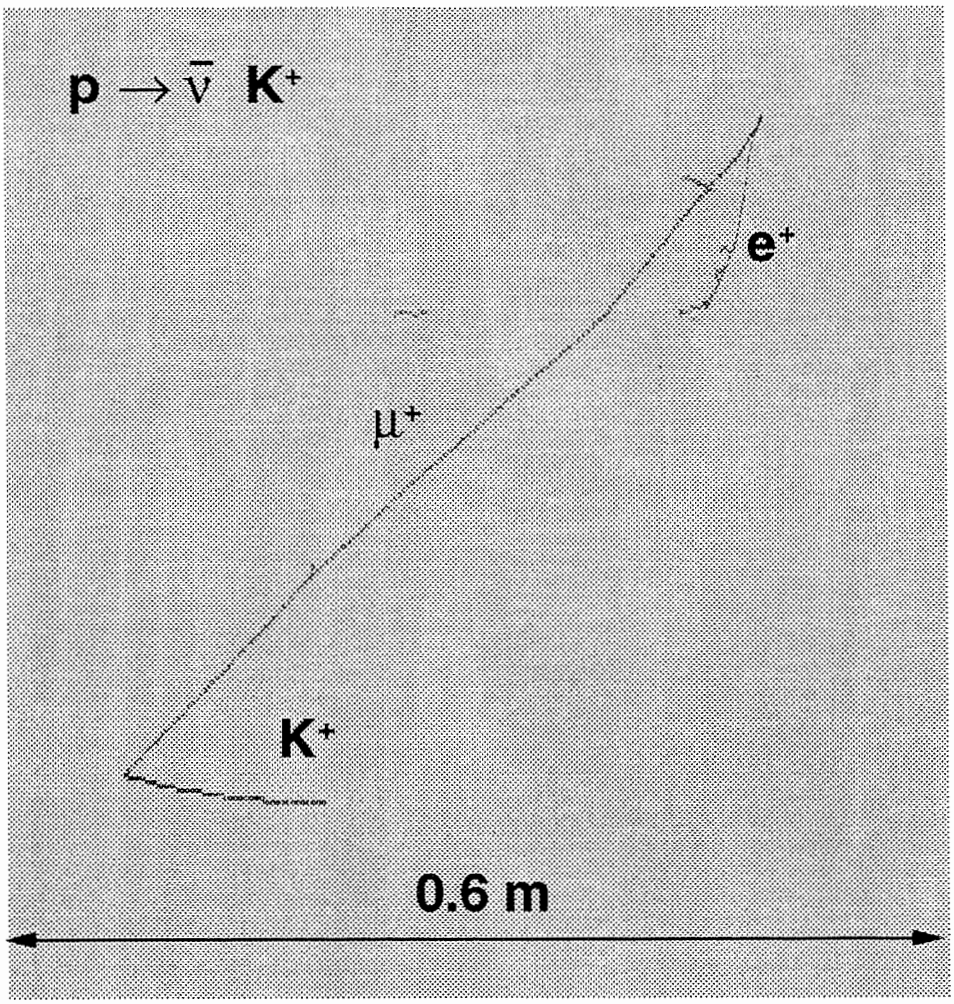

Figure 2 : Simulated proton decay in the Supersymmetrically preferred channel $p \rightarrow \bar{\nu} K^+$ as could be observed in ICARUS

Particle identification benefits greatly from the ability to measure the ionization loss (dE/dx). In particular, using dE/dx versus range only, an excellent separation is obtained between pions and kaons. Figure 3 shows the result of our Monte Carlo detector simulation of pion and kaon tracks. In Figure 3a we plot the dE/dx as a function of the distance from the stopping point of each particle for a 5 mm wire pitch (each track then contributes to this plot with a number of points proportional to the track length). The superimposed curve is the fit of a well-suited function to the kaon data only. Figure 3b shows the distribution of the distances of the points measured along each track from the above fitted functions. The separation between kaons and pions is obvious even here where we make use of the dE/dx information only. If one takes into account that, in addition, energy and topology information are also available, it is easy to understand that the proton decays can clearly be identified event per event, and, for most channels, it is not necessary to rely on statistical methods to eventually extract a signal. As a consequence, many exclusive channels will be searched for simultaneously, both for proton and neutron decays for which discoveries can occur at the one-event level. This is certainly the main strength of the ICARUS technique.

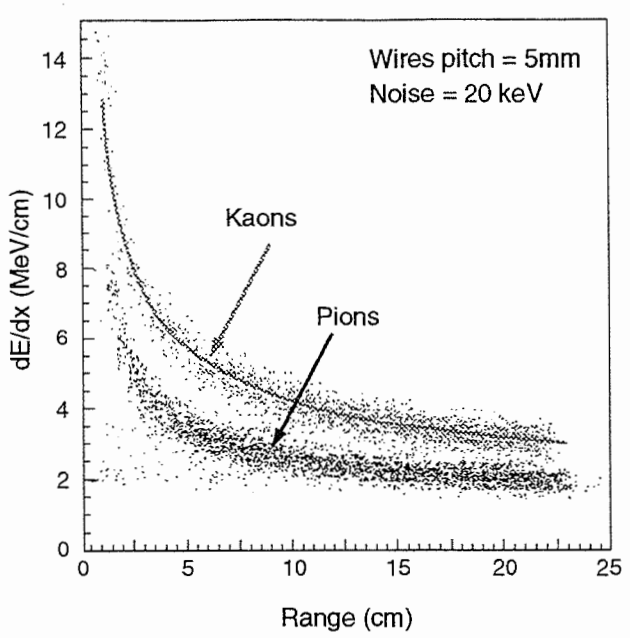

Figure 3a: Energy loss profile along kaon and pion tracks obtained in ICARUS, assuming an equivalent noise of 20 keV per wire

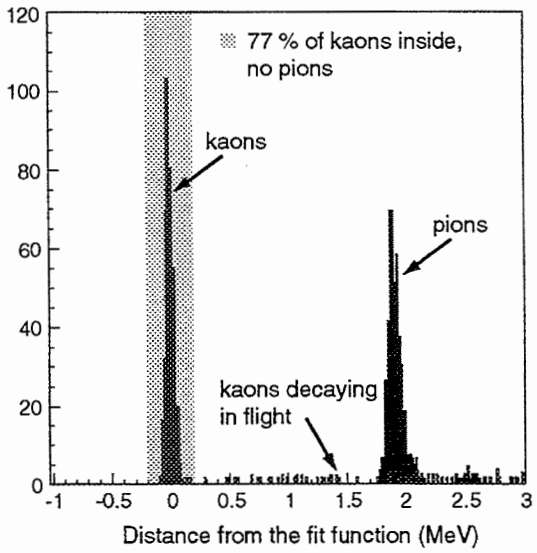

Figure 3b : Distance from the fit function (see Figure 3a) for energy loss distributions along pion and kaon tracks. For each particle the distance is normalized to the corresponding number of points.

In the absence of background, the limit on the nucleon lifetime reachable in T years of observation is given by the simple formulae:

$$\tau_p > 1.2 \times M \times T \times \eta \quad (10^{32} \text{ year}) \quad (90\ \%\ \text{C.L.}) \text{ for the proton} \qquad (3a)$$

$$\tau_n > 1.4 \times M \times T \times \eta \quad (10^{32} \text{ year}) \quad (90\ \%\ \text{C.L.}) \text{ for the neutron} \qquad (3b)$$

where M is the detector mass in kton and η is the overall detection efficiency. As we will discuss later, in order to reduce neutrino-induced backgrounds we make use of the ability of ICARUS to fully reconstruct the events. Proton decay events are characterized by a definite value of the total energy and by

the fact that the total momentum of the decay products must be zero. These features, which are true for a free nucleon, are also approximately verified for a nucleon bound in a nucleus, provided the decay products do not rescatter before escaping the nucleus. As a consequence, we also include in our definition of detection efficiency $\eta = \varepsilon_D \cdot \varepsilon$ the probability ε that the decay products do not interact with the nucleus in which they were produced, and the reconstruction efficiency ε_D.

These nuclear effects, the distortions of the energy and momentum distributions due to the nucleon Fermi motion, and the reinteraction of decay particles with the nucleus have been studied by Monte Carlo simulation methods (see Section 1.1).

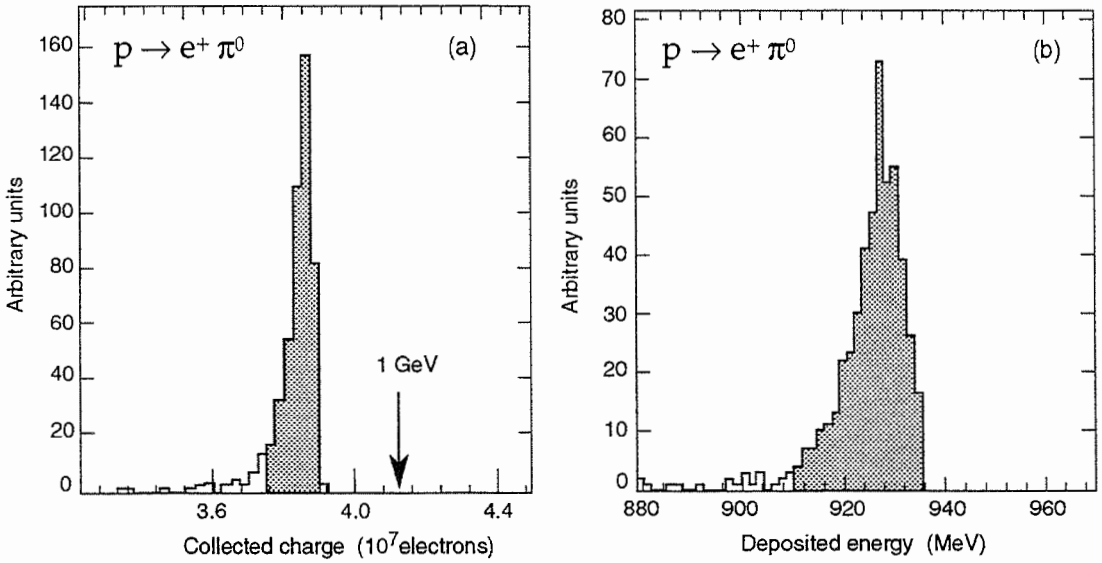

Figure 4 : Distribution of (a) the charge collected, (b) the energy collected for $p \rightarrow e^+ \pi^0$ events which have been simulated for a detector wire pitch of 5 mm. The dashed area contains 91% of the events and corresponds to a 30 MeV energy window.

A key element in the rejection of backgrounds is the excellent detector resolution expected for the distribution of the collected charge and of the energy deposition. This is illustrated by Figure 4 with simulated events for the classical decay mode $p \rightarrow e^+ \pi^0$. More than 90% of the events lie inside a window of 30 MeV.

Table 1 lists, for some of the main decay modes under consideration, the computed probabilities (ε) for the nucleon decay products to escape the argon nucleus without interacting. Inserting these values into formulae (3) and taking 4.7 kton as the sensitive mass, we obtain the limits shown in Table 2 (assuming $\varepsilon_D = 1$).

For example, for the decay mode $p \rightarrow \bar{\nu} K^+$ we obtain $\varepsilon = 0.85$ and a corresponding lifetime limit $\tau_p > 4.7 \times 10^{32}$ (90% C.L.) years for one year of data-taking. In ten years of operation, ICARUS will be able to reach a proton lifetime of 5×10^{33} years for this most interesting decay mode. This would increase the present limit by about two orders of magnitude. For this decay mode in particular (as for many others) we don't expect to have any significant background. Kaon production by atmospheric neutrinos is very

rare and always occurs in association with another strange particle. The probability that a charged-current neutrino interaction with emission of a proton from the argon nucleus can simulate a $p \rightarrow \bar{\nu} K^+$ decay is also expected to be negligible, because we can either distinguish the direction of motion of the charged hadron due to the increase of ionization at the end of the range, or directly recognize the kaon from the dE/dx and range measurements (Figure 3). However, since for this particular channel the discovery requires only one event, because of the negligible background, a lifetime of 10^{34} years is in fact reachable.

Table 1 : Efficiency (ε), as defined in the text, for various nucleon decay modes

Decay mode	ε
$p \rightarrow e^+ \pi^0$	0.42
$p \rightarrow \bar{\nu} \pi^+$	0.42
$p \rightarrow \mu^+ \pi^0$	0.38
$p \rightarrow \bar{\nu} K^+$	0.85
$p \rightarrow e^+ \pi^+ \pi^-$	0.13
$p \rightarrow e^+ \rho^0$	0.08
$n \rightarrow e^+ \pi^-$	0.4
$n \rightarrow \mu^+ \pi^-$	0.37
$n \rightarrow \nu \pi^0$	0.42
$n \rightarrow e^- K^+$	0.85
$n \rightarrow e^+ \rho^-$	0.08
$n \rightarrow e^+ \pi^- \pi^0$	0.13

Table 2 : Number of background events and 90% C.L. limits on the lifetime corresponding to one year of data with one ICARUS module

Decay mode	Number of background events	Lifetime limit (90% C.L.)
$p \rightarrow e^+ \nu \nu$	$5.7 \pm 0.8 \pm 1.7$	1.2×10^{32}
$p \rightarrow e^+ \pi^0$	< 1.1	2.3×10^{32}
$p \rightarrow \bar{\nu} K^+$	< 0.23	4.7×10^{32}

Figure 5 illustrates well the unambiguous signature of electrons, pions, kaons, photons, etc. in ICARUS for some characteristic nucleon decay modes.

For the particular case of $p \rightarrow e^+ \nu \nu$, as there are only leptons in the final state, nuclear reinteraction is negligible and $\varepsilon \sim 1$. Events from this channel are characterized by an isolated electron shower with a three-body decay energy spectrum mainly in the range 0 to 500 MeV. Figure 6 shows the simulation of one of these events. In this case the main source of background is atmospheric ν_e charged-current interactions which cannot be neglected. From our simulation of atmospheric neutrino events we obtained a background rate for this channel of $5.7 \pm 0.8 \pm 1.7$ events per module and per

year, where the first error is statistical and the second one reflects the present 30% uncertainty in the atmospheric neutrino flux. From the direct study of atmospheric neutrinos, ICARUS will eventually reduce that uncertainty in a significant way. The background rate obtained here is consistent with a naive prediction which can be derived by scaling the Fréjus experiment background [14]. The overall detection efficiency for $p \to e^+ \nu \nu$ is 0.77. Consequently, with one year of data, ICARUS will reach a lifetime limit for this channel of 1.2×10^{32} years to be compared with 4×10^{31} years which would be the value if we assume that the atmospheric ν_e/ν_μ anomaly be due to $p \to e^+ \nu \nu$.

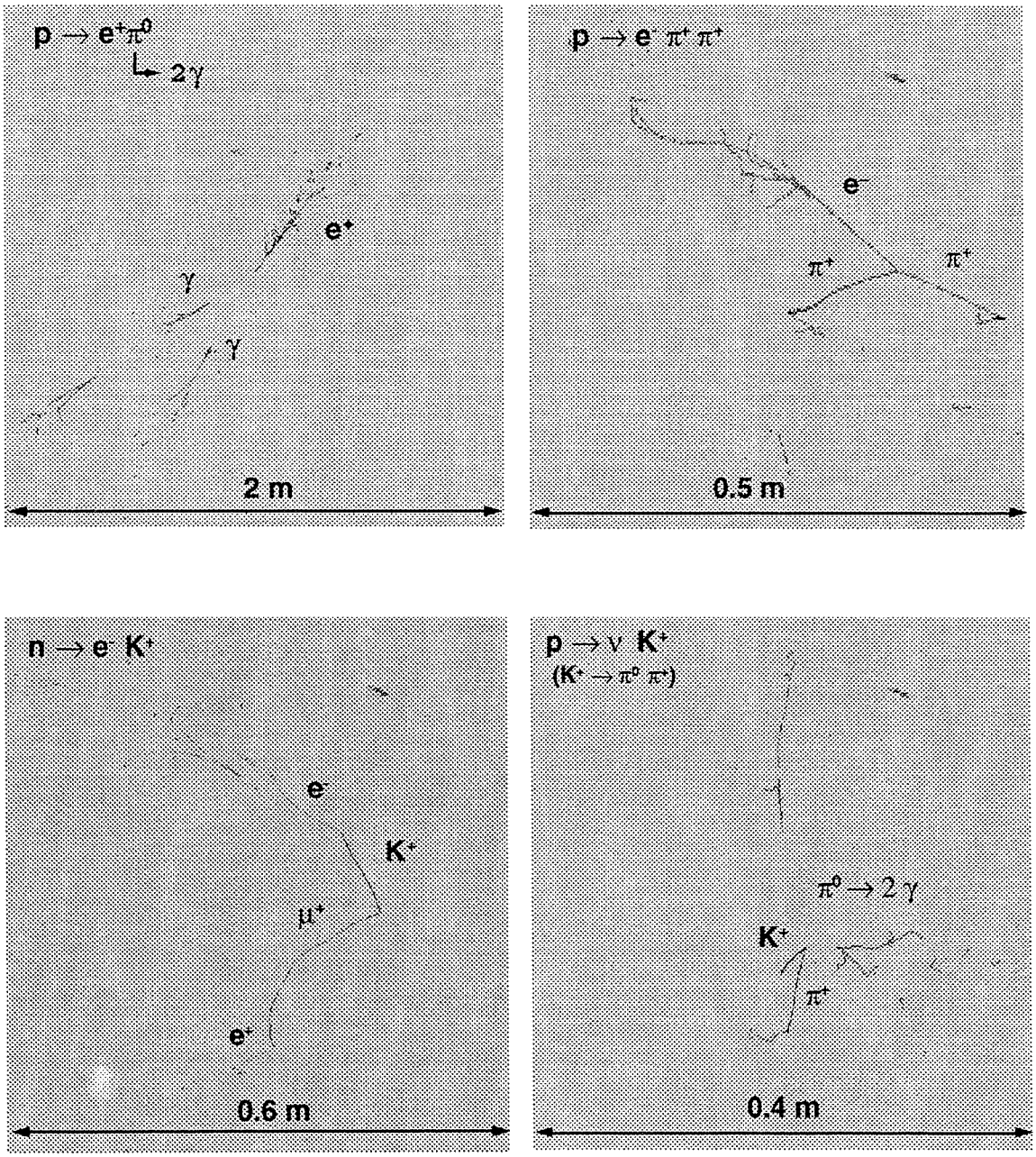

Figure 5: Simulation of selected nucleon decays. The dimensions are indicated on each figure.

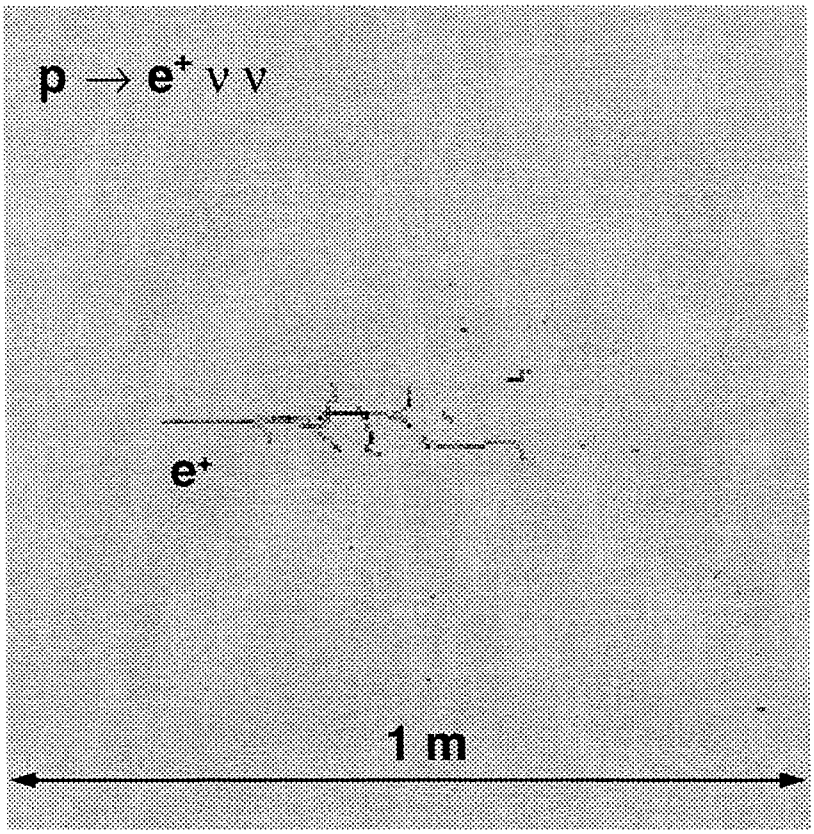

Figure 6 : Simulation of a $p \rightarrow e^+ \nu \nu$ event in ICARUS. In this event the electron has an energy of 390 MeV.

1.1 Simulation of proton decays inside the argon nucleus

In this section we describe in some detail the Monte Carlo simulation used to compute the detection efficiencies presented in the previous section. The method consists in evaluating the probability that, for nucleons decaying inside the argon nucleus, their decay products come out of the nucleus without interacting.

The distributions of nucleons in space within the nucleus and of their momenta was taken from the Saxon–Wood model [15]. The nuclear matter is distributed according to:

$$f(r) = \frac{N}{1 + e^{\frac{r-R}{a}}} \tag{4}$$

where $R = r_0 \times A^{1/3}$, r_0 = 1.07 fm and a = 0.545 fm, all determined from electron–nucleus scattering data. N is a normalization factor. For a nucleon at a distance r from the centre of the nucleus the momentum ranges from 0 to p_{max} with:

$$p_{max} = \frac{p_0}{1 + e^{\frac{r-R}{a}}} \tag{5}$$

where $p_0 = 228 \times (Z/A)^{1/3}$ MeV/c. The nucleons are assumed to be in a potential hole of the following shape:

$$E(r) = \frac{E_0}{1 + e^{\frac{r-R}{a}}} \tag{6}$$

where E_0 was taken to be 26.5 MeV for protons (18.5 MeV for neutrons) in order to reproduce nuclear binding energy data. Mesons coming from the nucleon decay are tracked through the nucleus in order to compute the reinteraction probabilities. Secondary particles eventually produced are then reprocessed in the same way. At present, the simulation program includes the quasi-elastic scattering and charge-exchange process for pions and kaons off nucleons. For the neutral members, the cross-sections have been obtained by isospin considerations from the experimental data for the charged partners. Because of its short decay length the ρ meson is considered to decay freely and the reinteraction probability is then computed for its decay products.

The nucleon decay code has been included as an event generator interfaced with the detector simulation program which is a standard GEANT 3.15 application [13]. To obtain the correct detector response, at tracking time, the ionization energy loss given by GEANT is converted into drift charge by means of Birk's formula which takes into account the increase of recombination probability with ionization density:

$$dQ = \frac{\alpha \, dE}{1 + k\frac{dE}{dx}} \tag{7}$$

where α and k are set respectively to 33 000 electrons per MeV and 0.096 cm/MeV in order to reproduce the data on stopping muons obtained in our 3-ton prototype with a drift electric field of 500 V/cm (see Chapter V). The coordinates are then digitized according to the selected wire pitch (5 mm) and the result is saved in two matrices (XZ and YZ) representing the response of the two orthogonal wires planes. A Gaussian noise (1000 electrons r.m.s.) is then superimposed on the result stored in the matrices at the end of each event, the events shown in these pages are just a plot of these matrices.

For each of the decay modes considered (Table 1), 2000 events were simulated. We have taken the conservative approach of rejecting all events with a nuclear reinteraction. All other events were reconstructed. The detection efficiency that appears in formula (3) reduces to the fraction of events that freely escape the argon nucleus. The largest source of error in the estimation of the reinteraction probability comes from the specific model used for the computation. We compared our results for the channel $p \rightarrow e^+ \pi^0$ with other results obtained by other simulations using the same model of the nucleus. We found good agreement, for instance, with the values of Reference [16] where a procedure very similar to ours has been adopted; but there is a certain discrepancy between our results (38% of non-interacting π^0's in iron) and the ones reported in Reference [14] (48%). This difference can be attributed to the different treatment of the pion–nucleon interaction. Experimental data on pion-nucleus scattering are consistent with both results [14], so we may take this difference as an estimate of the systematic error.

Table 3 : Sensitivity of ICARUS for various proton and neutron decay modes and for a data-taking period of five years. The sensitivity is the 90% C.L. limit expressed in years and for one module. The number of events given corresponds to a nucleon lifetime of 10^{33} years

Decay mode	Sensitivity	Events
$p \rightarrow e^+ \pi^0$	1.2×10^{33}	2.7
$p \rightarrow \bar{\nu} \pi^+$	1.2×10^{33}	2.7
$p \rightarrow \mu^+ \pi^0$	1.5×10^{33}	2.4
$p \rightarrow \bar{\nu} K^+$	2.4×10^{33}	5.4
$p \rightarrow e^+ \pi^+ \pi^-$	3.5×10^{32}	0.8
$p \rightarrow e^+ \rho^0$	2.4×10^{32}	0.5
$p \rightarrow e^+ e^+ e^-$	2.7×10^{33}	6.4
$n \rightarrow e^+ \pi^-$	1.4×10^{33}	3.1
$n \rightarrow \mu^+ \pi^-$	1.2×10^{33}	2.9
$n \rightarrow \nu \pi^0$	1.4×10^{33}	3.3
$n \rightarrow e^- K^+$	2.9×10^{33}	6.6
$n \rightarrow e^+ \rho^-$	3.0×10^{32}	0.6
$n \rightarrow e^+ \pi^- \pi^0$	4.1×10^{32}	1.0
$n \rightarrow e^+ e^- \nu$	3.3×10^{33}	7.8

We have performed a complete study of only some of the proton decay modes of interest, using the simulation procedure described in Section 1.2. Similar studies are under way. However, our detailed study of three characteristic decay modes (Table 2) indicates, that, except for channels such as $p \rightarrow e^+ \nu \nu$ for which the topology is identical to that of atmospheric ν_e charged-current events, the background corresponding to a data-taking period of one year is negligible. In order to obtain a preliminary estimate of the sensitivity of ICARUS, we have assumed that for all the other decay modes the background is indeed also negligible. Table 3 lists some of the main nucleon (proton and neutron) decay modes which will be considered with the 90% confidence level limits on the corresponding lifetime, for one module and for five years, which represents a minimum exposure time for ICARUS. The decay mode list is only indicative, a priori all decays can be searched for.

It is interesting to note here that the availability of a CERN neutrino beam aimed at the Gran Sasso Laboratory would offer the possibility to directly simulate, if needed, some of the nucleon decay backgrounds.

1.2 Simulation of atmospheric neutrino background

We have studied the atmospheric neutrino background to nucleon decay by means of a Monte Carlo simulation. The detector simulation is the one described in Section 1.1 with, in addition, an online display and full reconstruction of the events. The generation of atmospheric neutrino events uses the same generator used in Section 2.3. We report here the study for two specific channels: $p \rightarrow e^+ \pi^0$ and $p \rightarrow e^+ \nu \nu$ for which we generated a sample of proton decay events randomly mixed with a sample of atmospheric neutrino events. Proton decay candidates were then selected out of the whole sample by means of appropriate selection cuts, described below for the specific cases studied, and a visual scan was performed.

1.2.1 $p \rightarrow e^+ \pi^0$

This is the most standard decay mode, as it is the one originally predicted by the minimal SU(5) theory. The event signature is three, coplanar electromagnetic showers (one from the e^+ and two from the π^0) with a total energy ~ 938 MeV and a total momentum near zero. We generated a sample of 510 $p \rightarrow e^+ \pi^0$ events and a sample of 499 atmospheric neutrino events from ν_e and $\bar{\nu}_e$ charged-current interactions only, since they are the ones expected to have a topology which could possibly be similar to the specific proton decay channel studied here. All of these events were visually scanned, and proton decay candidates were selected according to the following criteria:

a) Total reconstructed energy E_{tot} such that: 700 MeV < E_{tot} < 1 GeV;

b) Two or three showers in each one of the two orthogonal event views and no other track;

c) No obvious momentum imbalance.

With these criteria 186 events were selected, all were proton decays, none were atmospheric neutrino events. This number is consistent within statistics with the efficiency of 42 % given in Table 1.

In the initial sample of 510 proton decay events generated, 177 events had no reinteraction with the argon nucleus, the other events had a reinteraction. Among the 186 events selected, 169 were decays without reinteraction in the argon nucleus. Only in 17 events did a π^0 reinteraction occur. The efficiency for selecting non-reinteraction events is therefore high (95.5%) while it is fairly low for reinteraction events (5%). This justifies fully the assumption made in the previous section of considering only events in which the nucleon decay products did not interact with the argon nucleus. However, it should be noted that with more sophisticated selection criteria it should be possible also to make use of reinteraction events and to further increase the ICARUS sensitivity.

1.2.2 $p \rightarrow e^+ \nu \nu$

The most important source of background for this channel is also charged-current interactions of atmospheric ν_e's and $\bar{\nu}_e$'s. Proton decay events will consist of one isolated electromagnetic shower with energy between 0 and 500 MeV. We generated 519 $p \rightarrow e^+ \nu \nu$ events and 1981 atmospheric-neutrino charged-current events. We used the following selection criteria:

a) Total reconstructed energy E_{tot} such that: 150 MeV $< E_{tot} <$ 450 MeV;

b) One single electromagnetic shower in each of the two orthogonal event views.

With these criteria, 399 proton decay events (detection efficiency 76.9% ± 1.9%) and 45 atmospheric neutrino events were selected by visual scanning. Since we expect to have 250 atmospheric ν_e and $\bar{\nu}_e$ charged-current events per module per year in this energy range, we conclude that the annual background in this proton decay channel is 5.7 ± 0.8 ± 1.7 events per module. The first error is statistical and the second one reflects the present 30% uncertainty in the atmospheric neutrino flux. The precise measurement of the atmospheric neutrino flux is part of the ICARUS programme, we will therefore be able to reduce significantly the systematic error on the background normalization. In addition the systematic study of topologies of atmospheric-neutrino events should allow us to find more refined criteria to reject further this type of background. We note that most of the atmospheric neutrino events were rejected because they contain a proton or a pion track accompanying the electron shower. In most cases these tracks were relatively short (1 to 2 cm) and in some cases they appeared as a bulb of ionization deposition near the start of the electron shower. This demonstrates well the power of the ICARUS technique and, in particular, the importance of the ionization density measurement.

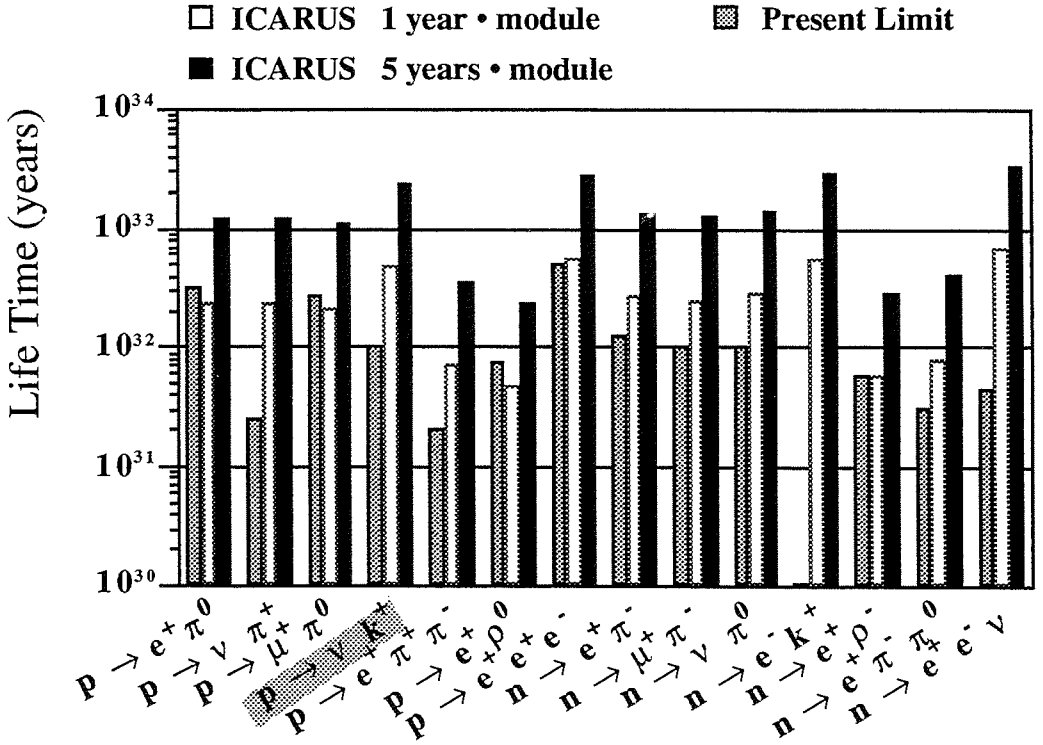

Figure 7: Comparison of present nucleon decay limits with the sensitivity of ICARUS for one and five years

In summary, many nucleon decay modes can be searched for simultaneously and, after only one year of data taking, ICARUS will reach or exceed most present limits (Figure 7). The equivalent of five years of data will

take us to the unexplored region between 10^{33} and 10^{34} years for some of the most relevant channels.

1.3 Search for neutron–antineutron oscillation in the ^{40}Ar nucleus

Some GUT models [17] predict $\Delta B = 2$, $\Delta L = 0$ baryon number non-conserving interactions leading to neutron–antineutron oscillations. Now that the minimal SU(5) has been rejected, it seems important to test $\Delta B = 2$ processes.

Although the most direct test of neutron–antineutron oscillations is the study of the spontaneous transitions in a free neutron beam [18], in principle it is also possible to search for an antineutron annihilation in a huge quantity of matter containing bound neutrons and taking into account the big reduction factor due to the effect of the nuclear potential inside a nucleus such as the ^{40}Ar nucleus [19].

An antineutron from a neutron–antineutron oscillation in a ^{40}Ar nucleus annihilates with a nucleon, producing an average of 5 pions (3 charged and 2 neutral). The efficiency for detecting this type of events is very high, comparable to that of the proton decay.

We estimate here the limit that ICARUS can set in one year of running with one module (assuming 100% efficiency):

– the number of neutrons in 4.7 kton of ^{40}Ar is $\sim 1.5 \times 10^{33}$;

– in one year (3×10^7 s), if no events are observed, the corresponding limit for neutron–antineutron oscillations for bound neutrons is:

$T_0 = (1.5 \times 10^{33} \times 3.15 \times 10^7) / 2.3 = 2.12 \times 10^{40}$ s (90% C.L.);

– to obtain the corresponding limit for free neutrons, we must apply a reduction factor (T_R) which is of the order of 1.3×10^{23} s^{-1}, as suggested in the work by Dover, Gal and Richard [19] for ^{16}O and ^{56}Fe nuclei. This leads to the following limits:

$$\tau_{n\bar{n}} > \sqrt{\frac{T_0}{T_R}} = \sqrt{\frac{2.12 \times 10^{40}}{1.3 \times 10^{23}}} = 4.0 \times 10^8 s \qquad (90\%\ \text{C.L.})$$

Therefore, in ten years of running with one module, we will reach a limit of $\tau_{n\bar{n}} > 1.27 \times 10^9$ s (90% C.L.) which is significant since it is one order of magnitude longer than the present limit of $\tau_{n\bar{n}} > 1.2 \times 10^8$ s (90% C.L.) [20].

1.4 References

[1] R.V. Eötvös, D. Pekar, F. Fekete, Ann. Physik **68** (1922) 11; J. Renner, Mat. Term. Ert. **53** (1935) 542; P.G. Roll, R. Krotkov, R.H. Dicke, Ann. Phys. **26** (1964) 442; V.B. Braginsky, V.I. Panov, Sov. Phys. JETP **34** (1972) 463.

[2] See e.g. A.D. Dolgov, M.V. Sazhin, Ya.B. Zeldovich, *Basics of Modern Cosmology*, Ed. Frontières, 1990.

[3] For a review see e.g. P. Langacker, Phys. Rep. **C72** (1981) 185.

[4] For a review, see R. Barloutaud, Theoretical Aspects of Underground Physics, Proc. of Toledo Workshop, Nucl. Phys. B (Proc. Suppl. **28A**) (1992) p. 437.

[5] P. Langacker and M. Lou, Phys. Rev. **D44** (1991) 817 and P. Langacker, *Particles, Strings, and Cosmology*, ed. P. Nath and S. Reucroft (World Scientific, Singapore, 1991), p. 237.
[6] U. Amaldi, W. de Boer and H. Fürstenau, Phys. Lett. **B 260** (1991) 447.
[7] P. Langacker, University of Pennsylvania preprint UPR–0539 (1992).
[8] For a review, see Graham G. Ross, *Grand Unified Theories*, (Benjamin–Cummings, Menlo Park, 1984).
[9] R. Arnowitt, Proc. Int. Europhys. Conf. on High Energy Physics, Marseille, 1993.
[10] W.A. Mann, T. Kafka and W. Leeson, Phys. Lett. **B291** (1992) 200.
[11] J. Pati, A. Salam and U. Sarkar, Phys. Lett. **B133** (1983) 330.
[12] J. Pati, Phys. Rev. **D29** (1984) 1549.
[13] R. Brun et al., CERN report DD 85–1 (1985).
[14] C. Berger et al., Z. Phys. **C 50** (1991) 385.
[15] E. Fermi, in *Nuclear Physics*, ed. J. Orear (Univ. of Chicago Press, 1950).
[16] P. Balzarotti et al., internal note, INFN, Milano (1987).
[17] For a recent review see R.N. Mohapatra Nucl. Instrum. Meth. **A284** (1989) 1.
[18] G. Fidecaro et al., Phys. Lett. **156B** (1985) 122; G. Bressi et al., Il Nuo. Cim. **103A** (1990) 731; M. Baldo Ceolin et al., Phys. Lett. **236B** (1990) 95.
[19] W.M. Alberico et al., Phys. Lett. **114B** (1982) 266; C.B. Dover, A. Gal and J.M. Richard, Phys. Rev. **C31** (1985) 1423.
[20] M. Takita et al., Phys. Rev. **D34** (1986) 902; C.H. Berger et al., Phys. Lett. **240B** (1990) 237.

2. Atmospheric neutrinos

2.1 The atmospheric neutrino puzzle: observation of small ν_μ/ν_e ratios

Atmospheric neutrinos, i.e. those originating from the interactions of the primary component of cosmic rays with the Earth's atmosphere, are the ultimate background for nucleon decay search. This in itself justifies fully a detailed study. Recently, however, very puzzling data came from early studies of atmospheric neutrinos and the issue has become central to the understanding of neutrino properties. Atmospheric neutrinos originate mainly from the decays of π's, K's and μ's produced in cosmic-ray-induced air showers (Figure 1). On general grounds, one expects the ratio of the number of ν_μ's and $\bar{\nu}_\mu$'s to ν_e's and $\bar{\nu}_e$'s to be approximately equal to two. A large number of contained neutrino interactions (events which are contained within the detector acceptance) have been recorded in the large nucleon-decay detectors. Initially it was found that the fraction of events with a muon in the final state was smaller than expected. This fact was largely ignored until the Kamiokande group separated muons from electrons in the observed neutrino interactions and found that the ratio of muons to electrons was indeed smaller than expected. This result could be interpreted as a possible hint for neutrino flavour oscillations, if one assumes that the smallness of the ratio comes from a depletion of the muon neutrinos.

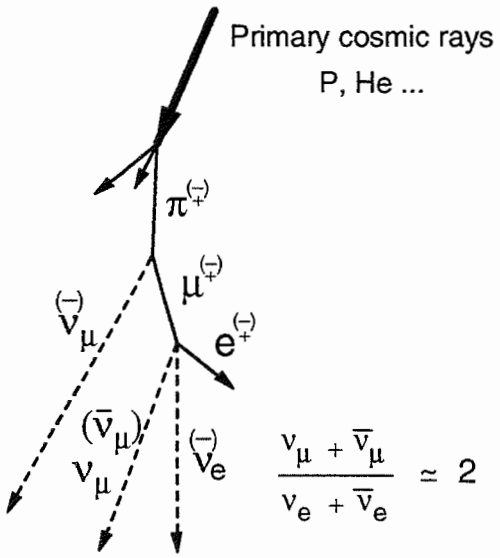

Figure 1 : Mechanisms for the production of neutrinos and antineutrinos in cosmic-ray showers

Soon after, the other proton decay collaborations, namely IMB, NUSEX, Fréjus, and recently Soudan-2, checked their own data on atmospheric neutrinos (Table 1). An interesting and puzzling result came out: the two water-Cherenkov detectors (IMB and Kamiokande) did observe an apparent muon-to-electron ratio anomaly, while the NUSEX and Fréjus iron-calorimeter detectors did not. The third iron-calorimeter detector, Soudan-2, instead agrees with the water-Cherenkov experiments, finding a small muon-to-electron ratio, however with small significance. The initial prejudice that a

systematic effect of the water-Cherenkov technique was responsible for this unexpected result is thus weakened, although the preliminary result of Soudan-2 is statistically still limited. One should note that both Fréjus and NUSEX results also have a poor statistical accuracy, and in any case these experiments will not collect more data since they have been terminated.

Table 1: Summary of present atmospheric neutrino data. For each experiment the ratio R as defined in the text above is given with its error.

Experiment	Exposure (kton.year)	R
Kamiokande [1]	4.90	$0.60^{+0.07}_{-0.06} \pm 0.05$
IMB–3 [2]	7.70	$0.54 \pm 0.02 \pm 0.07$
Fréjus [3]	1.56	0.87 ± 0.21
NUSEX [4]	~ 0.40	0.99 ± 0.40
Soudan–2 [5]	1.01	$0.69 \pm 0.19 \pm 0.09$

The atmospheric neutrino analysis is generally performed by studying the $(\nu_\mu/\nu_e)^{obs}$ ratio of charged-current interaction events observed in the detector, and comparing it with the $(\nu_\mu/\nu_e)^{MC}$ ratio predicted by a model of cosmic-ray interactions with the Earth's atmosphere. Since the largest uncertainty in the prediction comes from the knowledge of the absolute value of the initial neutrino flux, as large as 30%, it is desirable to study the quantity least sensitive to that flux, namely the ratio of ν_μ to ν_e events. In Table 1 the results on contained atmospheric neutrinos events, are described in terms of the double ratio R:

$$R = \frac{\left(\frac{\nu_\mu + \bar{\nu}_\mu}{\nu_e + \bar{\nu}_e}\right)^{obs}}{\left(\frac{\nu_\mu + \bar{\nu}_\mu}{\nu_e + \bar{\nu}_e}\right)^{MC}}$$

The situation is even more confused if one considers also the analysis of upward-going muons, i.e. those muons produced by higher energy neutrino interactions in the rock underneath the detector. IMB, Kamiokande and Baksan experiments, all claim agreement between data and prediction. It is worth mentioning that this result depends very much on the neutrino flux calculation (in particular the ν_μ flux calculation) and should therefore be considered with care.

The interpretation of the small R ratio in terms of neutrino oscillations suggests two main possible channels ($\nu_\mu \leftrightarrow \nu_e$) and ($\nu_\mu \leftrightarrow \nu_\tau$), assumed, for simplicity, to be independent and separated. (A possible ν_μ oscillation into a sterile, i.e. right-handed neutrino, of unknown mass and flavour has not been explored yet.)

The present constraints on the oscillation parameters (Δm^2, $\sin^2 2\theta$) (Figure 2) result in a possibly allowed region (shaded area) mainly from the Kamiokande data, limited, in the ($\nu_\mu \leftrightarrow \nu_e$) channel, by both the Fréjus

atmospheric neutrino results and the Gosgen reactor neutrino experiment, and for the ($\nu_\mu \leftrightarrow \nu_\tau$) channel by the Fréjus and CDHS accelerator neutrino results. One should note that there are also Baksan data [6] which take away the allowed region completely, but those data have a very large systematic error because their interpretation depends strongly on the absolute flux prediction.

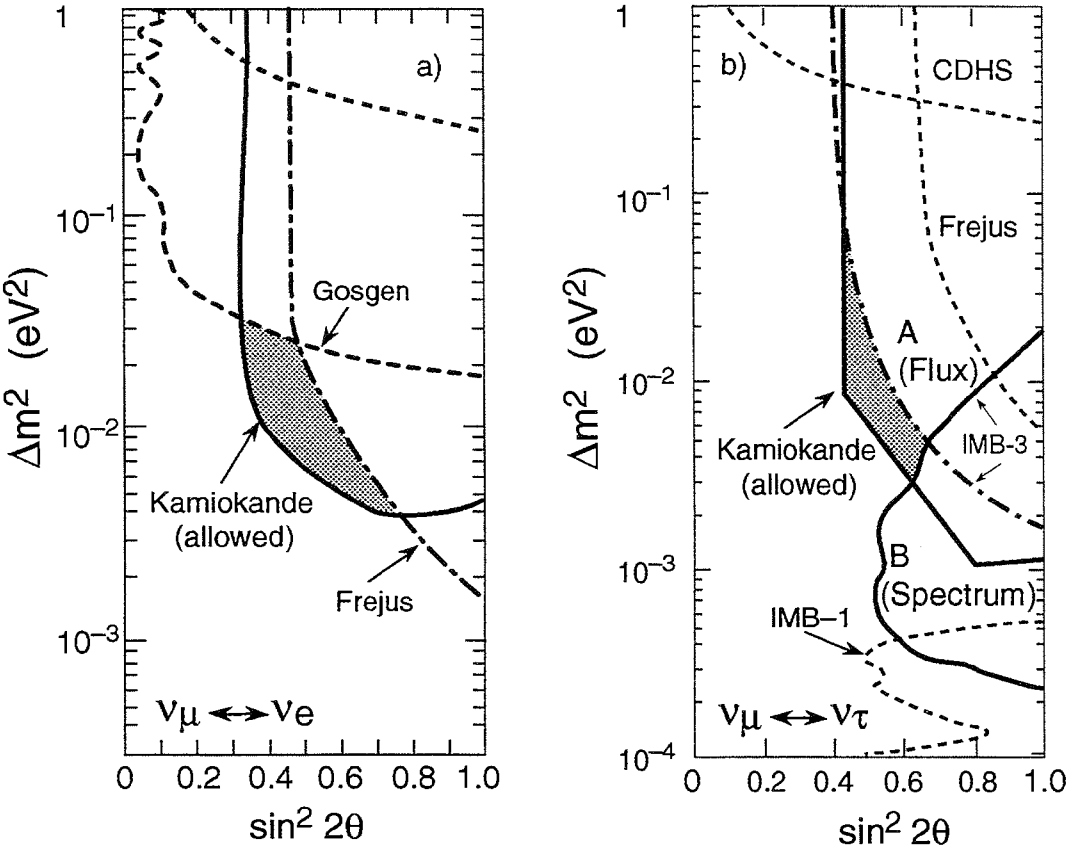

Figure 2 : Present experimental limits on (a) $\nu_\mu \leftrightarrow \nu_e$ and (b) $\nu_\mu \leftrightarrow \nu_\tau$ oscillations from atmospheric neutrinos. Curves A & B are from IMB-3 up-going muon data [7].

These data seem to indicate large neutrino mixing angles and relatively large mass differences (or, alternatively, short oscillation lengths). A very interesting point is that the solution in terms of ($\nu_\mu \leftrightarrow \nu_e$) oscillation is inconsistent with the solar neutrino results, which require Δm^2 of the order of 10^{-5} eV^2. This makes the ($\nu_\mu \leftrightarrow \nu_\tau$) interpretation of the atmospheric neutrino data the favoured one.

It is worth mentioning in addition that a crucial test is going to be pursued by a joint collaboration of Kamiokande and IMB to check their electron–muon identification algorithms, using an electron and muon beam from the KEK proton-synchrotron. If the particle recognition and energy calibration turn out to be correct, the small $(\nu_\mu/\nu_e)^{obs}$ ratio will have to be taken very seriously.

The present data, even if confirmed, do not contain sufficient information to provide an explanation for the phenomenon. Therefore, to definitively clarify this crucial issue, a new-generation experiment is required which should provide large statistics, high discrimination between electrons

and muons, a high precision energy and direction measurement, and which, if possible, should also distinguish neutrinos from antineutrinos. This is precisely what the ICARUS technique can offer, and with a large safety margin because the energies involved, 25–3000 MeV, are large enough to produce very long and unambiguous tracks in the detector.

2.2 Atmospheric neutrinos and neutrino oscillations

Atmospheric neutrinos reaching a detector located near the Earth's surface, when produced from above, travel an average distance of a few tens of kilometres through the atmosphere. A distance up to $L = 2\ R_E \cos\psi$ (R_E is the Earth's radius and ψ is the zenith angle) is crossed through the Earth in the case of upward-going neutrinos produced in the bottom hemisphere with respect to the detector location (for a definition of the angular reference frame in use, see Figure 8). An oscillation length up to $\sim 1.3 \times 10^4$ km is thus experimentally available. In principle, this makes the upward-going atmospheric neutrino detection very appealing for oscillation studies. On the other hand, some limitations affect this method, the main one of these being statistics, even for a large detector.

In this Section we present the calculation of the atmospheric ν_μ and ν_e induced events in the ICARUS detector. For upward-going neutrinos, the effect of propagation through a variable density medium (e.g. along trajectories crossing the Earth at different incident zenith angles) has been taken into account to evaluate possible variations on the expected ν_μ and ν_e event rate. For this reason the oscillation probability has been calculated applying the MSW theory [8], (Sections 2.4.1 and 2.4.2). For downward-going neutrinos, oscillations may occur in vacuum and the transition probability depends upon the neutrino production altitude in the atmosphere (Section 2.4.3).

2.3 The atmospheric neutrino interaction rate in ICARUS

The calculation of the neutrino-induced event rate N_ν^{exp} expected in case of no oscillation (Section 2.3.3), is based on the convolution of the flux with the cross-section for neutrino interaction, in a detector with a given detection efficiency. To calculate this rate in ICARUS a new set of atmospheric neutrinos fluxes has been used (Section 2.3.1) and the interaction cross-sections on liquid argon have been calculated with a dedicated, new Monte Carlo generator (Section 2.3.2).

2.3.1 The atmospheric neutrino flux

The atmospheric neutrino fluxes are affected by several effects. The geomagnetic field acts differently on the primary spectrum for each geographical site; at a low magnetic latitude there is a higher energy cut-off on primaries which strongly suppresses the neutrino flux at low energy (< 1 GeV). This means that at a northern site, like Gran Sasso, the geomagnetic field has little effect on down-going neutrinos while it largely reduces the flux of up-going neutrinos, with a big up-to-down asymmetry. Another effect is due to solar activity which introduces a flux modulation

during the solar cycle (about 11 years). Finally, the muon polarization effect, namely the fact that the ν_e from μ decay is thrown forward relative to the ν_μ, reduces the ν_μ/ν_e ratio at fixed neutrino energy.

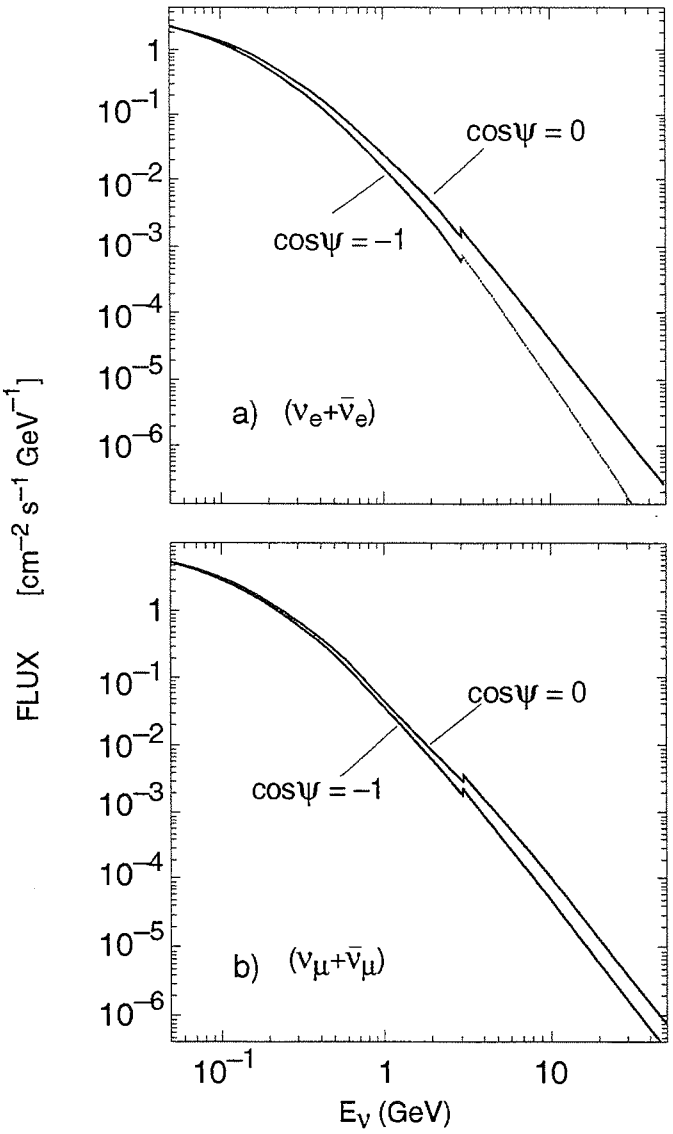

Figure 3: The atmospheric neutrino flux as a function of energy and for two values of ψ the zenith angle (a) for electron neutrinos and antineutrinos and (b) for muon neutrinos and antineutrinos.

All these factors have been taken into account in the Monte Carlo simulation developed by the Bartol group (T. Gaisser et al.) [9]. The fluxes actually in use in the following analysis, kindly provided by T. Stanev [10] a member of the Bartol group, are calculated for the Mont Blanc site (the geomagnetic difference with the Gran Sasso site is assumed to be negligible) and averaged over the solar cycle. These fluxes are given in a differential way both in energy (up to E_ν = 3 GeV) and in zenith angle (while the latest published spectra from Bartol are averaged on the zenith angle). The zenith angular dependence allows a more precise calculation of matter effect for up-going neutrinos. For energies higher than 3 GeV we used the Volkova fluxes [11].

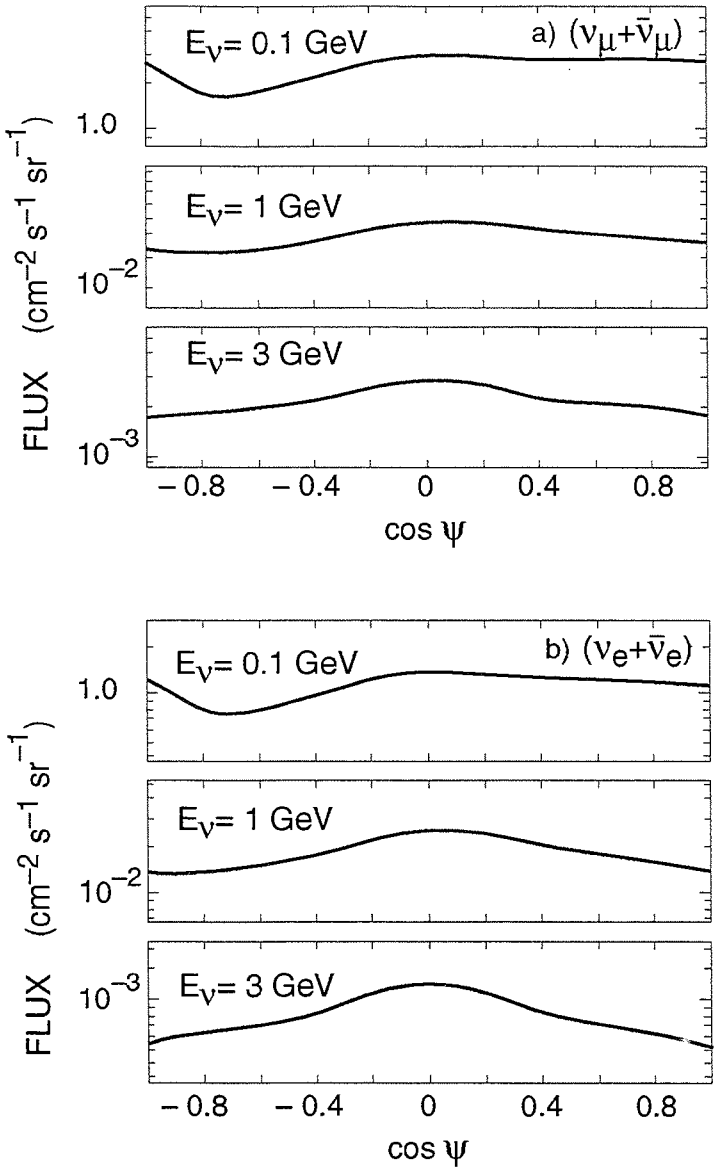

Figure 4: Variation of the atmospheric neutrino flux with the zenith angle (a) for muon neutrinos and antineutrinos and (b) for electron neutrinos and antineutrinos

In Figure 3, the resulting differential flux, as a function of neutrino energy, for two different incident angles of (ν_μ + $\bar{\nu}_\mu$) and (ν_e + $\bar{\nu}_e$) is presented. At E_ν = 3 GeV the mismatch between the two sets of curves is less than 10%.

In Figure 4 the differential flux as a function of zenith angle, at different energies, is also shown.

2.3.2 The neutrino-nucleon cross-section and the final-state kinematics

The atmospheric neutrino energy spectra indicate that the flux is mostly concentrated in a limited energy window below a few GeV. In this region, neutrino interactions with nucleons bound in nuclei happen mainly via quasi-elastic scattering and, as energy increases, via baryonic resonance excitation followed by pion production [12]. Inelastic scattering with multi-

pion production in the final state becomes important at higher energy and its contribution in the few GeV region is small.

In the interaction of neutrinos with nucleons bound in heavy nuclei, several important factors have to be taken into account in addition to the kinematics of the reaction on free nucleons: the effects of nucleons' Fermi motion, binding energy, Pauli blocking of the recoil nucleon, and, when π's are produced, charge exchange, scattering and absorption inside the nucleus. All these 'nuclear effects' modify the final-state kinematics and ultimately the cross-section of interaction of neutrinos on nucleons.

Monte Carlo techniques are best suited to calculate total and partial channel cross-sections and the kinematics (energy and angular distributions) of the final-state components.

Therefore, a new Monte Carlo event generator (GENEVE) has been developed for ICARUS to reproduce neutrino interactions on liquid argon. The details of such a Monte Carlo are described elsewhere [13] and we only mention here some of its basic features. The charged-current reactions implemented in the generator are:

$$\nu_{\mu,e}\,(\bar{\nu}_{\mu,e}) + N \rightarrow \ell^{\pm} + N'$$

$$\nu_{\mu,e}\,(\bar{\nu}_{\mu,e}) + N \rightarrow \ell^{\pm} + \Delta \rightarrow \ell^{\pm} + \pi^{\pm,0} + N'$$

$$\nu_{\mu,e}\,(\bar{\nu}_{\mu,e}) + N(q_V) \rightarrow \ell^{\pm} + (1 \text{ or } 2)\,\pi^{\pm,0} + N'$$

where N stands for proton or neutron, ℓ for μ or e and q_V's are the valence quarks in the nucleon. In total there are seven possible reactions. Our program also provides neutral-current reactions with ν ($\bar{\nu}$) replacing the charged lepton in the above reaction final states.

In the simulation, the energy of the incident neutrino is randomly distributed according to the atmospheric neutrino flux; the Fermi motion of the nucleon in the argon nucleus follows a Fermi distribution, with a Fermi momentum k_F = 0.246 GeV, modified to include a tail at high momenta, to take into account nucleon–nucleon correlations in the nucleus. An 'on-shell' dynamics is used to guarantee energy and momentum conservation.

In the form factors for quark–electron scattering and Δ production the Vector and Axial masses are M_V = 1.07 GeV and M_A = 0.98 GeV respectively, following the experimental world-average values. The invariant mass spectrum for the hadronic system in the case of Δ resonance production is generated according to the data available from Gargamelle, BNL and CHARM experiments. Finally, the total cross-section and the relative rates in the various channels are also normalized to experimental data to take into account the effect of pion scattering and absorption inside nuclei (a feature not included in the present Monte Carlo code).

In Figure 5 the total cross-sections for charged-current interactions of neutrinos on argon nuclei, as a function of the incident neutrino energy, are shown separately for $\nu_\mu, \bar{\nu}_\mu$ and $\nu_e, \bar{\nu}_e$.

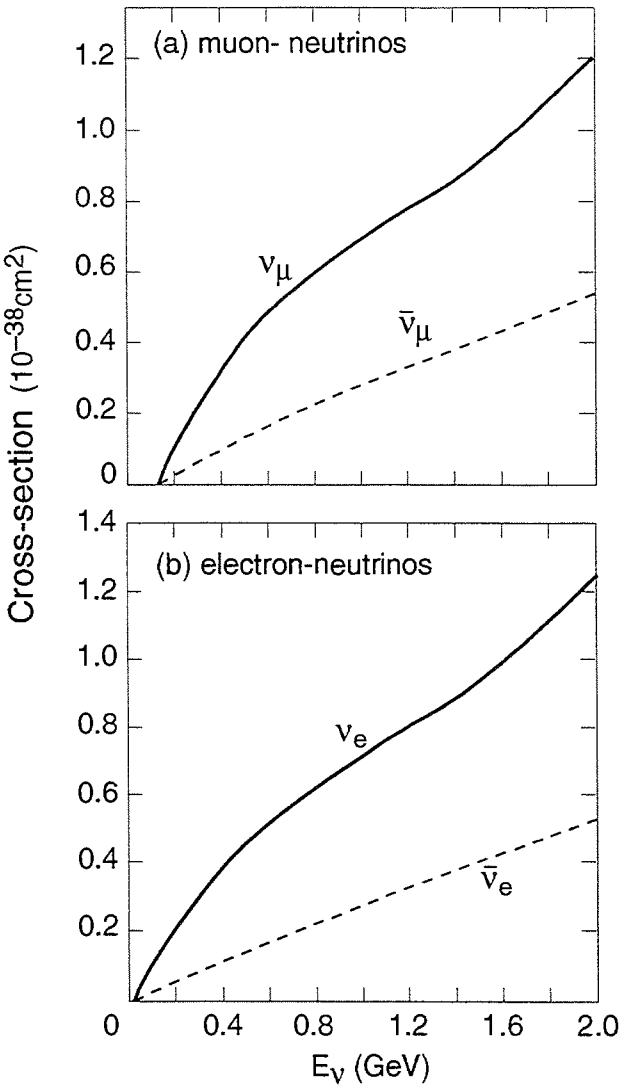

Figure 5: Cross-sections for neutrino scattering on argon (a) for muon neutrinos and (b) for electron-neutrinos, as a function of the incident neutrino energy

2.3.3 Expected rates

The atmospheric neutrino interaction rate in ICARUS must be evaluated, as mentioned above, taking into account the detector efficiency. At this stage we simply assume a full efficiency ($\varepsilon = 1$) and we calculate the charged-current event rate (without oscillations) for an ideal 5 kton liquid argon detector, and for an exposure of one year.

With these assumptions, in Table 2 we give the expected number of events for the various neutrino species, integrating over two different solid-angle regions of $\Delta\Omega = 2\pi$, corresponding to the top and bottom hemispheres seen by ICARUS.

Table 2 : Number of events in top and bottom hemispheres for electron and muon neutrinos

	ν_μ	$\bar{\nu}_\mu$	ν_e	$\bar{\nu}_e$	Total
Top	291	106	212	67	676
Bottom	253	94	177	57	581

The $(\nu + \bar{\nu})$ interaction yields per 10 MeV neutrino energy bin are shown in Figure 6. Charged-current ν_μ reactions may only occur above an energy threshold of $E_\nu \approx 130$ MeV $\approx m_\mu$. For electron-neutrino interactions the energy threshold is much lower (≈ 25 MeV) but much larger than the electron mass because of the Pauli blocking effect. Figure 6 shows that a fraction of about 12% of the $(\nu_e + \bar{\nu}_e)$ events are concentrated below the ν_μ energy threshold.

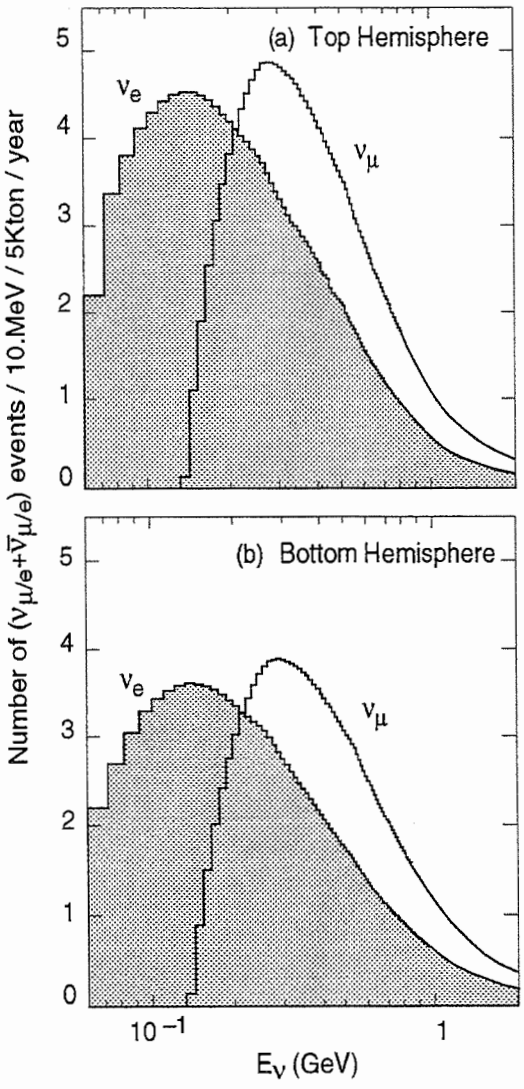

Figure 6 : Number of neutrino and antineutrino events as a function of neutrino energy for (a) the top hemisphere and (b) the bottom hemisphere

The dependence on the zenith angle of the interaction yields (per $\Delta\cos\psi$ = 0.05 angular bin) are shown in Figure 7, separately for the two hemispheres considered.

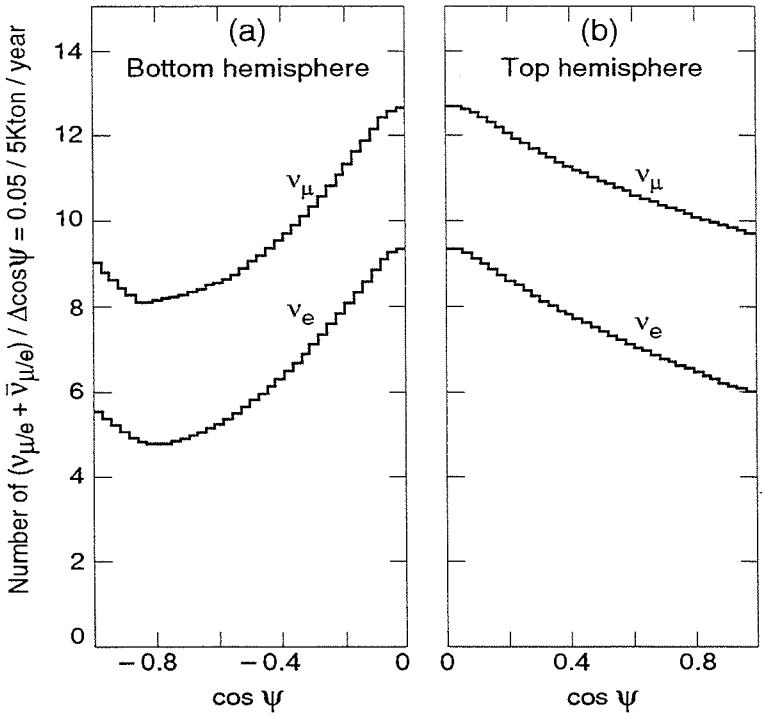

Figure 7: Number of neutrino and antineutrino events expected in the energy range 0.02 to 100 GeV, as a function of zenith angle (a) in the bottom hemisphere and (b) in the top hemisphere

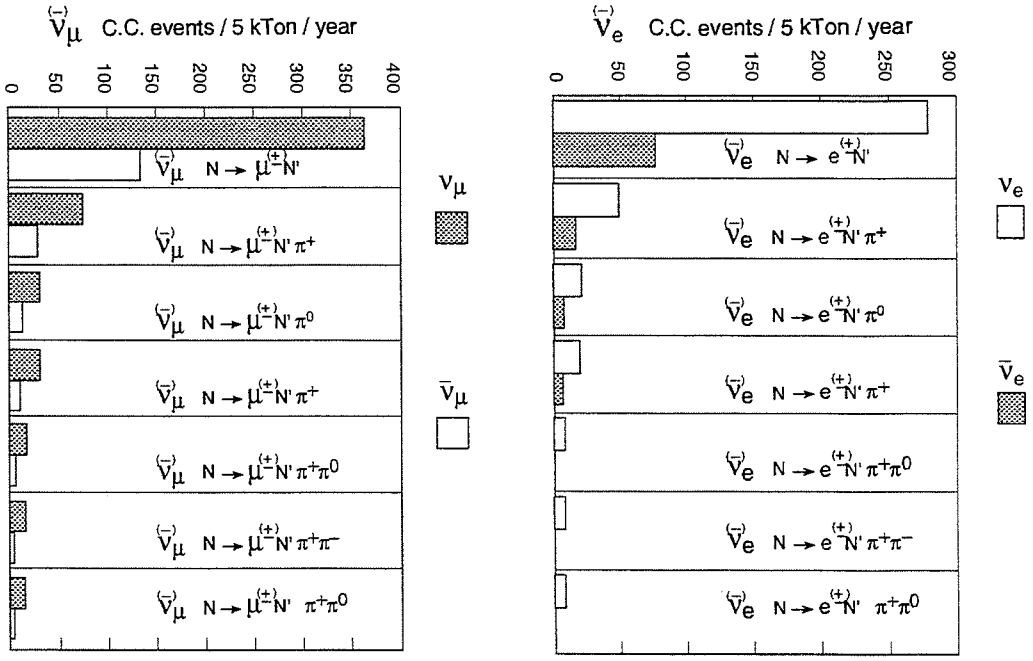

Figure 8 : Event rate distribution amongst the different decay channels, for charged-current reactions and for one year of exposure of the 5 kton ICARUS detector

The event rate distribution amongst the decay channels included in our Monte Carlo simulation is shown in Figure 8. The quasi-elastic channel, with a single lepton track in the final state (accompanied by a spectator proton) contributes about 70% of the total neutrino event rate.

2.4 Sensitivity to neutrino oscillations

2.4.1 Upward-going neutrinos through the Earth

In this analysis the neutrino mass hierarchy is assumed to follow the charged lepton sector, namely $m_{\nu e} < m_{\nu \mu} < m_{\nu \tau}$.

In principle, all possible mixing between the three neutrino families can be considered. However, if the masses are well separated, in the energy range where large ($\nu_e \leftrightarrow \nu_\mu$) transitions take place, only a small contamination occurs from ν_τ. Alternatively, at higher energies, where ν_e and ν_τ are fully mixed, there will be only a small contamination from ν_μ. In both cases, as shown in [14], the contamination due to the extra neutrino flavour can be neglected, allowing one to use the simple two-neutrino-families scheme for a separate search for ($\nu_e \leftrightarrow \nu_\mu$) transitions and for ($\nu_e \leftrightarrow \nu_\tau$) transitions.

In the atmospheric neutrino sample there are no ν_τ's and those from converted ν_e's do not have enough energy to be detected through charged-current reactions. The only detectable effect of ($\nu_e \leftrightarrow \nu_\tau$) transitions would be a relatively small decrease in the ν_e counting rate. This makes the search for ($\nu_e \leftrightarrow \nu_\tau$) oscillation difficult and less attractive than the search for ($\nu_e \leftrightarrow \nu_\mu$).

The ($\nu_\mu \leftrightarrow \nu_\tau$) oscillation is the simplest and most often made hypothesis to explain the contained events anomaly in the present experimental data (Section 2.1). However, since both of these neutrino flavours have identical interaction with matter, the transition is not affected by the presence of matter in the Earth.

The following analysis will be devoted to determining the ICARUS sensitivity to ($\nu_e \leftrightarrow \nu_\mu$) transitions, showing, in particular, how matter effects can be relevant.

Upward-going neutrinos may undergo oscillations enhanced by matter effects, depending on the path length and energy. For a precise calculation of the oscillation probability, the bottom hemisphere has been divided in several zenith angular sectors ($\Delta\psi$); for each of these sectors neutrino energy spectra were calculated integrating over a solid angle $\Delta\Omega = 2\pi\,\Delta\psi$ (Figure 9). Path lengths across the Earth, connecting the detector with the centre of each sector, were associated to the corresponding spectra.

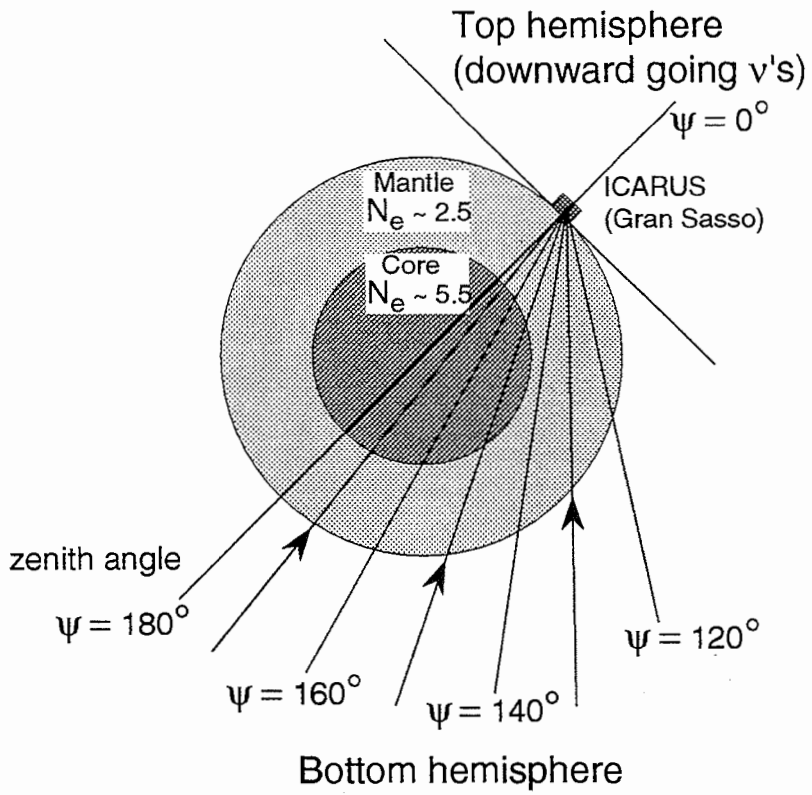

Figure 9 : Schematic diagram of the Earth showing the definition of top and bottom hemispheres and of zenith angle

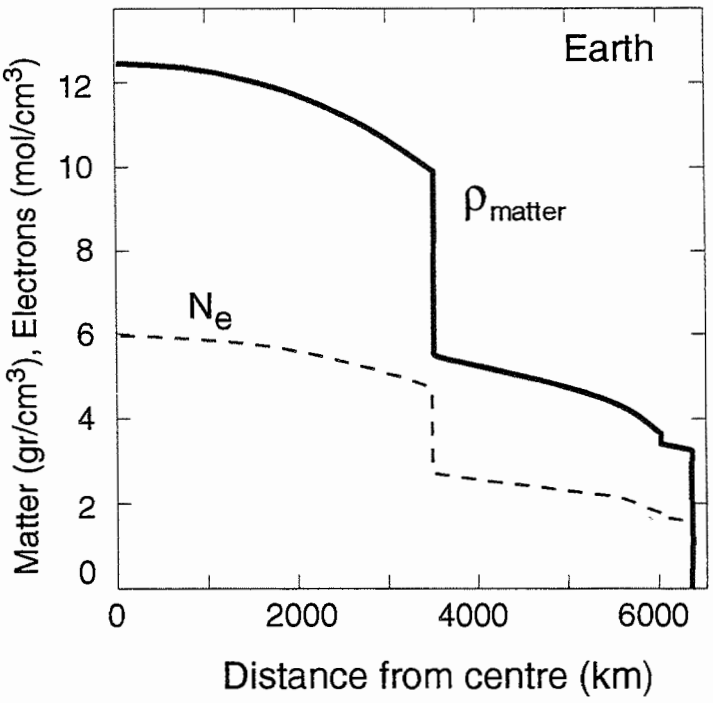

Figure 10 : The density of matter and of electrons in the Earth as a function of the distance from the centre

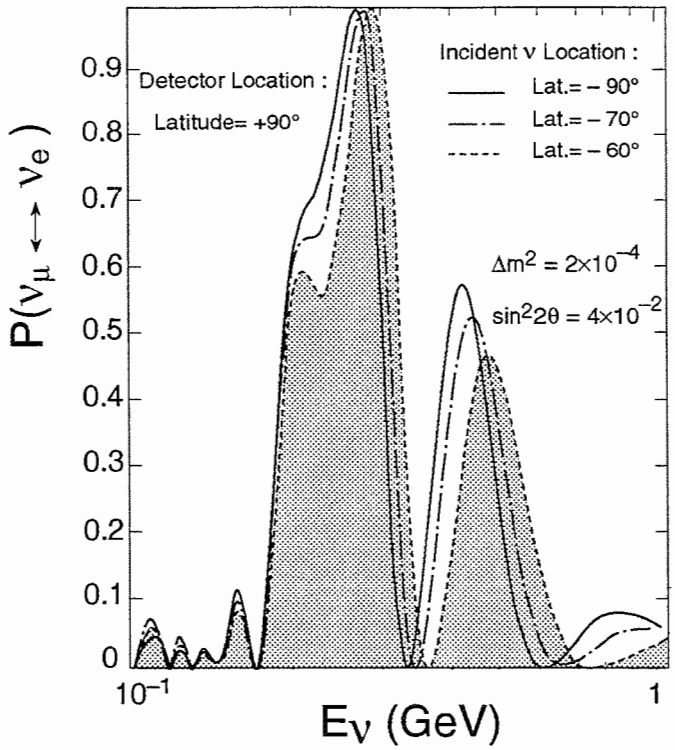

Figure 11 : Example of the MSW conversion pattern in the Earth for a given choice of neutrino masses and mixing angle. Large structures characteristic of the Earth's core and mantle are clearly visible.

Matter effects enhancing neutrino oscillations depend on the electron density of the traversed material. The electron density of the Earth (N_e) is not constant; it varies [15] from 1.6 mol/cm^3 near the surface up to 6.1 mol/cm^3 at the centre (Figure 10). The calculation of the transition probability for neutrinos at a given energy and angle was then performed, dividing the trajectory into segments where N_e is practically constant and calculating the probability at each step (we applied the method described in [16]).

One can see from Figure 9 that neutrino paths with $\psi > 148°$ cross the high density core of the Earth; the two clearly defined peaks in Figure 11 show neutrino resonant conversions taking place in the core and in the mantle. In Figure 12 the spatial dependence of transition probability is shown, for a given set of oscillation parameters and neutrino energy.

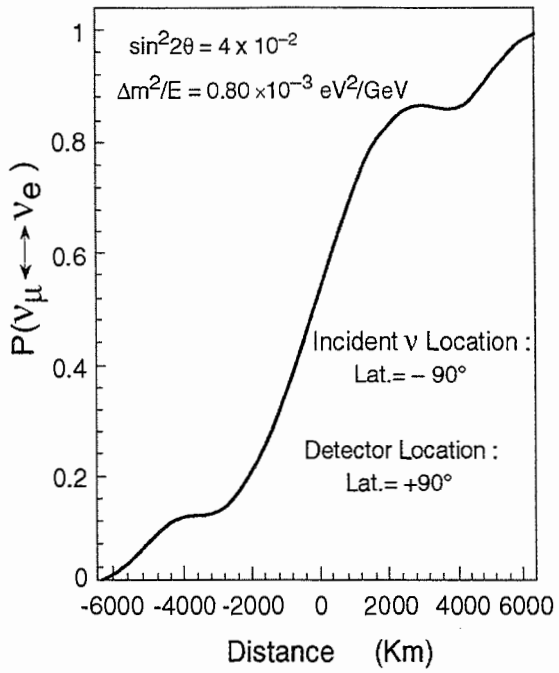

Figure 12 : Space dependence of $\nu_\mu \leftrightarrow \nu_e$ conversion probability as a function of the distance from the centre of the Earth. $\Delta m^2/E$ is chosen at the core resonance value and $\sin^2 2\theta$ where the core is approximately half a wavelength long.

In order to evaluate the sensitivity of ICARUS to oscillations from upward-going atmospheric neutrinos, we consider the double ratio R defined as:

$$R = \frac{\left(N_\mu/N_e\right)^{obs}}{\left(N_\mu/N_e\right)^{exp}}$$

where $\left(N_\mu/N_e\right)^{exp}$ is the ratio of the number of $(\nu_\mu + \bar{\nu}_\mu)$ and $(\nu_e + \bar{\nu}_e)$ charged current interactions expected in the case of no oscillations, integrating over both energy and zenith angle, while $\left(N_\mu/N_e\right)^{obs}$ refers to the same quantity, observable in the detector.

The quantity $\left(N_\mu/N_e\right)^{obs}$ depends on the transition probabilities for both neutrino and antineutrino. Since it is assumed that the neutrino masses are ordered in the natural way (namely, the lighter neutrino is primarily ν_e and the heavier is mostly ν_μ, a situation corresponding to $\Delta m^2 > 0$), matter effects can enhance oscillations in a resonant way in the neutrino sector but can only suppress slightly oscillations in the antineutrino sector, compared to the propagation in vacuum. Thus, $P(\bar{\nu}_e \leftrightarrow \bar{\nu}_\mu)$ is approximately equal to zero, there is no observable variation in the expected rate of the $\bar{\nu}_\mu$ and $\bar{\nu}_e$ events. Alternatively, in the neutrino sector, the transition probability $P(\nu_e \leftrightarrow \nu_\mu)$ varies with the oscillation parameters and the neutrino energy (Figure 11). Relying on the expected rates difference between ν_μ and ν_e (Figure 1), in practice a ν_μ deficit would be compensated by a ν_e excess, and the ratio R would become smaller than unity.

The accessible region, in the (Δm^2, $\sin^2 2\theta$) plane is limited by the error (σ_R) on the double ratio R. The main contributions to σ_R come from statistics, from theoretical uncertainties on fluxes and cross-sections and from

systematic errors related to the energy and angular resolution of the ICARUS detector.

Our estimation of the total error is $\sigma_R/R \approx 9\%$, where statistics contributes with $(\sigma_R/R)_{stat} \approx 8.5\%$, considering one year of exposure of the 5 kton ICARUS detector, and all the other sources of errors contribute to the systematic uncertainties, $(\sigma_R/R)_{syst} \approx 3.5\%$.

If we assume no oscillation, the shaded area in Figure 13 can be excluded at 90% C.L.

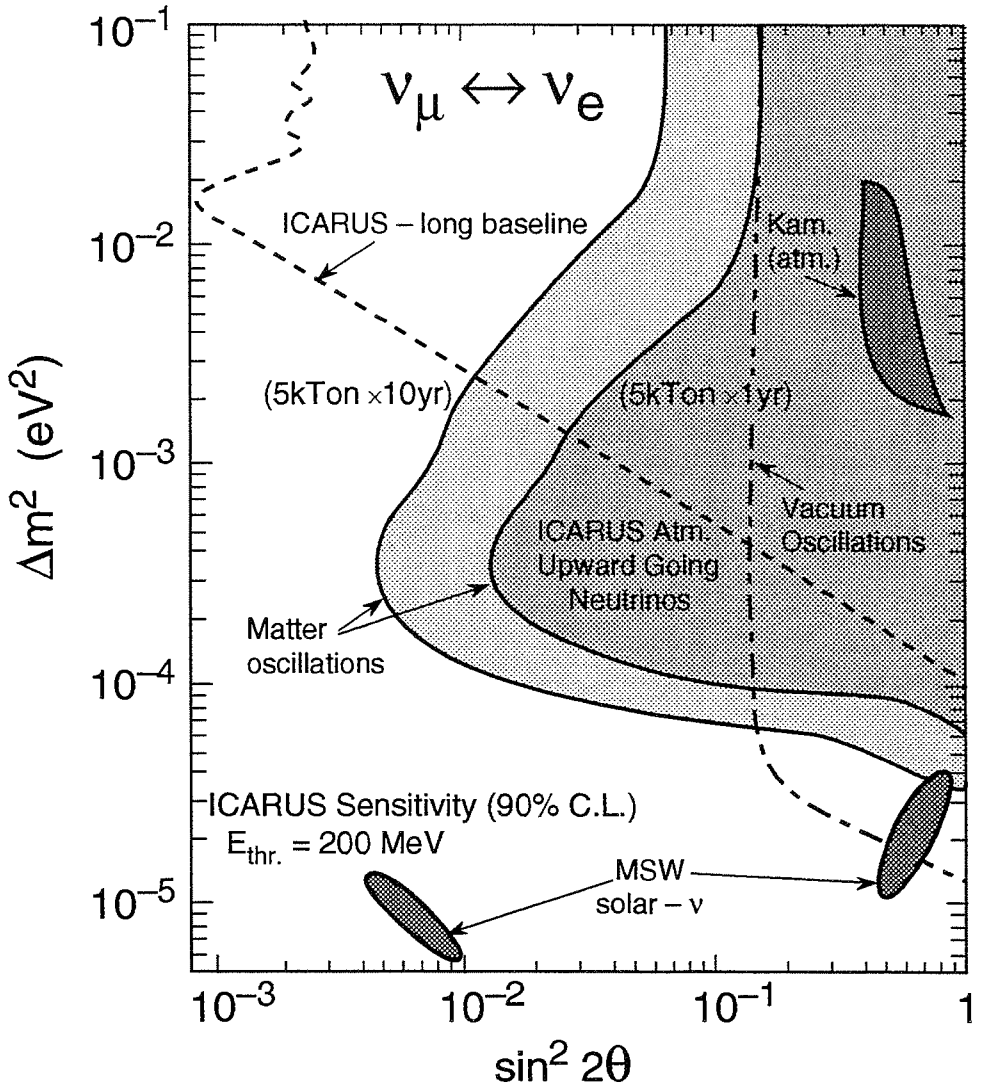

Figure 13 : Sensitivity of ICARUS to neutrino oscillations using atmospheric upward-going neutrinos. The vertical axis is Δm^2 and the horizontal axis is the usual mixing parameter. The shaded regions are excluded at 90% C.L. and correspond to 1 and 10 years of exposure of one 5 kton ICARUS module.

The conversion probability enhancement due to matter effects becomes evident when compared, in the parameter space, with vacuum oscillations for upward-going neutrinos through an empty Earth. In Figure 13 a contour plot in vacuum, obtained in the same conditions as the previous one but switching off the MSW effect, is also shown.

By increasing the time of exposure, the statistical error is reduced and larger regions can be excluded in the parameter space. In Figure 13 contour plots corresponding to 10 years of exposure of the 5 kton ICARUS detector are also reported. The statistical error at 10 years of exposure is comparable to the systematic error.

2.4.2 Reaching the sensitivity of the solar neutrino MSW solutions

The sensitivity study has been performed in terms of the double ratio R in order to reduce the systematic error coming mainly from the absolute neutrino flux uncertainty. Moreover, the ratio has been calculated integrating the event rate for neutrino energies ($E_\nu > 200$ MeV) well above the threshold where ν_μ charged-current reactions can take place, to ensure a full electron-to-muon separation in the event reconstruction.

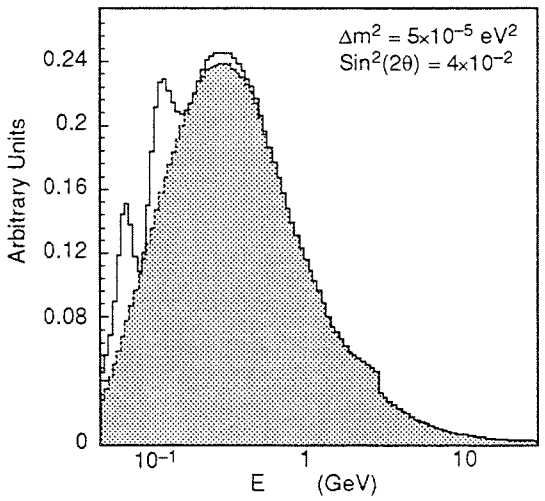

Figure 14a : Neutrino energy distribution from upwards going ν_e's and for the given choice of Δm^2 and $\sin^2(2\theta)$ indicated

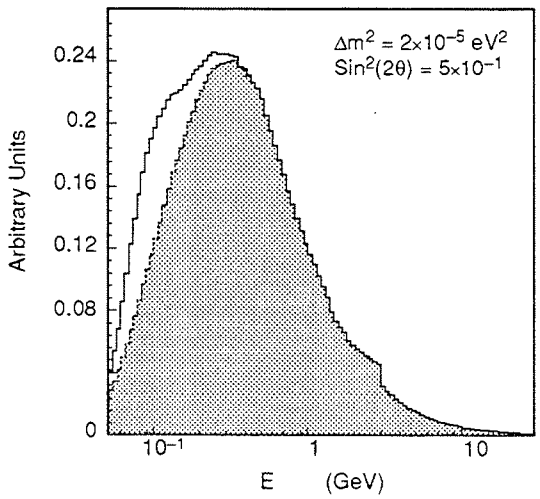

Figure 14b : Neutrino energy distribution from upwards going ν_e's and for the given choice of Δm^2 and $\sin^2(2\theta)$ indicated, corresponding to the large mixing MSW region, for solar neutrinos

Consequently, the corresponding fraction of the ν_e event sample (see Section 2.3.3) below 200 MeV and above the ν_e charged-current reaction threshold ($\approx$ 25 MeV), is not included in this analysis. In this energy range all the ν_μ's converting into ν_e's may produce a distortion in the energy distribution of the electron-neutrino interactions, depending on the values of the oscillation parameters, Figure 14a and 14b.

The comparison of the observed number of $(\nu_e + \bar{\nu}_e)$ events with the corresponding number of events expected in case of no oscillation (defining the ratio $Q \equiv [\nu_e + \bar{\nu}_e)^{obs}/(\nu_e + \bar{\nu}_e)^{exp}]$ provides another tool to study the ICARUS sensitivity to oscillations. In particular, from the resonance condition we expect that exploiting these low-energy data samples, a region at smaller Δm^2 becomes explorable.

However, this method is severely limited both by statistics and by the systematic error reflecting the large uncertainty on the present ν_e flux calculation at low energy.

Several experiments, using mainly high-altitude arrays or balloon techniques, are going to provide data on cosmic-muon production at different altitudes in the atmosphere. Using these future data, a significant reduction in the absolute neutrino flux uncertainty should be possible. This result should allow a safer use of the low-energy ν_e reaction data sample to extend the experimental sensitivity to oscillations.

Taking as an assumption that the systematic error on the ratio Q is $(\sigma_Q/Q)_{syst} = 10\%$, and using the statistical error as $(\sigma_Q/Q)_{stat} = 10\%$, for one year of exposure of the 5 kton ICARUS detector (integrating on the energy range from 30 to 200 MeV), we can exclude, at 90% C.L., the region labelled Q in Figure 15. In 10 years of exposure, the total error will be dominated by the systematic error. Combining the region excluded by this method (ratio Q), with the one from the statistically independent method of Section 2.4.1 (ratio R), one can obtain the overall contours labelled $Q \cup R$, for 1 and 10 years of exposure, at 90% C.L., also shown in Figure 15.

This method allows, in principle, a substantial extension of the sensitivity region down to the very low Δm^2 values of the solar neutrino MSW regions. However, one should stress again that this result is based on the assumptions made on the possible reduction of the ν_e absolute flux uncertainty.

The other crucial piece of information is the discrimination between neutrinos and antineutrinos. We know that the MSW effect can occur only for neutrinos or antineutrinos but not for both. Since we suspect that the effect occurs in the sun where neutrinos are produced, we can assume that it is happening for neutrinos but not for antineutrinos. Therefore, by not distinguishing between neutrinos and antineutrinos, the effect is diluted. The distinction between neutrinos and antineutrinos can be obtained from the knowledge of the charge of the lepton produced in the charged-current reactions. Since ICARUS is not equipped with a magnetic field we have to rely on other means to determine the charge.

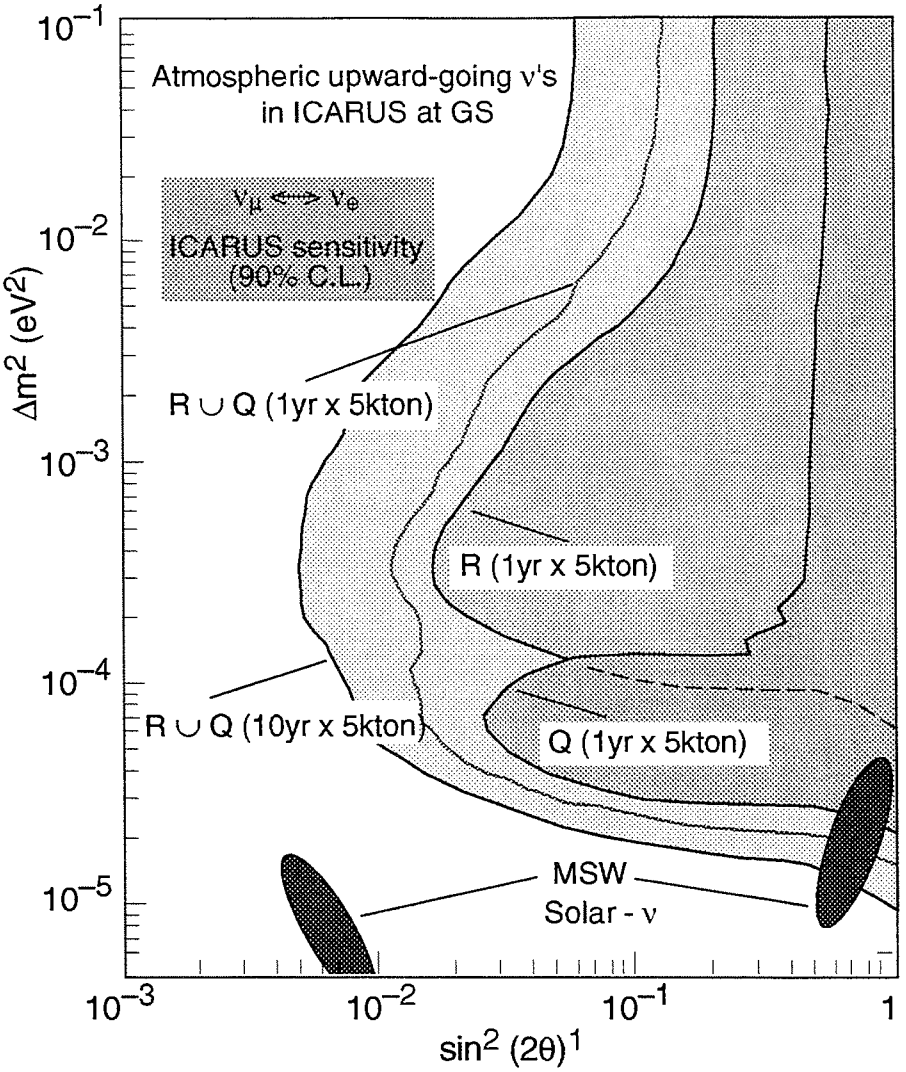

Figure 15 : ICARUS sensitivity to ($\nu_\mu \leftrightarrow \nu_e$) oscillations (90% CL): the region indicated by Q(1 yr × 5 kton) is obtained with the low-energy electron-neutrino sample (Q ratio, Section 2.4.2); the region indicated by R(1 yr × 5 kton) is obtained with the ν_μ to ν_e ratio at higher E_ν energies (R ratio, Sec. 2.4.1, Figure 13); the region indicated by $R \cup Q$(1 yr × 5 kton) is the combination of the above R and Q regions. All three regions correspond to an exposure of one year of the (5 kton) ICARUS detector. The region, indicated by $R \cup Q$(10 yr × 5 kton), is obtained in a similar way as $R \cup Q$(1 yr × 5 kton) but for a 10-year exposure.

Most muons from atmospheric neutrinos stop in the detector and then decay into electrons or are captured by an argon nucleus. All the captures are μ^-'s and the capture probability is ≈ 73% (the measurement is reported in Chapter V). Since muons from atmospheric neutrino interactions are a mixture of both types of muons, with a given ratio of positive to negative charge (see Table 2), by observing whether they decay or are captured, we can partially distinguish if it is a μ^+ or a μ^-.

The knowledge of the charge of the muons observed in ICARUS opens a new window in our study of atmospheric neutrinos. The ratio of neutrinos to antineutrinos can, in principle, be more precisely predicted than

the ratio of ν_e's to ν_μ's, hence a better sensitivity can be obtained, resulting in a further extension towards the solar neutrino MSW regions.

Atmospheric neutrinos in ICARUS offer a separate experiment in which the solar neutrino puzzle will also be addressed, adding therefore precious redundancy in the experimental data on the subject.

2.4.3 Downward-going neutrinos

The study of downward-going atmospheric neutrinos will usefully complement the study of upward-going neutrinos, in particular by providing a large reference sample of events not affected by MSW effects. The rate of events expected (Table 2) is about 15% larger than for upward-going neutrinos. The conversion probability strongly depends on the neutrino production altitude in the atmosphere. We use the altitude distribution from [17]. Further studies are under way.

2.5 References

[1] K.S. Hirata et al., Phys. Lett. **B280** (1992) 146–52.

[2] D. Casper et al., Phys. Rev. Lett. **66** (1991) 2561.

[3] Ch. Berger et al., Phys. Lett. **B227** (1989) 489; Phys. Lett. **B245** (1990) 305.

[4] M. Aglietta et al., Europhys. Lett. **8** (1989) 611.

[5] M. Goodman, Contained ν Events Observed in Soudan 2, presented at the XXIII International Cosmic Ray Conference, Calgary, July 1993.

[6] M.M. Boliev et al., Proc. Third International Workshop on Neutrino Telescopes, ed. M. Baldo-Ceolin, p. 235 (1991).

[7] R. Becker-Szendy et al., Phys. Rev. Lett. **69** (1991) 1010.

[8] L. Wolfenstein, Phys. Rev. **D17** (1978) 2369; S.P. Mikheyev and A.Y. Smirnov, Sov. J. Nucl. Phys. **42** (1985) 913; H.A. Bethe, Phys. Lett. **B175** (1986) 478; P. Rosen and J.M. Gelb, Phys. Rev. **D34** (1986) 969.

[9] G. Barr, T. Gaisser and T. Stanev, Phys. Rev. **D39** (1989) 3532; T. Gaisser, T. Stanev and G. Barr, Phys. Rev. **D38** (1988) 85; T. Gaisser and T. Stanev, Phys. Rev. Lett. **51** (1983) 223.

[10] T. Stanev, private communication (1992).

[11] L. V. Volkova, Sov. J. Nucl. Phys. **31** (1980) 784.

[12] T. Gaisser and J.S. O'Connel, Phys. Rev. **D34** (1986) 822; E. Nikolov et al., Phys. Lett. **B281** (1992) 208; T. Gaisser, M. Novakowski and E. Paschos, Phys. Rev. **D33** (1986) 1233.

[13] GENEVE Monte Carlo, write-up in preparation.

[14] T.K. Kuo and J. Pantaleone, Phys. Rev. Lett. **57** (1986) 1805.

[15] F. D. Stacey, Physics of the Earth, (Wiley, New York, 1969).

[16] A. Dar et al., Phys. Rev. **D35** (1987) 3607.

[17] T. Gaisser, T. Stanev and F. Cavanna, Altitude distribution of atmospheric neutrinos, in preparation.

3. Long-baseline neutrino oscillations

3.1 Introduction

The high-flux neutrino beams which CERN can provide make it possible to perform a long-baseline neutrino oscillation search with baseline distances as far as, for instance, the distance between CERN and Superkamiokande in Japan [1]. Artificial neutrino beams, such as those available at CERN, are essentially pure sources of ν_μ's, and the search for neutrino oscillations consists in detecting ν_e's and ν_τ's, produced by oscillations of ν_μ's.

The probability of oscillation between ν_μ and ν_e, for a given neutrino energy (E) and a given flight path (L) may be written as:

$$P(\nu_\mu \leftrightarrow \nu_e) = \sin^2(2\theta_{\mu e}) \times \sin^2(1.27 \times \Delta m^2_{\mu e} \times L/E)$$

where $\theta_{\mu e}$ is the mixing angle between ν_μ and ν_e and $\Delta m^2_{\mu e} \equiv m_{\nu\mu}{}^2 - m_{\nu e}{}^2$. If one takes into account that the neutrino flux at great distances decreases as L^{-2} and that the event rate is proportional to the neutrino energy, the precision which can be reached in a search intended for the smallest possible $\Delta m^2_{\mu e}$ values, is independent of the distance L:

$$\Delta p/p \propto E/[T \times \sin^2(2\theta) \times (\Delta m^2_{\mu e})^2]$$

where T is the time during which the experiment is running. Hence, on the one hand, the lowest possible energy is preferable. It is also the case if one wants to have the best rejection against some of the backgrounds, for ICARUS mainly π^0's faking electrons. On the other hand, for the ν_τ search, in order to produce real τ's through charged-current reactions, the beam energy must be such that neutrinos are produced above the kinematical threshold of about 10 GeV. This is the reason why a SPS beam is best-suited in the case of ICARUS to provide protons of energies ranging from about 80 GeV to 450 GeV.

In order to optimize for the sensitivity to small values of $\sin^2(2\theta)$ at larger values of $\Delta m^2_{\mu e}$, in a regime of small oscillation lengths and with a fluctuating neutrino energy as is the case in an accelerator beam, the factor $\sin^2(1.27 \times \Delta m^2_{\mu e} \times L/E)$ averages to 1/2. Then, for a given neutrino beam configuration, the sensitivity to small $\sin^2(2\theta)$ values is given by $\Delta p/p = L^2/[E \times \sin^2(2\theta)]$. Consequently, the sensitivity of an ICARUS detector at a distance of 732 km from Gran Sasso is about two orders of magnitude better than, for instance, the sensitivity of the same detector installed 9000 km away.

Another important consideration in the choice of a detector target for a long-baseline study is the aiming of the neutrino beam. It turns out that there is no great technical difficulty but the practical limitation will be cost. In the case of a CERN SPS beam to Gran Sasso the situation is extraordinarily favourable; a proton transfer line between SPS and LEP tunnels has exactly the right configuration to allow proton extraction in the direction of Gran Sasso (Figure 1). In addition, the 1 km long decay tunnel needed can be excavated at the same time as the planned transfer tunnel at a very modest additional cost.

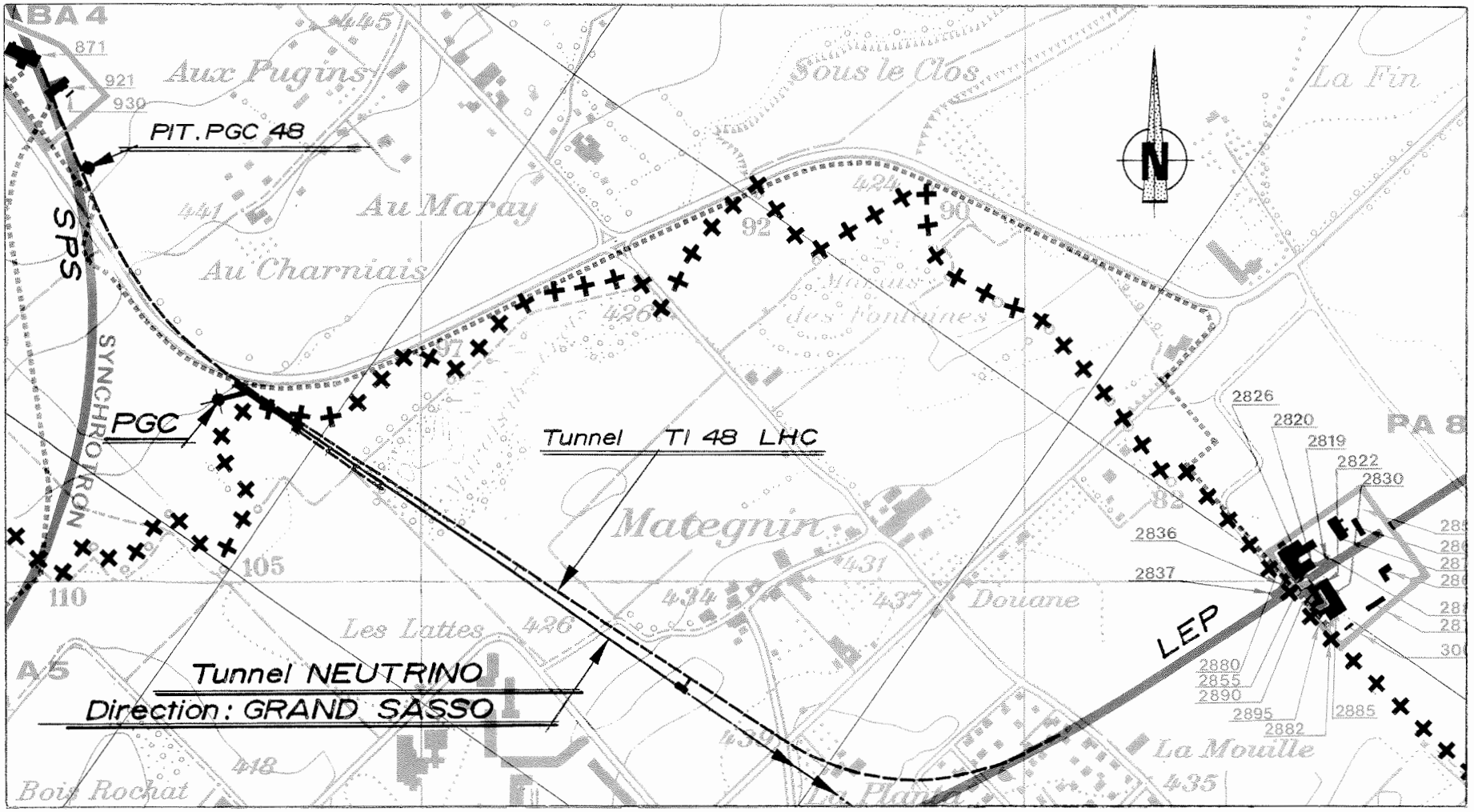

Figure 1 : Map of CERN showing the LHC proton transfer line between the SPS and LEP tunnels as well as the layout of the neutrino tunnel in the direction of Gran Sasso.

In addition, the few surface constructions needed can all be located on French territory which has the advantage of dealing with only one authority as far as building authorisations are concerned. Finally, the small slope required to aim the beam at Gran Sasso allows the whole decay tunnel to be dug out of a molasse terrain, which is ideal for this type of work. Great experience has been acquired by CERN in excavating the 27 km LEP tunnel with similar techniques. We have here such an exceptional situation, that it is evident that the CERN neutrino beam to Gran Sasso should be constructed at the same time as the proton transfer line needed for LHC.

There is increasing evidence (atmospheric neutrino studies) that a specific neutrino mass region at small Δm^2 (10^{-1} to 10^{-5} eV^2) should be carefully studied both in the $\nu_\mu \leftrightarrow \nu_e$ and $\nu_\mu \leftrightarrow \nu_\tau$ channels. This can best be done by extending the experiment baseline outside the limits of the laboratory. Not only is it technically straightforward to send a CERN ν_μ beam to Gran Sasso, but ICARUS, which is primarily designed for the search for proton decay, represents an ideal natural target for such a neutrino beam. It has a large mass and is placed underground in a low-background environment; and, most importantly, it has the excellent detection capability required to identify possibly rare ν_e charged-current interactions in a background of neutral current ν_μ events. As we shall see, even though physics with a neutrino beam is not the primary goal of ICARUS, it adds a considerable scientific potential to the programme:

– the search for $\nu_\mu \leftrightarrow \nu_e$ and $\nu_\mu \leftrightarrow \nu_\tau$ oscillations;
– the search for MSW matter effects;
– the use of the beam to calibrate the background to proton decay.

Artificially-generated neutrinos or antineutrinos (from accelerator beams) indeed offer several clear advantages over other possible sources of neutrinos:

– the neutrino energy spectrum is more sharply peaked and better known than for atmospheric neutrinos, and it can be tuned;

– one can switch between neutrinos and antineutrinos. Antineutrinos are currently poorly studied and, in addition, they are expected to behave differently from neutrinos in their interaction with matter, this is a crucial feature for a definite study of MSW matter effects;

– the known direction and timing of the beam spills allow efficient event identification, so that running with the neutrino beam does not perturb data-taking for proton decay and other neutrino studies;

– the initial beam flavour composition is well known (almost entirely ν_μ or $\bar{\nu}_\mu$) and at the same time the high rate allows a good statistical accuracy.

We can conclude that the availability of a neutrino beam from CERN to the Gran Sasso underground laboratory, in conjunction with the new detector technique offered by ICARUS, will allow the breaking of new ground in the study of the nature of neutrinos and of their interaction with matter.

3.2 The CERN neutrino beam to Gran Sasso

3.2.1 The target

Figure 2 shows the general layout of the neutrino beam elements needed to extract protons from the CERN SPS and to direct and focus the charged hadrons producing neutrinos towards the Gran Sasso Laboratory. It is foreseen to use the same type of target as currently under construction for the experiments WA95 and WA96 (CHORUS and NOMAD), which is very similar to the one used previously for experiment WA79 (Charm II). It consists of a string of beryllium rods of 100 mm length each and a diameter of 3 mm. Each rod is inserted at either end into the holes of a beryllium plate. Cooling is provided by a forced flow of gas.

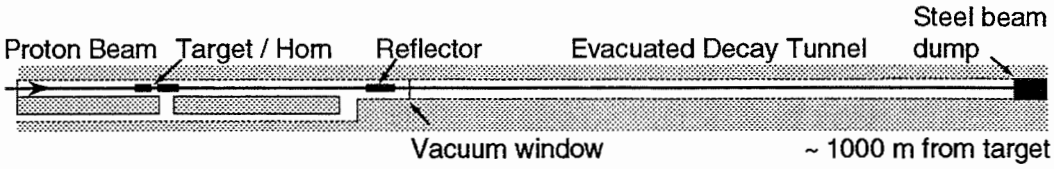

Figure 2 : General layout of the CERN neutrino beam line for Gran Sasso

The target is mounted in a container which will be put in place by a precision plug-in technique. Compared to targets of different geometry and materials this type of target provides optimum efficiency, i.e. highest flux of neutrinos per primary proton. A target of this type has been exposed for long periods with a double fast/slow extracted beam of spill length of 6 ms and a total intensity of 1.8×10^{13} protons per SPS cycle. Experience of this type of target with a fast extracted beam of 23 μs spill length exists also from its use for producing the narrow-band neutrino beam in 1979. We conclude that we can safely assume a maximum intensity of 1×10^{13} protons per pulse at the highest SPS energy. We need to study whether a somewhat different geometry, e.g. by reducing the length of the rods, could somewhat increase the performance.

3.2.2 The neutrino target station

There are several ways in which target areas have been designed for protons of several hundred GeV in order to minimize the effects of the high levels of induced radioactivity. In the North target areas of the SPS the approach has been to build as large a target hall as was economically feasible in order to dilute the secondary particle fluxes by the simple inverse square law, as much as possible, before they hit the target station walls, thus reducing the interaction density in these walls and thus the levels of induced radioactivity. Local shields are placed around the principal points where protons interact, both to reduce the levels of induced radioactivity in the surrounding components such as motors for positioning the targets, etc. and to reduce as much as possible the total hadron path-length in the air thus reducing the activity levels in the air. The large amount of space allows one to insert inactive shielding between a person working and the active components.

The approach used at FERMILAB was to minimize the volume of the target-station and to counter the effect of the extremely high levels of induced

radioactivity by avoiding the need for human intervention directly on the equipment of the target station. All equipment is mounted on 'trains' which can be removed from the target station to specially shielded areas serviced with manipulators in order to maintain and repair the active equipment.

The approach considered here, for the new neutrino target area, is to follow that of the FERMILAB target stations, i.e. to mount the target, some local shielding and all beam monitoring equipment on one carriage, the horn on a second carriage, and the reflector on a third. The three carriages would be connected by flexible attachments and would move on rails set into the ground. Alignment would be achieved by special jacks slotted into special reference marks in the walls and floor of the cave. This should present little difficulty for the 6 degree slope [2] of the target station to Gran Sasso.

The proposed concept involves filling in the excavated tunnel with iron and concrete, leaving only enough room for the trains to pass through. This shielding is designed to attenuate the secondary radiation so that as little radioactivity as possible is created in the rock around the target region. No services other than the rails and location points would be installed in the tunnel. This implies that all services must be brought to the neutrino cave via a parallel service tunnel of similar dimensions to the target tunnel placed some 8 metres to the side and linked by small cross-galleries. These galleries and alcoves would contain the transformers for the horn and reflector. The galleries would be positioned so that services could be connected to the carriages from the safety of the service gallery.

3.2.3 The focusing elements

Three possibilities can be considered for focusing the beam after the target :

- quadrupole focusing using one or more triplet structures,
- co-axial magnetic lenses usually known as horns and reflectors,
- plasma lenses in which the target forms the inner conductor.

The horn/reflector alternative (Figure 3) is preferred as it provides a broader energy and angular acceptance – hence higher neutrino flux, is sign selective (it allows a simple switching mechanism between neutrinos and antineutrinos), and is known to operate with high reliability.

An essential feature of this type of beam is that there can be no correction of the beam direction after the target. All elements must be coaxial with a line between the target and detector to a high degree of precision and the incident proton beam must be steered coaxially through the target. This imposes stringent requirements on the alignment of the elements and rail system.

For 450 GeV/c incident protons, the magnetic horn would typically be of the order of 6 m length and located 2 m behind the target, manufactured from anticorodal, with a cylindrical outer conductor of 250 mm radius and a thin 'paraboloid' inner conductor with radius from 180 mm to 8 mm. The inner conductor would be cooled by de-ionized water spray on a closed-circuit system. The horn would be powered with a half-sinusoid pulse of 100–120 kA peak current and 3 ms duration obtained by discharge of a capacitor bank through a pulsed current transformer.

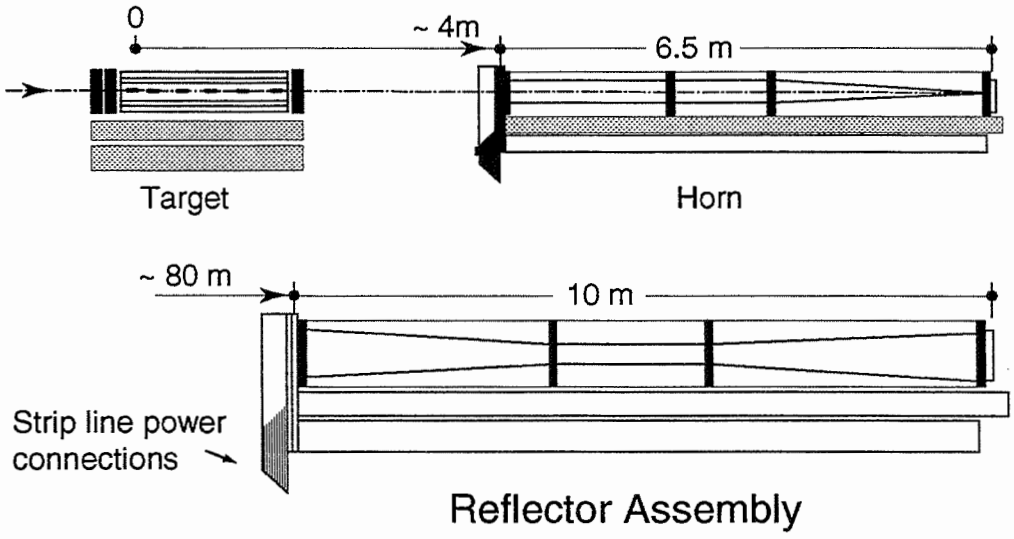

Figure 3 : Details of the target, horn and reflector assembly envisaged for the CERN neutrino beam to Gran Sasso

A single magnetic reflector whose principle is sketched in Figure 4, of similar design to the horn, is envisaged. The potential gain in flux by adding further reflectors is usually negated by the increased absorption losses. The reflector length would ideally be ~ 10 m, with an outer conductor of 400 mm radius; final dimensions would be conditioned by the size of the access shaft to the cavern.

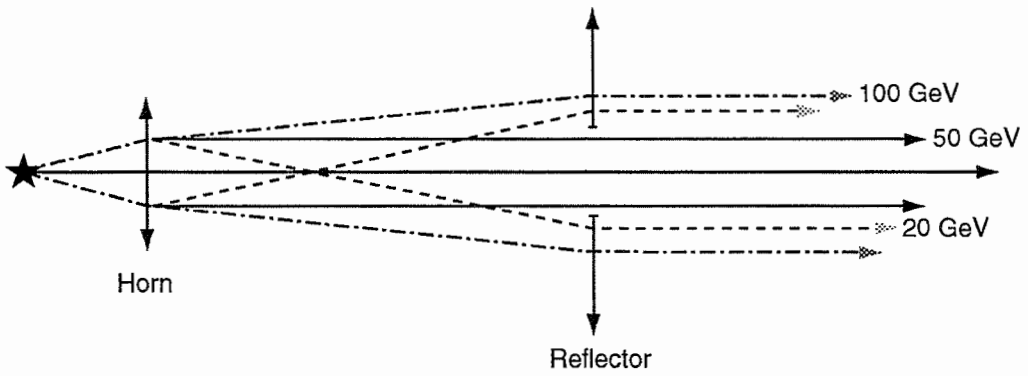

Figure 4 : Principle of the magnetic reflector envisaged for the CERN neutrino beam to Gran Sasso

The transformers would be located in the alcoves of the connecting galleries between the beam and service tunnels. The water and high-current strip-line connections at the junction of the beam tunnel and gallery must be designed so as to limit personnel radiation exposure, and some form of remote handling equipment may be necessary.

Some very preliminary calculations, extrapolating the CHORUS/NOMAD neutrino polarity beam, indicate an r.m.s. neutrino beam radius of the order of 600 m for Gran Sasso at 730 km and neutrino flux of $6 \times 10^4/m^2$ per 10^{13} incident protons in a 10 m radius detector with a mean energy of 40 GeV. The latter should be compared to a typical mean energy of 24 GeV in current beams in the West area, showing that the beam becomes considerably harder with distance. The ratio of $\bar{\nu}_\mu/\nu_\mu$ is expected to be less than 2% and the ratio of ν_e/ν_μ is in the region of 0.5%.

For 80 GeV/c incident protons the magnetic horn would be shorter (~ 2.5 m) and as close as possible to the rear of the target.

Since the beginning of SPS operation in 1976, neutrino beams of this type have been operated on a continuous basis for over 50% of the scheduled machine run time and taken 65% of all protons accelerated by the SPS.

3.2.4 Beam lines and tunnels

As part of the work for the LHC project at CERN, injection transfer lines are being designed to bring the fast extracted beams from the SPS to the new collider [3]. The primary proton beam for a neutrino production target to feed Gran Sasso with only minor modifications can be derived from TI48, which links SPS/LSS4 to LHC/P8 (Figure 5).

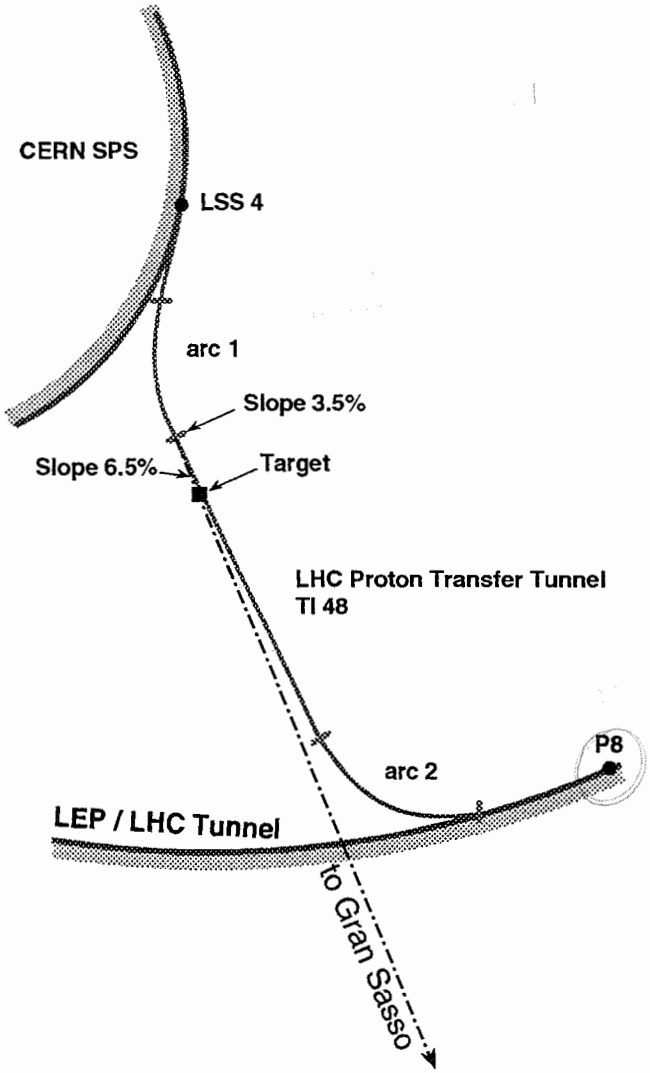

Figure 5 : Geometric characteristics of the CERN neutrino beam to Gran Sasso. The TI48 tunnel is needed to transfer protons from the SPS to the LHC.

The geometry of TI48 is formed by two arcs of 35° and 70° total horizontal deflection separated by a 1-km long straight section. The orientation of this straight section is such that only very minor extra horizontal and vertical deflections are needed to direct the protons exactly

towards the Gran Sasso detector. The required horizontal deflection is of the order of 31 mrad, just sufficient for switching away from TI48 and for obtaining sufficient lateral separation at the position of the target station from the LHC injection line. The vertical deflection is about 32.5 mrad downwards. The total length of the new beam line to implement these deflections and also to provide the necessary focusing of the small beam spot onto the target is about 140 m. Whereas the arcs of TI48 are made of superconducting magnets, for the branch towards the neutrino target classical warm magnets of types existing at CERN can be used. The total required bending power for 450 GeV/c beam momentum is 95 T × m and the number of quadrupoles is 10 equivalent type QTL. The beam line will be equipped with horizontally and vertically deflecting pairs of dipole correctors for precise final adjustment of the beam direction and with an adequate number of beam-position, profile and intensity monitors.

An overall plan of the proposed modification to TI48 is given in Figure 1. Access to the new tunnels would be via a 9 m diameter vertical shaft, linking via a horizontal tunnel to a 10 m wide junction chamber. This would provide the necessary manoeuvring and storage area for the highly radioactive train carriages. It is assumed that a separate short service tunnel will be built alongside the target station. An alternative would be to use the TI48 tunnel itself as the service tunnel. However, because of the presence of the LHC injection line and the level and slope difference between TI48 and the neutrino target tunnel, this latter may not be a practical proposition. This remains to be studied in detail.

3.2.5 Decay tunnel

Following on from the target tunnel the evacuated pion-decay tunnel is assumed to extend for about 1000 m. At the end of the decay tunnel one must expect to build a dump for the remaining primary protons and secondary hadrons that will contain induced radioactivity to a level acceptable to the regulatory authorities. This dump cavern is close enough to TI48, however, for access to be provided via the LHC injection tunnel.

In the initial calculations, an evacuated decay tunnel of 1.1 m radius and total decay length from the target of 1000 m has been assumed. It seems probable that a smaller radius would be adequate if this reduces the civil engineering costs. Increasing the length of the decay path from the target increases the neutrino flux, but it also favours the high-energy component.

3.2.6 Beam considerations

The normal SPS cycle, which provides beams for both SPS and LEP experiments, has a period of 14.4 s. Thus, in an operating year of 10^7 s there would be 7×10^5 pulses which with 10^{13} protons per pulse would provide 7×10^{18} protons per year onto the neutrino production target.

The simplest modification to the normal SPS cycle would be the removal of the lepton pulses which feed LEP, resulting in a time-saving of 4.8 s. With this cycle, which has a period of 9.6 s, the SPS could supply 10^{19} protons of energy 450 GeV per year to the neutrino target.

With the appropriate machine development, one could envisage shortening this cycle to 4.8 s which would mean that 2×10^{19} protons could be

supplied to the neutrino target for a proton energy of 450 GeV. In this case, the operation of the SPS would have to be dedicated to this experiment.

3.3 The search for neutrino oscillations with the CERN neutrino beam

3.3.1 $\nu_\mu \leftrightarrow \nu_e$ oscillations

The principle of the experiment is simple, it consists of searching for charged-current reactions from ν_e's produced in the beam by oscillation from ν_μ's. The signature is therefore an electron producing an electromagnetic shower in the liquid argon. Using the characteristics of the CERN neutrino beam [4], the rate of events and the sensitivity of ICARUS in $\Delta m^2_{\mu e}$ and $\sin^2(2\theta_{\mu e})$ have been calculated (Table 1) for one ICARUS module and for one year of data taking. Based on statistical analysis only (neglecting possible π^0 backgrounds) the optimal sensitivity for $\Delta m^2_{\mu e}$ and $\sin^2(2\theta_{\mu e})$ combined is obtained for proton energies between 80 and 160 GeV. The calculation assumes a decay tunnel length of 1000 m, 1.5×10^{13} (3×10^{13}) protons on targets every 7.2 s (2.4 s) at a proton energy of 400 GeV (40 GeV). For other energies a linear interpolation was used.

Table 1: Sensitivity in Δm^2 and $\sin^2(2\theta)$ for $\nu_\mu \leftrightarrow \nu_e$ oscillations as a function of the energy of the proton on target. E_p, E_π and E_ν are respectively the proton, pion and neutrino energies. Δm^2 is expressed in eV^2. $N(\nu_e)$ is the number of background ν_e's in the beam. The limits are given with and without taking into account the beam ν_e background.

E_P	$<E_\pi>$	$<E_\nu^{-2}>^{-1/2}$	$N(\nu_\mu)$	$N(\nu_e)$	Δm^2 (no BG)	Δm^2 (ν_e BG)	$\sin^2(2\theta)$ (no BG)	$\sin^2(2\theta)$ (ν_e BG)
40	12.6	3.5	1250	0.24	$1.6\,10^{-4}$	$1.6\,10^{-4}$	$3.6\,10^{-3}$	$3.6\,10^{-3}$
80	25.7	5.9	4000	1.0	$1.5\,10^{-4}$	$1.6\,10^{-4}$	$1.2\,10^{-3}$	$1.3\,10^{-3}$
160	48.9	9.0	10800	5.4	$1.4\,10^{-4}$	$2.2\,10^{-4}$	$4.3\,10^{-4}$	$1.0\,10^{-3}$
240	72.7	12.0	19800	17.6	$1.4\,10^{-4}$	$2.9\,10^{-4}$	$2.3\,10^{-4}$	$9.6\,10^{-4}$
320	95.4	14.8	29800	32.3	$1.4\,10^{-4}$	$3.3\,10^{-4}$	$1.6\,10^{-4}$	$8.5\,10^{-4}$
400	120	17.8	41500	53.4	$1.4\,10^{-4}$	$4.0\,10^{-4}$	$1.1\,10^{-4}$	$8.2\,10^{-4}$
450	134.5	19.2	47700	72.3	$1.4\,10^{-4}$	$4.3\,10^{-4}$	$9.0\,10^{-5}$	$8.0\,10^{-4}$

There are two types of background to charged-current interactions from genuine ν_e coming from a ν_μ oscillation:

(i) ν_e's present in the initial beam producing genuine electrons: they mostly come from K decays. Because their transverse momentum is larger than ν_μ produced in π decays, as the distance increases, so their proportion decreases (Table 1), and at Gran Sasso they are almost negligible for 80 GeV protons. (The fraction in the beam is estimated to be 2.5×10^{-4}.)

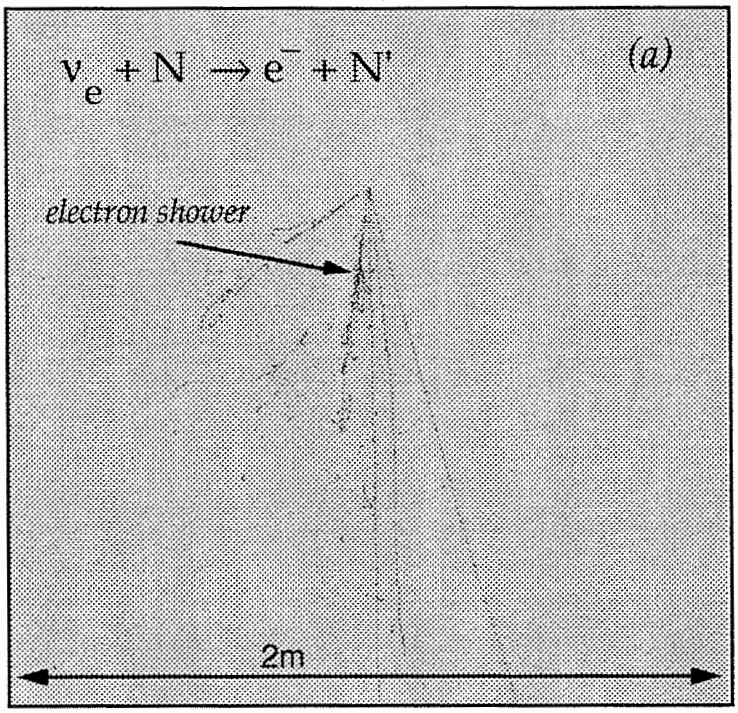

Figure 6 : Simulated ν_e charged-current event in the liquid argon. The electron shower is spectacular and easy to recognize.

(ii) The other important type of background comes from neutral current interactions of ν_μ producing a recoiling jet with π^0's faking electrons. We expect of the order of 1.5 π^0's to beproduced in each hadronic shower. In ICARUS, π^0's can be identified from their decay properties (separation of the photon showers), from the shape of the shower, and from ionization information. Figures 6, 7 and 8 show three characteristic types of events: (a) ν_e charged-current interaction producing an electron shower and corresponding to the signal being sought; (b) ν_μ neutral-current interaction without a high-energy π^0; (c) ν_μ neutral-current event with an energetic π^0 decaying into two well-separated showers. Both b and c are examples of background; however, only type c is worth discussing in some detail. One may note that the topologies of the three types of events are very different. The strength of ICARUS comes from the ability of being able to distinguish between genuine electrons and π^0's. This was confirmed by a detailed Monte Carlo simulation which has shown that the π^0 background can also be made almost negligible in the 80 GeV proton case. (The remaining fraction in the data is estimated to be smaller than 0.1%.) The event generator used was the Lund Monte Carlo. Confidence in the simulation was obtained from a comparison between the π^0 momentum spectrum produced by the Monte Carlo and data from the Serpukhov bubble chamber SKAT [5] at a similar energy. Figure 9 shows that the agreement is very good.

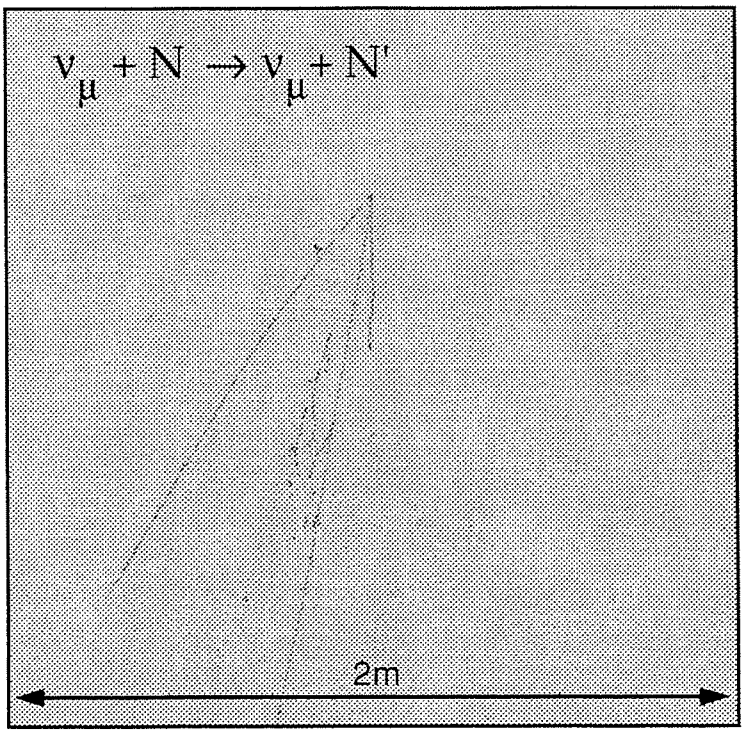

Figure 7 : Simulated ν_μ neutral-current interaction in liquid argon.

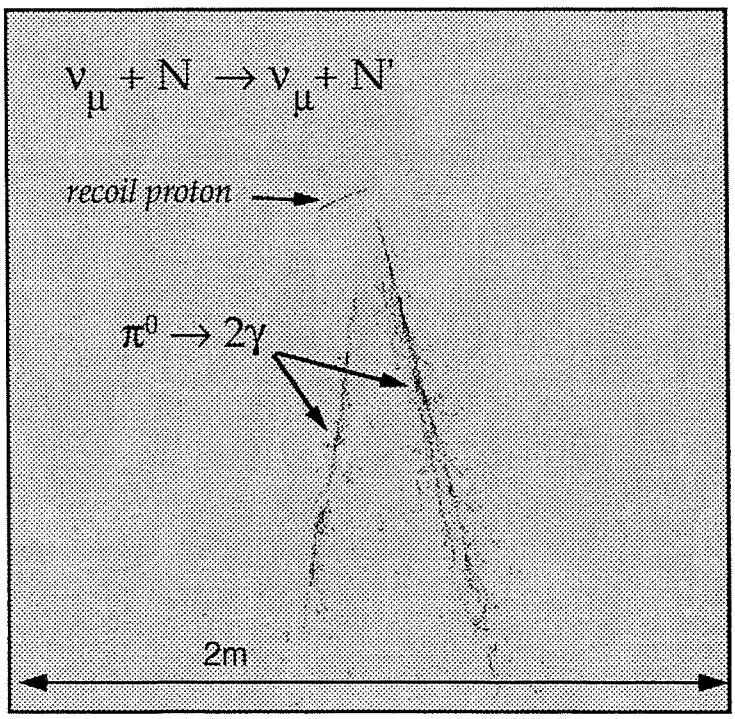

Figure 8 : Neutral-current ν_μ interaction producing an energetic π^0. The two separated photon showers are clearly visible.

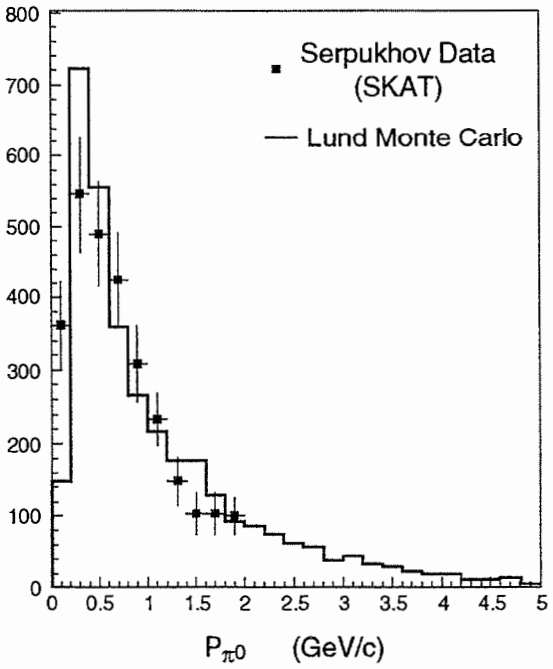

Figure 9 : Comparison of momentum spectra of π^0's produced by the Lund Monte Carlo generator and data from the SKAT bubble chamber at Serpukhov

The events generated were digitized according to the ICARUS readout configuration with a wire pitch of 5 mm. The properties of electron and π^0 showers were studied. The discrimination is obtained first of all from the ionization information (Figure 10). Showers produced by π^0's tend to have more ionization deposition than electron showers because their shower is initiated by two photons. A 2 mips (minimum-ionizing particle signal) cut removes 80% of the π^0's but retains 95% of the electrons.

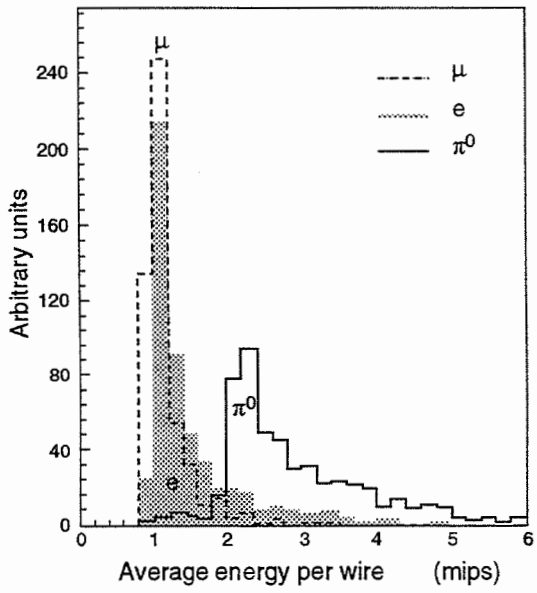

Figure 10 : Comparison of ionization deposition on the first 10 wires between a muon, an electron, and a π^0

The next means we have to discriminate between electrons and π^0 showers is to study the development of the shower. For electrons the shower starts at the vertex, for π^0's the shower tends to start later. The result of our simulation (Figure 11) shows that 92% of the π^0 showers start at least 1.5 cm away from the vertex.

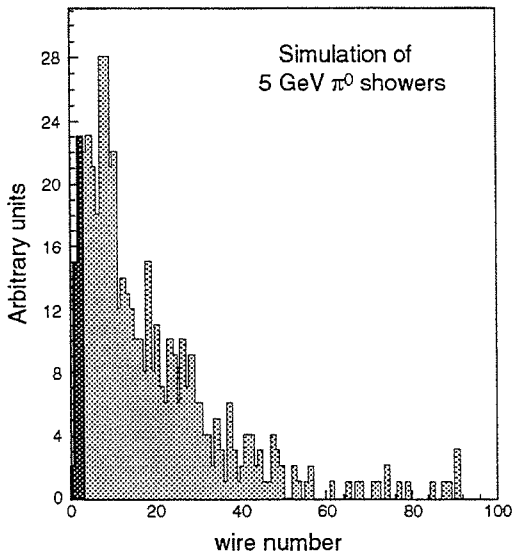

Figure 11 : Longitudinal profile of π^0 showers, given as a function of wire numbered from the vertex. The wire pitch is 5 mm.

Finally, since low-energy π^0's decay into two well-separated showers, at low energy, below about 1 GeV, they can be recognized simply from the topology of the event. In the absence of an automatic pattern-recognition program we have scanned events visually to verify that the topological properties of π^0 events (Figure 12) were well understood. The scan not only confirmed that all π^0's with momentum up to 1 GeV can be recognized, but also that a significant fraction can also be recognized this way at higher momenta.

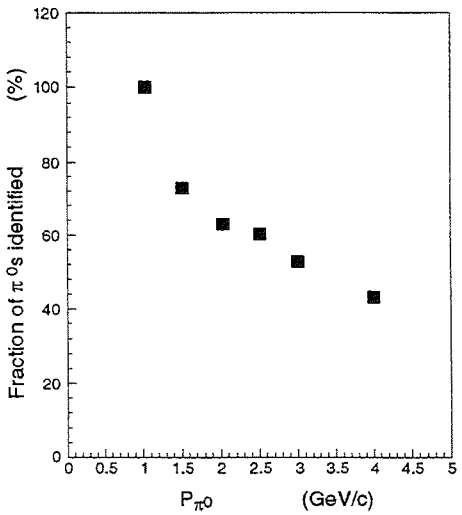

Figure 12 : Fraction of π^0's identified in a visual scan from the topology of their decay, as a function of momentum

Taking ν_e contamination level in the neutrino beam into account, as well as the remaining fraction of π^0's not identified, the sensitivity of ICARUS to $\nu\mu \leftrightarrow \nu_e$ oscillations is expressed as the sensitivity area shown in Figure 13a for 80 GeV protons on target, and in Figure 13b for 400 GeV protons on target. This study covers essentially the full energy range of the SPS beam, since the highest possible energy is 450 GeV.

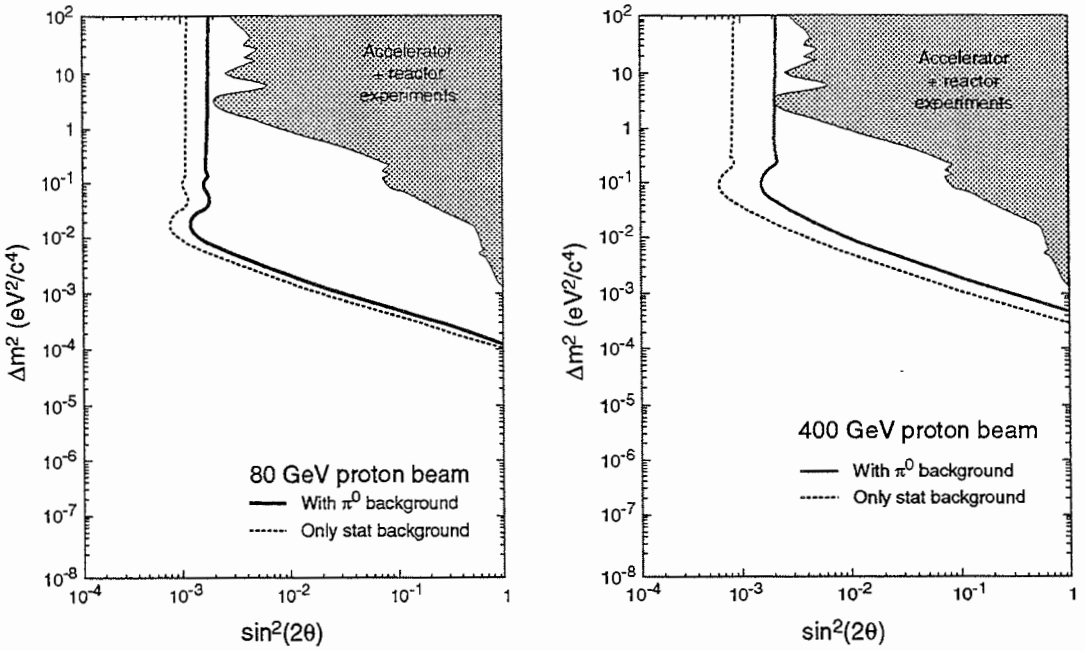

Figure 13 : (a) Sensitivity of ICARUS to $\nu_\mu \leftrightarrow \nu_e$ oscillations for one year of running with 80 GeV protons on target; (b) Sensitivity of ICARUS to $\nu_\mu \leftrightarrow \nu_e$ oscillations for one year of running with 450 GeV protons on target.

Because the fraction of remaining π^0 background is larger at high energy, the optimal conditions are obtained with 80 GeV protons from the CERN SPS (3.0×10^{13} protons on target every 2.4 s). The 400 GeV proton beam gives a similar sensitivity in $\sin^2(2\theta)$ (2.0×10^{-3} vs 1.5×10^{-3}), but a somewhat worse Δm^2 sensitivity (7.5×10^{-4} vs 1.5×10^{-4} eV^2). The difference between the two energies is not huge, and other arguments could encourage us to run at an intermediate energy value, for instance to favour a higher τ production rate.

3.3.2 $\nu_\mu \leftrightarrow \nu_\tau$ oscillations

A priori, at least three different methods can be used to search for ν_τ in the CERN ν_μ beam:

(a) The disappearance method: It consists of measuring the number of muons produced in the rocks near ICARUS and coming from the direction of the CERN beam. This number of muons is proportional to the number of ν_μ's contained in the beam. It is then compared with the total number of neutrino interactions (both charged and neutral-current) in the detector, which is proportional to all neutrino flavours. The ratio R_d measured can be expressed as:

$$R_d = \frac{\sigma_\mu + \sigma_\tau \left[\frac{\nu_\tau}{\nu_\mu}\right] Br(\tau^- \to \mu^- \nu_\tau \bar{\nu}_\mu)}{\left[\sigma_e \left[\frac{\nu_e}{\nu_\mu}\right] + \sigma_\mu + \sigma_\tau \left[\frac{\nu_\tau}{\nu_\mu}\right]\right][1+\alpha]}$$

where σ's are charged-current cross-sections, α is the neutral current factor and ν_x is the number of ν_x particles present in the beam. The ratio ν_e/ν_μ is extremely well known from the $\nu_\mu \leftrightarrow \nu_e$ oscillation search, and therefore the measurement of R_d provides a measurement of the ν_τ content. Table 2 gives the corresponding sensitivity of ICARUS.

Table 2 : Sensitivity of ICARUS to $\nu_\mu \leftrightarrow \nu_\tau$ oscillations from the disappearance method

E_P	$\langle E_\pi \rangle$	$\langle E_\nu^{-2} \rangle^{-1/2}$	$N_{CC}(\nu_\mu)$	$\langle \sigma_\tau / \sigma_\mu \rangle$	Δm^2 (stat. BG)	Δm^2 (1% SE)	$\sin^2(2\theta)$ (stat. BG)	$\sin^2(2\theta)$ (1% SE)
80	25.7	5.9	4000	0.18	$1.4\ 10^{-3}$	$1.6\ 10^{-3}$	$1.0\ 10^{-1}$	$1.4\ 10^{-1}$
160	48.9	9.0	10800	0.31	$1.6\ 10^{-3}$	$2.1\ 10^{-3}$	$5.2\ 10^{-2}$	$8.9\ 10^{-2}$
240	72.7	12.0	19800	0.38	$1.7\ 10^{-3}$	$2.5\ 10^{-3}$	$3.4\ 10^{-2}$	$7.2\ 10^{-2}$
320	95.4	14.8	29800	0.45	$1.8\ 10^{-3}$	$2.9\ 10^{-3}$	$2.5\ 10^{-2}$	$6.3\ 10^{-2}$
400	120	17.8	41500	0.50	$2.0\ 10^{-3}$	$3.4\ 10^{-3}$	$2.4\ 10^{-2}$	$4.0\ 10^{-2}$

(b) The appearance method: It consists of comparing the number of ν_μ charged-current interactions in the detector with the number of neutral current interactions which is proportional to the combined ν_μ and ν_τ number. The ratio R_a gives a measurement of the ν_τ content of the beam. Table 3 shows the sensitivity expected in the appearance method.

$$R_a = \frac{\sigma_\mu + \sigma_\tau \left[\frac{\nu_\tau}{\nu_\mu}\right] Br(\tau^- \to \mu^- \nu_\tau \bar{\nu}_\mu)}{\left[\sigma_e \left[\frac{\nu_e}{\nu_\mu}\right] + \sigma_\mu + \sigma_\tau \left[\frac{\nu_\tau}{\nu_\mu}\right]\right]\alpha + \sigma_\tau \left[\frac{\nu_\tau}{\nu_\mu}\right] Br(\tau^- \to \mu^- \nu_\tau \bar{\nu}_\mu)}$$

The two methods could be combined to provide an overall sensitivity which is somewhat better than the result of each method taken alone. One should be careful to take into account the correlation which exists since the two measurements make use of neutral-current events.

We estimate that the resulting ICARUS sensitivity for $\nu_\mu \leftrightarrow \nu_\tau$ oscillations extends at least to $\sin^2(2\theta) = 5.0 \times 10^{-2}$, and $\Delta m^2 = 2.0 \times 10^{-3}$ eV^2. A possible improvement which we intend to study is to enrich the data samples in ν_τ events by using topological and kinematical properties of tau events. Therefore we expect that the above number is a conservative estimate.

Table 3 : Sensitivity of ICARUS to $\nu_\mu \leftrightarrow \nu_\tau$ oscillations from the appearance method

E_P	$\langle E_\pi \rangle$	$\langle E_\nu^{-2} \rangle^{-1/2}$	$N_{CC}(\nu_\mu)$	$\langle \sigma_\tau / \sigma_\mu \rangle$	Δm^2 (stat. BG)	Δm^2 (1% SE)	$\sin^2(2\theta)$ (stat. BG)	$\sin^2(2\theta)$ (1% SE)
80	25.7	5.9	4000	0.18	$1.1\ 10^{-3}$	$1.3\ 10^{-3}$	$5.6\ 10^{-2}$	$7.9\ 10^{-2}$
160	48.9	9.0	10800	0.31	$1.2\ 10^{-3}$	$1.7\ 10^{-3}$	$2.9\ 10^{-2}$	$5.6\ 10^{-2}$
240	72.7	12.0	19800	0.38	$1.3\ 10^{-3}$	$2.0\ 10^{-3}$	$2.0\ 10^{-2}$	$4.9\ 10^{-2}$
320	95.4	14.8	29800	0.45	$1.4\ 10^{-3}$	$2.4\ 10^{-3}$	$1.4\ 10^{-2}$	$4.1\ 10^{-2}$
400	120	17.8	41500	0.50	$1.5\ 10^{-3}$	$2.8\ 10^{-3}$	$1.2\ 10^{-2}$	$4.0\ 10^{-2}$

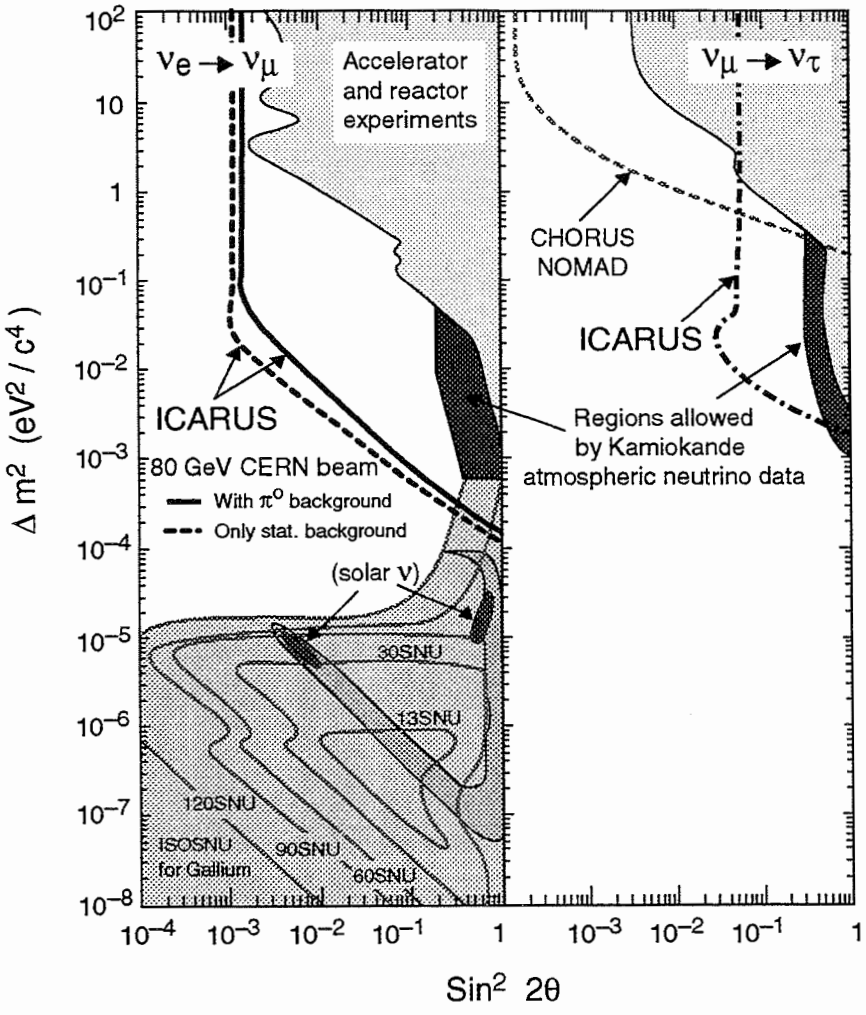

Figure 14 : The sensitivity of ICARUS to vacuum $\nu_\mu \leftrightarrow \nu_e$ and $\nu_\mu \leftrightarrow \nu_\tau$ oscillations, for one year of data with one module

(c) In principle, direct appearance measurements can also be performed: A study [6] has shown that the ICARUS technique allows one to search for ν_τ charged-current events producing a tau lepton. Several channels

may be used, for instance $\tau^- \rightarrow \pi^- \pi^+ \pi^- \nu_\tau$. However, at this stage we do not know whether the chosen wire pitch will allow for sufficient precision to detect τ leptons this way. One may be able to make use of the characteristic kinematic and topological properties of τ events to enrich the sample, but this study still has to be done.

In summary, with the use of the CERN neutrino beam, ICARUS will search for vacuum oscillations and reach all of the interesting region indicated by Kamiokande atmospheric neutrino data. As shown in Figure 14, the sensitivity of ICARUS to $\Delta m^2_{\mu e}$ and $\Delta m^2_{\mu \tau}$ versus the respective mixing parameters will cover a very large currently unexplored region.

3.3.3 Matter effects

The favourite explanation for the solar neutrino puzzle [7] is enhanced neutrino mixing in matter through the so-called MSW mechanism [8]. It is obviously crucial to be able to study such an effect in an experiment with complete control of the main parameters possibly driving the phenomenon, namely neutrino energy, density of matter, and amount of matter traversed. The CERN neutrino beam to Gran Sasso will provide for the first time artificially produced neutrinos travelling through a substantial amount of matter under controlled conditions. No matter what the outcome may be, new ground will be explored in the study of the interaction of CERN neutrinos with the 732 km of Earth along the path between CERN and Gran Sasso.

For beams travelling through the Earth, in addition to neutrino vacuum oscillations discussed in the preceding paragraph, there also exists the possibility to study matter effects, which should be present if neutrinos have a non-zero mass. The MSW effect, apart from requiring non-zero neutrino masses, is entirely due to otherwise Standard Model effects, based on the fact that ν_e's and ν_μ's have different interactions with electron-rich matter. This difference in interactions induces an effective mixing between ν_e's and ν_μ's. Under certain energy and density conditions, the mixing becomes very large and, provided the matter density does not vary too abruptly, there can be conversion of one neutrino state into the other.

The average matter density in the Earth (5.5 g/cm^3) is five times larger than in the sun. If matter effects exist in the sun, they should also occur in the Earth. The MSW resonance condition requires that the product of neutrino energy with matter density be a constant. This implies that even if the resonance in the sun occurs at very high densities found near the centre of the sun, of the order of 150 g $\cdot$ cm^{-3} (Figure 15a), it will be possible to reproduce the effect at lower matter density found in the Earth (13 g $\cdot$ cm^{-3} at the centre of the Earth) (Figure 15b), provided the neutrino energy selected is higher by the corresponding factor. For a neutrino beam going through the centre of the Earth, the resonance spectrum [9] in the conversion of ν_μ's into ν_e's is dominated by two main structures (Figure 16), the effect of the Earth's core and the effect of the Earth's mantle. A beam observed 10 000 km away, for instance at the location of SuperKamiokande, would provide spectacular resonance (Figure 17), corresponding to the mantle structure only, since in this case the beam does not reach the Earth's core.

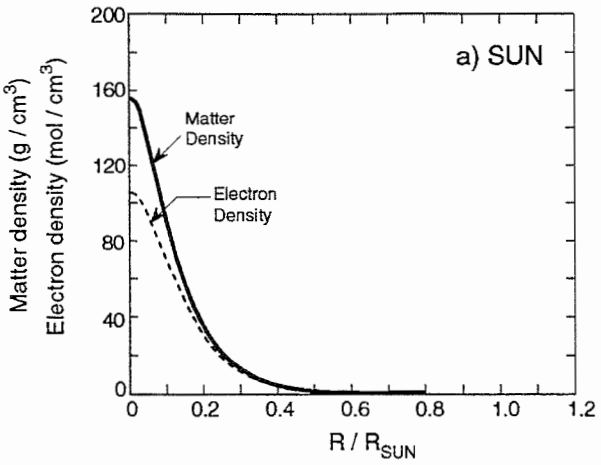

Figure 15a : Matter and electron density in the sun as a function of dimensionless radius

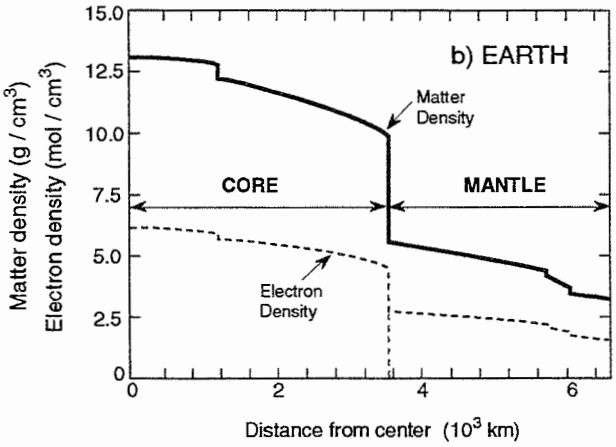

Figure 15b : Matter and electron density in the Earth as a function of distance from the centre

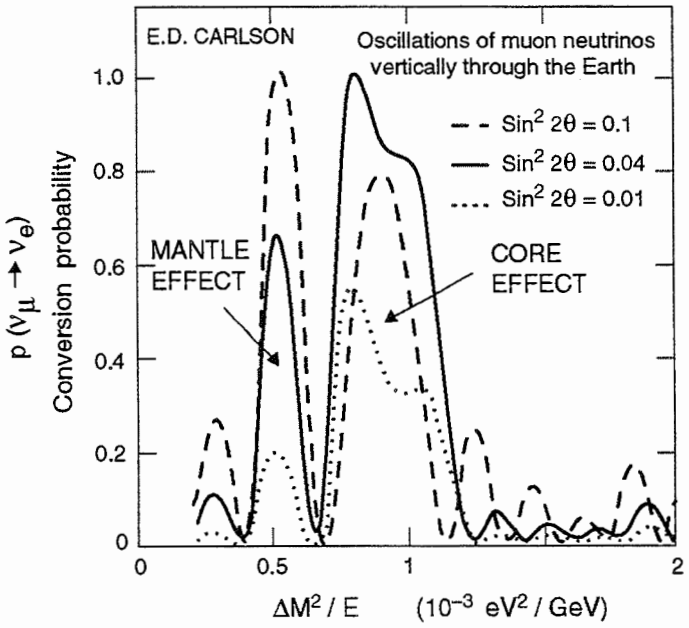

Figure 16 : Matter oscillation pattern for neutrinos travelling through the Earth vertically, and for different values of the mixing parameter in vacuum

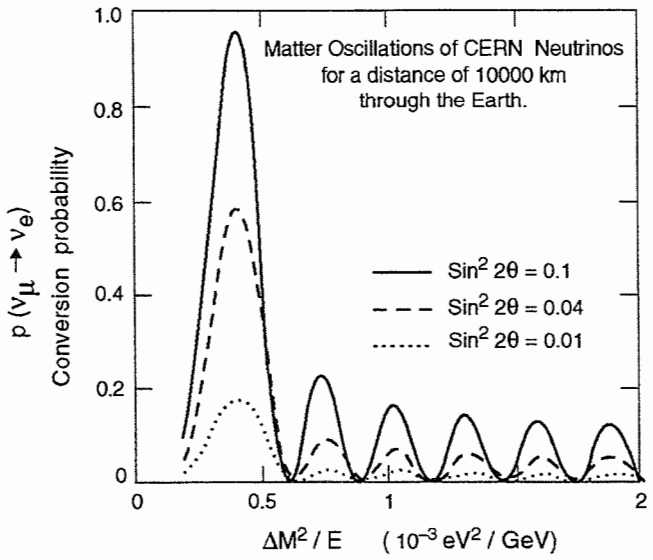

Figure 17 : Matter oscillation pattern for CERN neutrinos travelling a distance of 10 000 km through the Earth, and for various values of the mixing parameter in vacuum

In the case of ICARUS at Gran Sasso the effect is present but is unfortunately rather small (Figure 18). However, asymmetry measurements between ν_μ and $\bar{\nu}_\mu$ will double the sensitivity. One should remember that the MSW mechanism depends on the sign of Δm^2. For the simple two-neutrino system, if $\Delta m^2_{\mu e} \equiv m_{\nu\mu}{}^2 - m_{\nu e}{}^2$ is positive the resonance condition will occur with neutrinos but not with antineutrinos. Conversely, if $\Delta m^2_{\mu e}$ is negative the resonance condition will occur with antineutrinos.

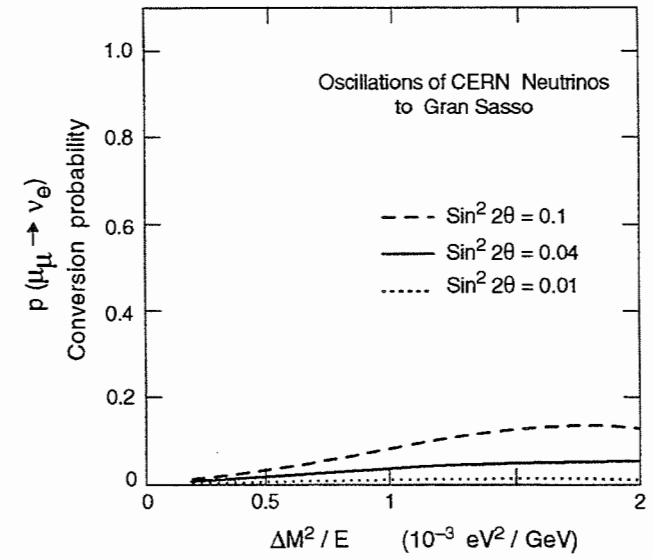

Figure 18 : Matter oscillation pattern of CERN neutrinos travelling through the Earth to Gran Sasso, and for various values of the mixing parameter in vacuum

Let us assume that $\Delta m^2_{\mu e}$ is positive. Even though there is no resonance in the case of antineutrinos, one finds that the effective mixing induced by the presence of matter is smaller than in the pure vacuum case. Therefore, if one were to compare the neutrino case with the antineutrino

case, one would find that the effect is amplified, by about a factor two for ICARUS and for a neutrino beam from 450 GeV SPS protons (Figure 19) [10]. We therefore intend to take data with both polarities of the neutrino horn, selecting negative or positive hadrons to produce antineutrinos or neutrinos. Since the beam intensity is smaller for antineutrinos and because the antineutrino cross-section in liquid argon is smaller than for neutrinos, a longer running time (a factor 4) will be required for antineutrinos if one needs to achieve the same statistical significance as with neutrinos. However, if there were any hint of an effect with neutrinos, it would certainly be worth while to take data with antineutrinos. One should also remember that data-taking with the beam is done while the detector is taking data for proton decay or other neutrino physics. There is no need for a dedicated beam data-taking period.

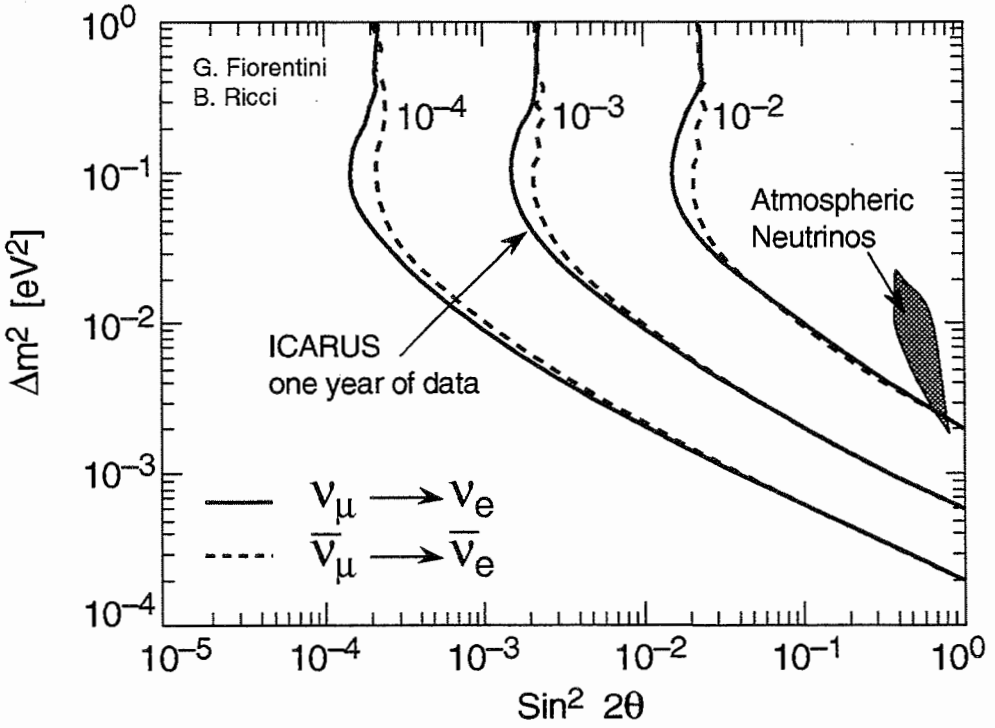

Figure 19 : Curves of constant oscillation probability shown separately for neutrinos and for antineutrinos. With one year of data-taking ICARUS should be sensitive to probabilities smaller than 10^{-3}.

The conclusion of long-baseline studies with ICARUS making use of a CERN SPS neutrino beam is that a new domain will be explored where we have reasons to believe (solar neutrinos and atmospheric neutrinos) that new physics is happening.

3.4 Proton decay background calibration

The neutrino beam from CERN will provide a rich sample of events which can be used to finely tune the detector calibration, with a view to reducing as much as possible the systematic error in the estimation of proton decay background in the channels where the background is not negligible.

By setting the beam energy at the appropriate value, the lowest possible energy allowed by the SPS, we can search for proton decay candidates in events from the beam for which we know both the direction and the timing. For instance, with 80 GeV protons on target one can collect in one year of running about 4000 charged-current events at an average neutrino energy of about 5.9 GeV. Even though the rate of events is low, it will be very useful to study a controlled sample of events whose kinematics and signature approach that expected for proton decays. In addition, the large sample of hadrons produced ($\pi^{\pm}$, $K^{\pm}$ etc.) will be used as a check of the calibration of dE/dx versus range for a large class of particles, as well as a general tuning of the detector simulation.

It should be noted that these calibration runs can take place while data-taking is proceeding for all the other physics items.

3.5 References

[1] A. Ball, B. Bianchi, J.P. Revol, G. R. Stevenson and E. Weisse, CERN Beams for Long Baseline Neutrino Oscillation Experiments, CERN-SL/Note 92–75 (BT), December 1992, unpublished.

[2] M. Mayoud, CERN AT/SU, private communication.

[3] Design Study of the Large Hadron Collider (LHC), (Pink Book), CERN 91–03, May 1991.

[4] A. Ball et al., Simulation of a CERN SPS Neutrino Beam to Gran Sasso, to be published.

[5] D.S. Baranov et al., Sov. J. Nucl. Phys. **41** (6) 963 (1985).

[6] F. Pietropaolo, The ICARUS Collaboration, The ICARUS Liquid Argon TPC: a New Detector for ν_τ Search, Proc. 2nd Int. Conf. on Calorimetry in High Energy Physics, ed. A. Ereditato, Capri, 1991.

[7] J.N. Bahcall, Solar Models and Experiments, Proc. Rencontres de Physique de la Vallée d'Aoste 1993, March 8, 1993, ed. M. Greco.

[8] L. Wolfenstein, Phys. Rev. **D17** (1978) 2369; **D20** (1979) 2634; S.P. Mikheyev and A.Yu. Smirnov, Yad. Fiz. **42** (1985) 1441; Nuovo Cim. **9C** (1986) 17; H. Bethe, Phys. Rev. Lett. **56** (1986) 1305.

[9] E.D. Carlson, Terrestrially Enhanced Neutrino Oscillations, Phys. Rev. **D34** (1986) 1454.

[10] G. Fiorentini and B. Ricci, Old and New Interactions in Long Baseline Neutrino Experiments, INFN Ferrara 06-93, Proc. of Workshop on Neutrino Telescopes, Venice, March 1993, ed. M. Baldo-Ceolin.

4. Solar neutrinos

ICARUS II is optimized for the study of rare events that deposit in the detector a relatively large energy, such as those coming from proton decays, atmospheric and long-baseline neutrinos. In particular this leads us to accept a space granularity of the order of a few millimetres and to use materials that will not necessarily be selected on the basis of their very low content of radioactive contaminants, mainly for cost reasons. As a consequence ICARUS II may not be optimized for solar-neutrino physics. However, ICARUS II can also play an important role in this field, because its large mass, more than an order of magnitude larger than that of ICARUS I, compensates, at least partly, for the coarser space resolution and also provides a very welcome self-shielding for the inner volume. We describe here our present understanding of the capability of ICARUS II with regards to solar-neutrino physics, keeping in mind that the precise knowledge of the ultimate detector performance will require a final detector design and will also benefit from experience gained in operating the detector under experimental conditions.

4.1 The ICARUS real-time detector of solar neutrinos

The solar neutrino puzzle is one of the most challenging issues of modern physics. As shown in the atmospheric neutrino section, ICARUS will address the question of solar neutrinos in an original way, by studying the interaction of atmospheric neutrinos with the Earth. If the Mikheyev–Smirnov–Wolfenstein (MSW) effect [1] is in action in the sun for neutrino energies ranging from 1 to 10 MeV, a similar effect must take place in the Earth, but for an energy range of 10 to 1000 MeV which is precisely the atmospheric neutrino energy range. It is of course also very important for ICARUS to directly observe solar neutrinos. The four present experiments [2] have shown the existence of an apparent solar neutrino deficit, however the effect, if confirmed, needs to be determined with precision and an explanation needs to be found either in terms of a modification of the Standard Model of particle physics or in terms of a modification of the Standard Solar Model (SSM). ICARUS can provide a definite answer by observing directly the solar neutrino flux and without having to rely on a comparison with a solar model. If neutrino oscillations are responsible for the solar neutrino deficit, a fraction of ν_e's produced near the centre of the sun could transform into $\nu_{\mu, \tau}$'s not detected in the radiochemical detectors. Two mechanisms are considered: (a) vacuum oscillations, however, this possibility, even though consistent with all experimental results so far, requires that the distance between the Earth and the sun just happens to be what it takes to produce the effect, an unlikely situation; (b) enhancement of neutrino oscillations by the presence of high-density electron-rich matter, the so-called MSW effect. It is therefore crucial to be able to detect at the same time the ν_e flux and the ν_μ, ν_τ fluxes to confirm that ν_e's which have disappeared through oscillations did transform into the other neutrino species.

ICARUS can detect solar neutrinos by observing the electron produced in the following two reactions [3]:

(a) $\nu_{e,\mu,\tau} + e^- \rightarrow \nu_{e,\mu,\tau} + e^-$ (elastic scattering on electrons)

(b) $\nu_e + {}^{40}Ar \rightarrow {}^{40}K^* + e^-$ (absorption on the argon nucleus)

Process (b) is known as inverse β-decay.

The unique capabilities of the ICARUS liquid argon Time Projection Chamber (self-triggering, 3D-imaging, energy measurement with good resolution and continuous sensitivity), together with the high density of liquid argon, are suitable to the real-time detection of the neutrinos produced in the sun. Because of the increasing backgrounds (mainly radioactivity) at low energy, there is a minimum threshold (a few MeV) below which electrons produced by solar neutrinos cannot be distinguished from other sources. Therefore our device is only sensitive to the ^8B part of the solar cycle [4] (Figure 1).

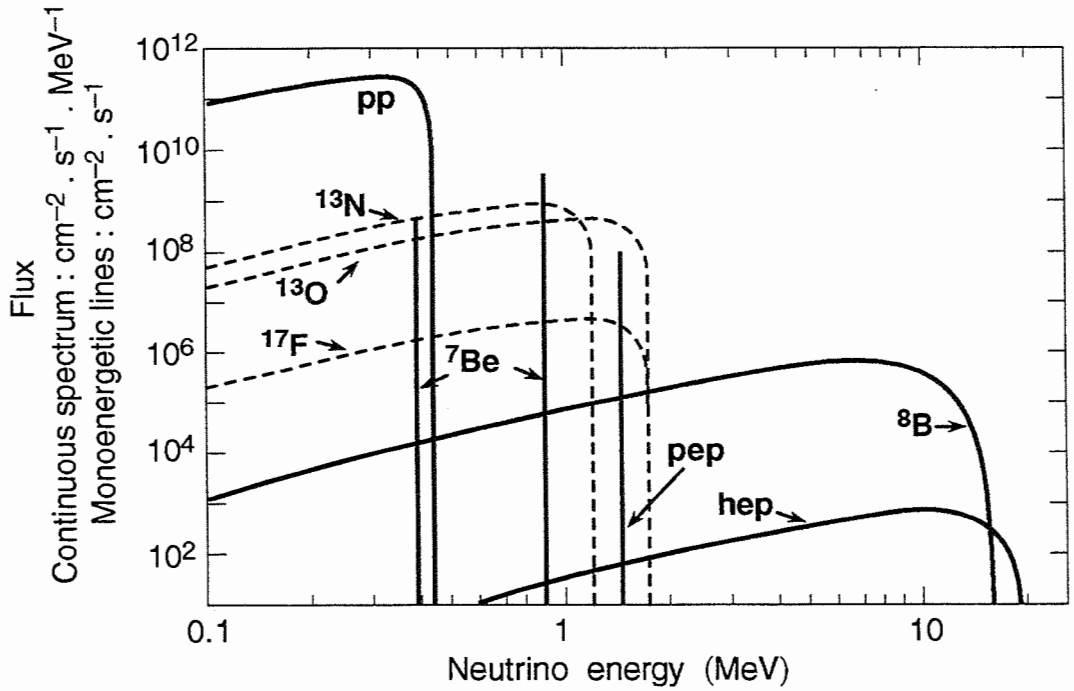

Figure 1 : The solar neutrino energy spectrum according to the Standard Solar Model

In the elastic scattering reaction, the electron is emitted with a small angle with respect to the direction of the incident neutrino. For example electrons with energy larger than 5 MeV are emitted within a cone of 18° with respect to the direction of the sun. Therefore an angular cut will help to reject backgrounds which all have isotropically distributed electrons. The rejection power will depend on the accuracy in the electron direction measurement, and, to a lesser extent, on the energy resolution.

In the absorption reaction, however, there is no correlation between the electron and sun directions, but another signature can be used. Since the ^{40}K is mostly produced in an excited state, it will decay to the ground state through the emission of one or several photons. Therefore the absorption events can be characterized by the presence of one electron accompanied by several photons. The ^8B solar neutrinos have an energy ranging up to 15 MeV

and the Q value in reaction (b) is 1.5 MeV, therefore, in the case of the pure Fermi super-allowed transition to the isobaric analogue state of ^{40}K, 4.38 MeV above the ground state, the electrons produced have a maximum energy of about 9 MeV. Other transitions (Gamow–Teller) are also possible mainly to a level 2.29 MeV above the ground state, and in that case, the electrons are produced with a maximum energy of 11 MeV. The ^{40}K* de-excitation γ rays will produce a number of Compton electrons, in coincidence with the inverse β-decay electron. These Compton electrons are to be detected in a limited volume around the inverse β-decay electron (about 0.5 m^3).

In order to correctly relate the measured number of absorption events to the original solar ν_e flux, the neutrino capture cross-section by ^{40}Ar must be well estimated. Whereas the Fermi transition has already been calculated very precisely, recent nuclear-structure computations [5] indicate that Gamow–Teller transitions may give a contribution of the same order of magnitude as the Fermi transition. It is expected that those Gamow–Teller contributions to the cross-section will soon be calculated with an adequate accuracy. If needed, an accurate test-beam measurement can be performed to ensure that the uncertainty on the absorption cross-section does not become the main source of systematic error.

The most relevant point is that the measurement by ICARUS of both the absorption events, induced only by ν_e, and of the elastic scattering events, which can occur with all neutrino types (ν_e, ν_μ, ν_τ), provides a direct measurement of the probability of oscillation of ν_e's, independent of the Solar Model. The ratio R of the number of elastic scattering events to the number of absorption events which can be expressed as :

$$R = \frac{P_{\nu_e \to \nu_e}\sigma\left(\nu_e\, e \to \nu_e\, e\right) + P_{\nu_e \to \nu_\mu}\sigma\left(\nu_\mu\, e \to \nu_\mu\, e\right) + P_{\nu_e \to \nu_\tau}\sigma\left(\nu_\tau\, e \to \nu_\tau\, e\right)}{P_{\nu_e \to \nu_e}\sigma_{absorption}} \quad (1)$$

is in one-to-one correspondence with the oscillation probability P ($\nu_e \to \nu_{\mu,\tau}$) and most importantly is independent of the magnitude of the solar neutrino flux.

Figure 2a shows the oscillation probability as a function of R including only the contribution from the Fermi transition; the inclusion of the Gamow–Teller transitions can only increase the sensitivity of the method.

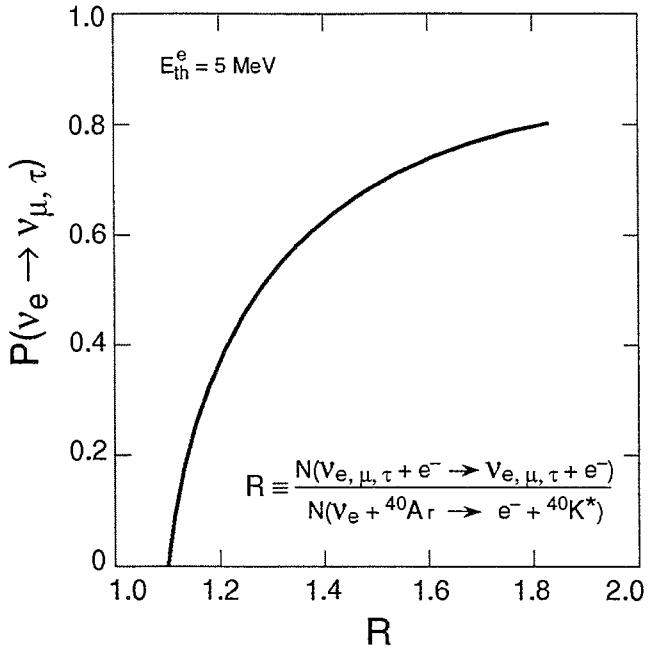

Figure 2a : The oscillation probability P ($\nu_e \leftrightarrow \nu_\mu, \tau$) as a function of the ratio R between elastic scattering and absorption rates for 5 MeV threshold

As described in more detail in the following paragraphs, with a 5 MeV threshold on the electron energy, we expect to have 65% detection efficiency for elastic scattering events and 80% for absorption events. Assuming the SSM to be valid, we expect to collect about 2730 elastic scattering and 3000 (pure Fermi transition only) absorption events per year and per one ICARUS module. After a period of two years of data-taking and for one module, the statistical error on R is 1.9%. Beyond this level the knowledge of R becomes limited mainly by the systematic uncertainties, including those from the absorption cross-section. Assuming after two years a total uncertainty of 3.5% we can detect a 20% or more neutrino oscillation probability corresponding to a value of R larger than 1.15 at 90% C.L.

It is convenient to introduce the ratio $R' \equiv R/R_0$, where R_0 is the value of R in absence of oscillations, and to study curves of constant R' in the $\nu_\mu \leftrightarrow \nu_e$ oscillation parameter space ($\sin^2 2\theta$, Δm^2). These are shown in Figure 2b. The above evaluated sensitivity corresponds to R' larger than 1.05 at 90% C.L. The regions allowed by the present solar neutrino experiments are well within the sensitivity region of ICARUS. The R parameter does not contain all the information; additional information is contained in the shape of the electron energy spectrum. An improved sensitivity could be reached from a further study of systematic effects (in particular if a lower energy threshold can be used for the absorption event selection) combined with experience with the real data.

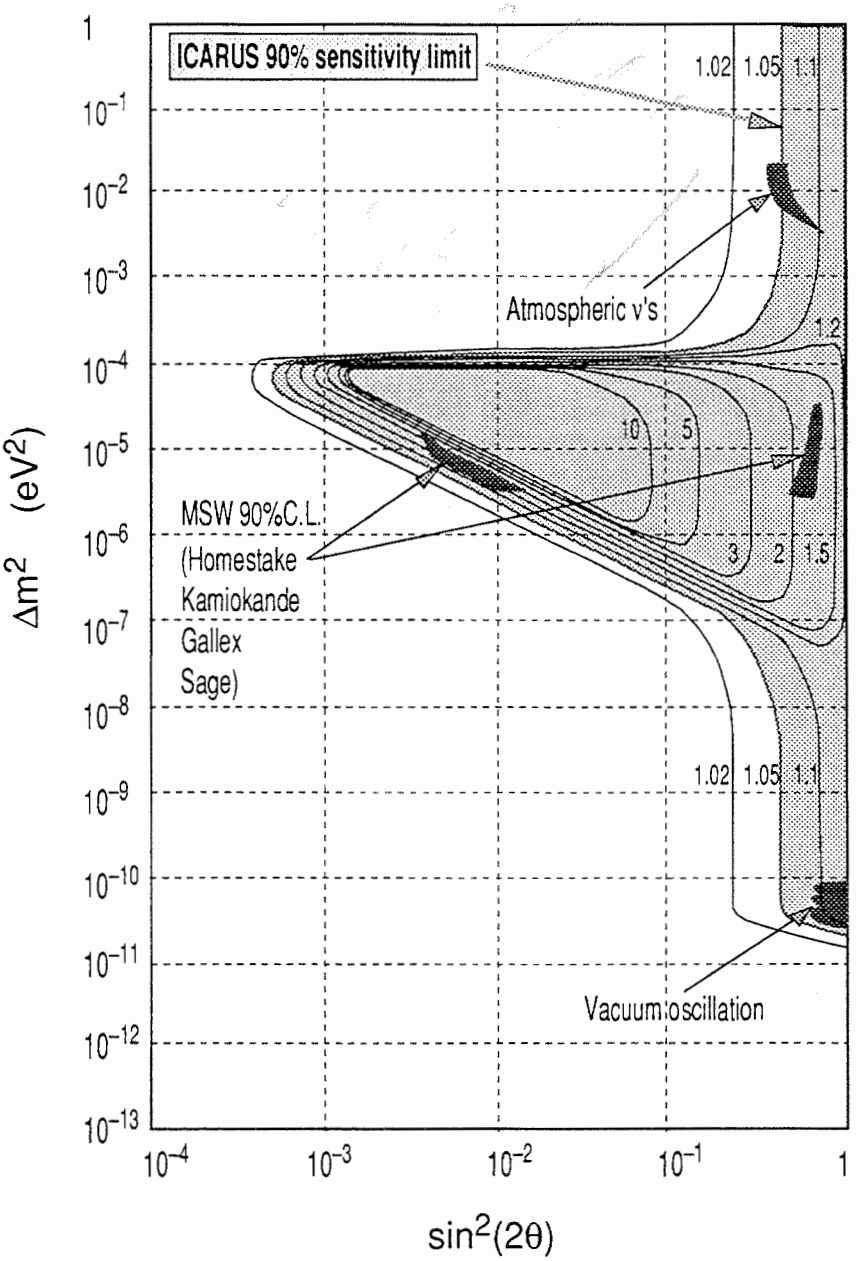

Figure 2b : Curves of constant ratio R' in the ($\sin^2 2\theta$, Δm^2) plan for $\nu_\mu \leftrightarrow \nu_e$ oscillations. The three areas currently allowed by solar neutrino experiments and the Kamiokande atmospheric neutrino area are indicated. The ICARUS sensitivity after two years is shown by the shaded area (90% C.L.).

4.2 Monte Carlo simulation of elastic scattering events

Since in ICARUS solar neutrinos can only be detected above a threshold of several MeV only ^{8}B and hep neutrinos contribute to the data sample. The signature of elastic scattering events is the presence of an electron with energy up to 15 MeV, pointing roughly to the direction of the sun. The lower energy threshold will be determined by the radioactive noise level present in the real experimental environment; we will assume here that we can achieve a 5 MeV threshold on the recoil electron energy. Notice also that if the energy is too low the direction of the electron track cannot be accurately

determined (for instance a 5 MeV electron has a range of only about 20 mm, that gives a maximum of five contiguous sense-wires with a signal).

A full simulation of ^8B neutrino elastic scattering events in liquid argon was made. The total and differential cross-sections used are those reported in Reference [4]. The neutrino directions are randomly generated in the plane of the ecliptic and the detector is assumed to be the liquid argon cylinder fitted in the Hall C of the Gran Sasso Laboratory (128° azimuth) (see Chapter III). The scattered electron is reconstructed taking into account multiple scattering, ionization losses, Møller scattering and bremsstrahlung (the secondary electrons from Compton scattering or pair conversion are also reconstructed down to 20 KeV kinetic energy) [6].

The kinematics [7] of the elastic scattering reaction results in a simple relation between the scattered electron kinetic energy (E_e) and the angle α between the direction of the sun and the electron momentum vector:

$$2(1-\cos\alpha) = \frac{1}{E_e} - \frac{1}{E_\nu} \qquad (2)$$

where E_ν is the incident neutrino energy. The study of the effect of energy resolution, bremsstrahlung and multiple scattering indicates that requiring the electron momentum to be in the direction of the sun within, for instance, 25 degrees, rejects 90% of the isotropic background and selects 65% of the solar neutrino events, for an electron energy threshold of 5 MeV (Figure 3). The background rejection takes into account the ambiguity which may exist in recognizing which end of the electron track corresponds to the beginning of the track. The energy resolution does not play a crucial role what is most important is the measurement of the electron direction whose resolution is mainly determined by the multiple scattering in the liquid argon.

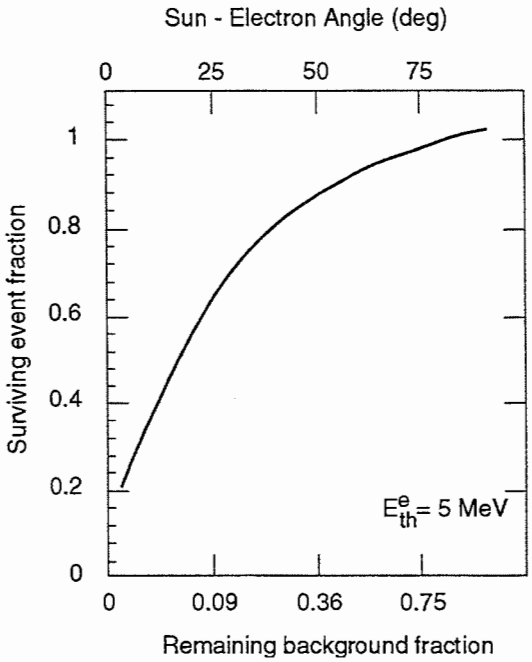

Figure 3 : Detection efficiency as a function of the cut on the angle between the reconstructed electron and the sun direction (top scale) and as a function of the remaining background fraction (bottom scale)

Figure 24 (Chapter V) shows a 5 MeV electron event observed in our 3-ton prototype using a radioactive gamma-ray source. In our study the Monte Carlo simulation has been tuned using the parameters obtained with our 3-ton prototype, in particular an electronic noise (Gaussian of 500 electrons r.m.s.) has been included. Monte Carlo events were treated with a procedure similar to the one used to analyse real data. We find that 800 events/kton/year are produced above 5 MeV threshold (Figure 4).

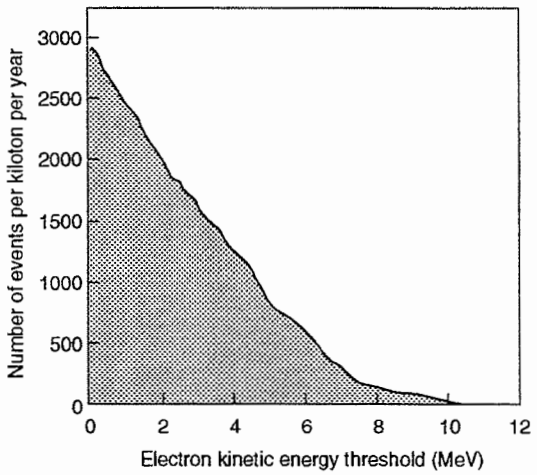

Figure 4 : Expected number of events per kiloton, as a function of the electron kinetic energy threshold (elastic scattering only)

4.3 Monte Carlo simulation of absorption events

Very recent calculations [5] show that, in addition to the super-allowed Fermi transition to the 4.38 MeV excited analogue state of ^{40}K, there is also an important contribution to the total absorption cross-section, due to the allowed Gamow-Teller (GT) transitions. Preliminary results predict a contribution of 4.85 SNU for GT transitions for electrons above 5 MeV to be compared to the 2.23 SNU expected from Fermi transitions (SSM assumed in both cases). A detailed calculation is in preparation [5] and will also be complemented by a test-beam measurement if needed.

The experimental signature for absorption events is the following:

a) the presence of an electron with an approximately isotropic distribution and an energy ranging from the threshold ($\approx$ 5 MeV) to 12 MeV,

b) the presence of a number of Compton electrons, produced by the photons from the de-excitation of the ^{40}K* nucleus. The energy of the Compton electrons ranges up to about 2 MeV and is deposited substantially in a single 'pixel' of the detector. This single pixel must be distinguished from the background. Assuming that a safe threshold for this is ten times the average electronic noise, we will be able to recognize electrons down to 300 keV. It is clear that for the detection of the absorption process it is particularly important to achieve the lowest possible energy threshold to be sensitive to the largest part of the ^{8}B neutrinos from the sun.

In this low-energy range the background plays an essential role. We consider a spherical volume around the electron, 50 cm in radius, i.e. about three radiation lengths, in which to search for an additional energy deposition

from Compton electrons. The background is due to any ionizing event depositing between 2 and 4 MeV (see later) in time coincidence with the primary electron within a complete drift time, which is about ± 250 μs. We have used the 3-ton prototype to evaluate a very conservative upper limit for this type of background, by counting the contained events that give an energy deposit between 2 and 4 MeV in a sensitive volume of 18 litres. The rate is 0.77 Hz, corresponding to 21 Hz when extrapolated to the 50 cm radius sphere. This value is certainly an upper limit because it includes the contribution of the radioactivity of our dewar (that has been exposed to a beam) and of many nearby concrete blocks and from cosmic rays (our prototype is located at CERN, not in the Gran Sasso tunnel). In particular, the measurement shows that the contribution from ^{42}Ar to this specific background is negligible. The measured 21 Hz upper limit would imply the presence of background in 4% of the events; in practice it will be much lower and is therefore not a problem for us.

The other type of background to consider comes from the bremsstrahlung photons emitted by electrons of kinematic energy in the range considered here. About 53% of the electrons from solar neutrinos with an energy above 5 MeV produce, through bremsstrahlung, a Compton electron of energy larger than 300 keV.

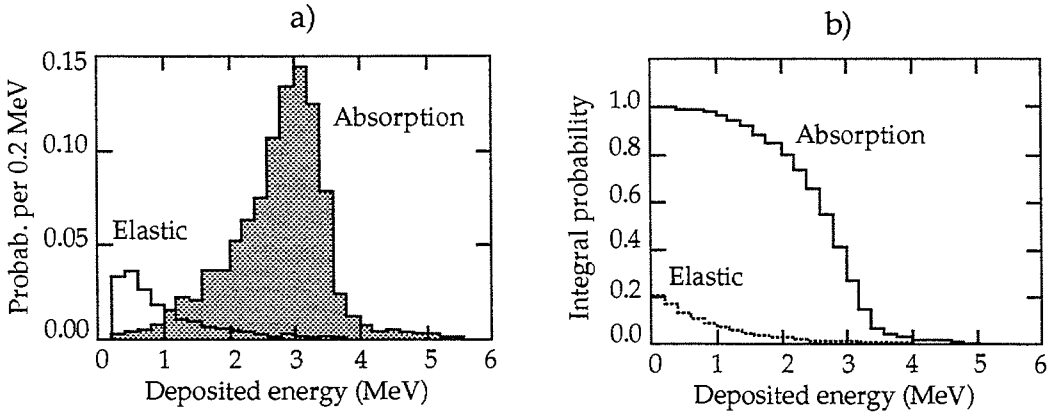

Figure 5 : Energy deposited in addition to the inverse β-decay electron in a 50 cm radius sphere around the primary electron vertex: (a) differential probability distributions; (b) integral probability distribution.

We have performed a Monte Carlo simulation of Compton electron production by de-excitation photons and evaluated the total energy deposited by the photons above 300 keV inside the 50 cm radius sphere centred on the inverse β-decay electron. The probability density distribution shown in Figure 5a is peaked between 2 and 4 MeV. Therefore we can reduce the background by requiring that the energy deposition be larger than about 2 MeV. To evaluate the effectiveness on background suppression we have simulated the process of Compton electrons production by bremsstrahlung from the neutrino elastic scattering electron. Results are also shown in Figure 5. One can see that indeed the discrimination can work. If we require a total extra energy deposition between 2 and 5 MeV, the efficiency for the absorption process is about 80%, while the remaining background fraction is 5%. Alternatively, if we require a multiplicity of associated Compton electrons larger than three, the efficiency for absorption events is 80% and the

remaining elastic events contamination reduces to 1%. This demonstrates that in the final analysis it is possible to choose an optimized combination of the above cuts to obtain both a high selection efficiency for absorption events and, at the same time, an excellent rejection against background.

4.4 Low-energy background considerations

There are several sources of background which can produce single electrons with energy above the chosen threshold. These backgrounds affect both elastic and absorption events (down to a few MeV for elastic scattering events and a few hundred keV for absorption events). We refer the reader to Reference [3] for a detailed analysis of these low-energy backgrounds. A practical summary of conclusions is presented here.

4.4.1 Intrinsic radioactivity of natural liquid argon

Most of the argon isotopes are radioactive with very short half-lives (less than a few days), so that they, and the electrons they produce by β-decay, disappear very quickly. The relevant exceptions are ^{39}Ar (producing β electron up to 565 keV), and ^{42}Ar (producing β electrons up to 3520 keV). More specifically ^{39}Ar and ^{42}Ar have a half-life of 269 and 33 years respectively. The latter isotope might have been produced by thermonuclear explosions in the atmosphere through double neutron capture by ^{40}Ar nuclei. Its concentration is unknown. Recently, a search for ^{42}Ar in natural liquid argon was performed at the Gran Sasso Laboratory by a Collaboration between the University of Milan, the ICARUS Group and the LNGS by means of gamma spectroscopy with a germanium detector [8]. The ^{42}Ar concentration was estimated from the counting rate in an energy window around 1.526 MeV. Taking into account the Ge efficiency, determined by Monte Carlo simulation, and fitting the spectrum with a maximum likelihood method on a linear background, we deduced an upper limit on the ^{42}Ar concentration in natural liquid argon:

$$\frac{N_{^{42}\mathrm{Ar}}}{N_{^{40}\mathrm{Ar}}} < 1.2 \times 10^{-18} \qquad (90\%\ \mathrm{C.L.})$$

Further measurements are in preparation to lower the present upper limit by at least one order of magnitude.

However, the actual value may be several orders of magnitude lower than our present limit. Recently Terrani et al. [9] have calculated the ^{42}Ar concentration scaling from the measured value of the increase factor of ^{14}C due to nuclear explosions. This factor is between 1.5 and 2 and is due to a single neutron capture process. This value can be scaled to the ^{39}Ar formation from single neutron capture on the natural ^{38}Ar isotope. Scaling by the ^{39}Ar/^{42}Ar ratio and taking into account the ratio of the double versus single capture probabilities (which depends on the natural neutron flux which in turn depends on the nuclear weapon yield), the calculation gives a concentration of 10^{-21} for ^{42}Ar in natural argon and of 10^{-20} for ^{39}Ar, about three orders of magnitude smaller than the measured limit! In this case these isotopes would not constitute a background in ICARUS.

Taking conservatively the measured upper limit, Figure 6 shows the expected differential rate due to ^{42}Ar β-decay in an ICARUS module. The spectrum ends at 3.5 MeV. The total rate corresponding to the measured upper limit (10^{-18}) is 1.13×10^5 Hz. The rate in the higher energy part of the spectrum, say between 3 and 3.5 MeV would be as high as 200 Hz. In the pessimistic hypothesis made, this contribution to the background to the electrons from solar neutrinos depends critically on the threshold and on energy resolution. With our prototype at CERN, we achieved an energy resolution of 7% for electrons in this energy range. The 5 MeV threshold is at 7σ from the 3 to 3.5 MeV energy bin. If we assume a Gaussian energy resolution function we can evaluate that the number of expected events over threshold is a few events per year. If non-Gaussian tails are present we can control this rate by slightly increasing the threshold. Notice also that the measured quantity is the ionization charge. To obtain the corresponding energy we must correct for the effect of the finite electron lifetime. This correction depends on the distance of the event from the readout planes; as a consequence the uncertainties on the knowledge of the $t = 0$ translate into uncertainties on the correction. Again this effect can be controlled increasing the threshold, the high mass of the detector allowing for a comfortable statistics margin.

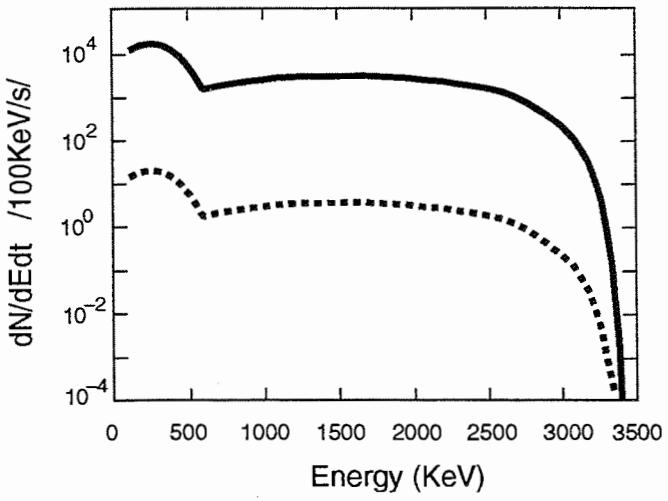

Figure 6: β-ray particle differential rate in one ICARUS module due to ^{42}Ar: (a) experimental upper limit; (b) estimate from ^{39}Ar scaling.

4.4.2 Photons from natural radioactivity

We consider now gamma rays from the natural radioactivity background induced by the experiment environment. From the measurements of the photon flux in Hall C at the Gran Sasso Laboratory [10, 11] we expect to have in one module a total rate of 6.2×10^5 Hz of Compton electrons. The energy spectrum of these electrons extends up to a maximum of 2.4 MeV (Figure 7), so that they constitute a source of background only for the absorption events.

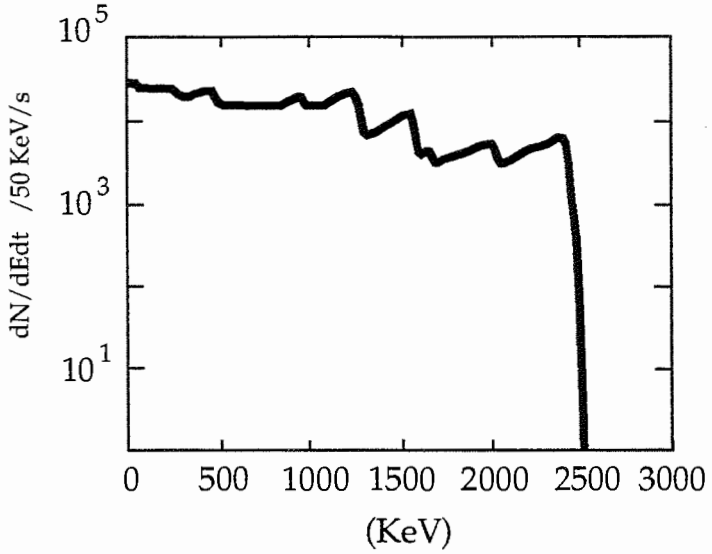

Figure 7 : Natural radioactivity Compton electron differential rate computed from the γ background measured in Hall C at the Gran Sasso Laboratory

It is interesting to note that most of this background is confined to the external region of the detector so that it is possible to find a volume in which the rate is completely manageable. In other words, there exists, thanks to the shielding provided by the liquid argon itself, a large central region of the detector which should be background-free. For instance, if we use an inner region of the detector of 3.5 kton, having around it about 1 metre of liquid argon acting as a shield (the attenuation length for 2.5 MeV photons in liquid argon is ≈ 18 cm), the resulting mean rate reduces to 90 Hz. We conclude that photons from natural radioactivity do not constitute a serious source of background.

4.4.3 Neutron background

Low-energy neutrons are a potential source of dangerous backgrounds. They are produced from the spontaneous fission of uranium or other heavy nuclei contained in the rock, in the stainless steel and other materials around the liquid. The neutron flux has been measured at Gran Sasso by several groups, with different techniques. We use here the most recent measurement of Belli et al. [11], performed in Hall A over a period of several months, using a BF_3 counter with polyethylene layers of various thickness to moderate and count the fast neutron component (Table 1).

Table 1: Energy dependence of the neutron flux in Hall A of the Gran Sasso Laboratory

Neutron energy range	Neutron Flux ($cm^{-2}\ s^{-1}$)
Thermal	$(1.08 \pm 0.02) \times 10^{-6}$
0.05 eV → 1 keV	$(1.84 \pm 0.20) \times 10^{-6}$
1 keV → 5 MeV	$(0.81 \pm 0.15) \times 10^{-6}$
5 → 10 MeV	$(0.05 \pm 0.01) \times 10^{-6}$
> 10 MeV	$(0.60 \pm 0.20) \times 10^{-9}$

Considering that the total area of one ICARUS module is 1400 m^2, we expect a rate of 5×10^6 neutrons per day traversing the boundaries of the detector. The reaction rate in the detector and the consequent background production will be evaluated by means of a dedicated Monte Carlo simulation. We give here some preliminary evaluations of attenuation of the incoming neutron flux produced by the stainless steel container walls and by the first layers of the argon itself. We will consider separately the thermal and the fast neutrons.

a) thermal neutrons.

The flux of thermal neutrons entering through the 1400 m^2 surface of the detector results in a total rate of 13 Hz. The attenuation length for thermal neutrons in stainless steel is 4.8 cm; the 11 cm thick wall will then capture at least 90% of the thermal neutrons, reducing their rate to 1 Hz. In liquid argon the 'diffusion length', the length over which the flux decreases to 1/e, is 23 cm; if we use a one metre thick outer argon layer as an absorber, this will attenuate the thermal neutron flux to 1.2%. We then expect a rate of less than 10^{-2} Hz in the detector volume inside a one metre layer of argon. Only a fraction of the photons from neutron capture will be directed towards the sensitive volume and they will be absorbed by a further 1.5 m long path.

b) fast neutrons.

Fast neutrons are also an indirect source of thermal neutrons, which in turn can be captured by argon nuclei. Fast neutron capture and inelastic scattering have not been considered. Under these hypotheses the neutron density d at depth x is given by:

$$d = D_0 \; e^{-\left(\frac{x^2}{4\tau}\right)}$$

where D_0 is the initial neutron density, x the distance from the source and τ is the so-called thermal neutron age. We obtain that the remaining thermalized component after one metre of liquid argon is negligible.

In conclusion we find that no more than 0.1% of the original thermal neutron flux survives after one metre of liquid argon. As a consequence, to be confirmed by accurate calculations and measurements, a central fiducial volume of 3.5 kton of the detector should be essentially background-free. In the worst hypothesis, even if all the remaining neutrons (1000/day) were absorbed inside the fiducial volume, no more than a few electrons per day would be produced above 5 MeV.

4.4.4 Muon-induced radioactivity

Long-lived radioactive isotopes are produced by the interaction of high energy cosmic muons with argon nuclei [12].

In the underground Gran Sasso Laboratory the muon flux $\Phi_\mu \sim 1\ m^{-2}\ h^{-1}$ [12] is due to the penetrating component of the cosmic muon flux ($E_\mu > 1.4$ TeV) and to atmospheric neutrino interactions in the rock surrounding the cavern.

These muons can produce:

(a) radioactive isotopes, from electromagnetic nuclear interactions with the detector materials (liquid argon and stainless steel). γ's and β's are thus eventually produced from radioactive decays;

(b) neutrons, from nuclear showers initiated by through-going muons inside the apparatus. Inelastic scattering of these neutrons with argon nuclei may produce in turn new radioactive isotopes. (Muon interactions in the rock surrounding the detector may produce neutrons and γs as well, but they have already been accounted for in the natural radioactivity measurement discussed above.)

Nuclei in excited states are directly produced through electromagnetic nuclear reactions by muons. Only the long-lived ($\tau_{1/2} >> 1$ s) isotopes (or their daughters) are sources of background. In fact, when the decay time is short, the decay products can be correlated in time with the recorded signal from the muon crossing the detector, and the event can easily be vetoed. The long-lived elements produced through the interaction of muons with ^{40}Ar are ^{39}Cl and ^{39}Ar with de-excitation energy respectively of 3.44 MeV and 0.57 MeV. Possible long-lived daughters from excited argon nuclei are ^{22}Na and ^{7}Be, with de-excitation energy respectively of 2.84 MeV and 0.48 MeV. We consider here the production of ^{39}Cl and ^{22}Na, where the decay energy is not negligible.

The number of electromagnetic nuclear reactions induced by muons on argon nuclei can be evaluated, taking into account the muon flux reaching the detector (Φ_μ), the number of targets (argon nuclei in the detector) and the production cross-section $\sigma(\mu + Ar \rightarrow A^* + X)$ for a given nuclide A^* in the final state.

Assuming an average muon energy of 200 GeV and a mean virtual photon energy of 20 MeV, absorbed by the nucleus in the μ + Ar electromagnetic interaction, we predict a production cross-section of 3.8 mb for ^{39}Cl and of 7.6 μb for ^{22}Na. Thus, the estimated rate is of the order of ~ 700 ^{39}Cl nuclides produced per day in a 5 kton ICARUS module, while the ^{22}Na production rate is negligible (about 1 per day). The half-life of ^{39}Cl is quite short (55.6 mn), leaving only ~ 40 radioactive nuclei at equilibrium. Most of the ^{39}Cl nuclei decay to the ground state through β^- or γ emission.

The mean number of neutrons induced by cosmic-ray muons in the underground Gran Sasso Laboratory has been extrapolated from a measurement performed in the Mont Blanc underground laboratory [12], scaling to the mean muon energy ($<E_\mu>$ = 200 GeV) at Gran Sasso:

$$< N_{neutrons} >= 32 / \frac{muon}{m^2} \ / kton$$

With the muon flux (Φ_μ) given above, we obtain a rate of about 4000 neutrons per day in one ICARUS module. These neutrons are promptly produced by the crossing muons and the background electrons generated can be rejected by requiring a coincidence with the parent muon in a time interval of a few hundred microseconds.

4.5 Conclusions

With a 5 MeV threshold on the kinetic energy of the scattered or inverse β-decay electrons, a 4.7 kton ICARUS detector will record about 4200 elastic scattering events and about 3800 absorption events per year, if the Standard Solar Model calculations are valid.

For the elastic scattering reaction the background electrons can be efficiently removed by requiring that the angle between the electron direction and the sun be less than 25°. Under these conditions, the number of events reduces to 2730 while the background rate is reduced by a factor of 10.

Absorption events are distinguished from the background by requiring one inverse β-decay electron ($E_e > 5$ MeV) accompanied by energy deposition larger than 2 MeV (from a number of Compton electrons) in a spherical fiducial volume of 50 cm radius. The corresponding efficiency is estimated to be about 80% giving a rate of 3000 events/year.

The measurement of both the elastic scattering and the absorption reactions allows the performance of a solar-model-independent test of the neutrino oscillation mechanism. In the hypothesis of 5460 elastic scattering and 6000 absorption events in two years and for one module, the estimated statistical error on the ratio R of elastic to absorption events is of the order of 1.9%. As a result we will be sensitive to all the currently interesting area of the $\nu_\mu \leftrightarrow \nu_e$ oscillation parameter plane ($\sin^2 2\theta$, Δm^2).

With the direct observation of solar neutrinos, in two years of data taking, ICARUS should be able to tell whether the apparent neutrino deficit is confirmed and if it is, whether it is due to neutrino oscillations or to a deficient solar model. Let us note again here that the solar neutrino issue is addressed in two independent ways in ICARUS, indirectly by using atmospheric neutrinos and directly by observing solar neutrinos. This is a truly unique feature of our experiment.

4.6 References

[1] S.P. Mikheyev and A.Y. Smirnov, Nuovo Cim. **9C** (1986) 17; L. Wolfenstein Phys. Rev. **D20** (1979) 2634.

[2] Y. Suzuki, Kamiokande Results, Proc. Int. Symp. on Neutrino Astrophysics, Takayama, Japan, 1992; R. Davis Jr., BNL-508-79, The Status and Future of Solar Neutrino Research, 1 (1978), ed. G. Friedlander; R. Davis Jr., Workshop on Neutrino Telescopes, ed. M. Baldo-Ceolin, Palazzo Loredan, Venice, Feb. 1990, pp. 1–13; P. Anselbaum et al., Phys. Lett. **B285** (1992) 376 and 390; M. Spiro, Proc. Int. Europhys. Conf. on High Energy Physics, Marseille, 1993; V.N. Gavrin, Int. Conf. on High Energy Physics, Singapore, 1990, Vol. 1, p. 693; Phys. Rev. Lett. **67** (1991) 3332; Int. Conf. on High Energy Physics, Dallas, Texas, USA (1992); T. Bowles, Moriond Conf., Villars, Switzerland, Jan.-Feb. 1993.

[3] J.N. Bahcall, M. Baldo-Ceolin, D.B. Cline and C. Rubbia, Phys. Lett. B **178** (1986) 324; CERN – Harvard – Milano – Padova – Roma – Tokyo – Wisconsin Collaboration, internal report INFN/AE – 85/7 Frascati (1985); ICARUS Collaboration, ICARUS I: An optimized, real time detector of solar neutrinos, internal report LNF–89/005(R), February 1989.

[4] J.N. Bahcall, *Neutrino Astrophysics*, Cambridge Univ. Press (1989); Particle Data Group, Review *of Particle Properties*, Phys. Rev. **D45** (1992) III. 60–61.

[5] W.E. Ormand, P.M. Pizzochero, P.F. Bortignon and R.A. Broglia, June 1993, private communication; W.E. Ormand, P.M. Pizzochero, P.F. Bortignon and R.A. Broglia, *The Solar Neutrino Capture Cross-Section for* ^{23}Na, NTG/INFN–92 Prep.

[6] R. Brun, F. Bruyant, M. Maire, A.C. McPherson and P. Zanarini, GEANT 3, CERN report Data Handling Division, DD/EE/84–1, September 1987.

[7] P. Petranzan, Una Possibile Soluzione al Puzzle dei Neutrini Solari, Ph. D. Thesis, University of Padova, 1986, unpublished.

[8] C. Arpesella et al., Search for ^{42}Ar with a germanium detector at the Gran Sasso Laboratory, LNGS 92–27, April 1992.

[9] A. Cesana and M. Terrani, *On atmospheric* ^{39}Ar *and* ^{42}Ar *production*, private communication, June 1993.

[10] C. Arpesella, S. Latorre and P.P. Sverzellati, *A low background counting facility at Laboratori Nazionali del Gran Sasso*, Internal Report LNGS 92/35 (1992).

[11] P. Belli et al., Il Nuovo Cimento **101A** (1989) 959.

[12] J.S. O'Connel and F.J. Schima, Phys. Rev. **D38** (1988) 2277.

5. Astrophysical and cosmological studies

5.1 Detection prospects for a supernova collapse

5.1.1 Characteristics of a supernova collapse

For the first few seconds, the gravitational core collapse of a single star emits an intense burst of neutrinos whose luminosity rivals the total optical emissions of the observable universe. The detection of 19 $\bar{\nu}_e$ events from SN1987A most economically constrained the properties of neutrino mixing, neutrino masses, neutrino magnetic moments, neutrino decay, etc., as well as providing confirmation of the gross features of the previously untested theory of stellar collapse [1]. Those 19 events, however, could not identify any of those dynamical characteristics of the supernova mechanism that are stamped upon its neutrino signatures: shock breakout, convection, accretion, explosion, core cooling, and transparency. Nor was it possible that any ν_μ or ν_τ events be detected, despite the prediction that these neutrino species and their antiparticles carry away the bulk of the neutron star binding energy. On the other hand, the new dedicated experiment, LVD, will soon take data at the Gran Sasso Laboratory; the collection of hundreds to thousands of events is anticipated by the dedicated LVD experiment and by the new generation of neutrino detectors for the next supernova burst. Such collective information will resolve many of the outstanding questions in supernova modelling, as well as measure or constrain the properties of all three generations of neutrinos more tightly than can now be done in a laboratory. The contribution of the ICARUS detector, in particular, can provide pieces of the puzzle not duplicated by other experiments.

In order to examine the response of ICARUS to a supernova collapse in our Local Group of galaxies, we employ here a generic but detailed model of neutrino emission that reflects the latest calculations in Type II supernova theory. This baseline model of luminosities and spectra for each of the neutrino species incorporates various generic features of the dynamics of stellar collapse, but is not tied to any particular model. This patchwork model has been presented in Ref. [2] specifically for the purpose of studying and comparing the response and sensitivity of various neutrino detectors. In Figure 1a we reproduce from Ref. [2] the structure of the ν_e, $\bar{\nu}_e$, and 'ν_μ' luminosity curves for the first second of emission, where 'ν_μ' denotes the muon and tau neutrinos and their antiparticles collectively; Figure 1b shows the same for the first 50 seconds. In Figure 2a we reproduce the ν_e, $\bar{\nu}_e$, and 'ν_μ' average energy spectra as a function of time for the first second, and in Figure 2b for the first 50 seconds. The total energy radiated by this model is 2.9×10^{53} erg, of which 5.87×10^{52} erg are radiated in the form of ν_e's, 5.18×10^{52} erg in $\bar{\nu}_e$'s, and 1.79×10^{53} erg in 'ν_μ''s. The integrated average energies are 9.9 MeV, 11.6 MeV, and 15.4 MeV, respectively.

5.1.2 The neutrino signal

From Figures 1 and 2 it is clear that the neutrino emissions are rich in diagnostic features of core collapse dynamics and neutron star formation. Here we list some of the main features only, for the purpose of their identification in the detected neutrino signals. Details may be found in the

abundant literature; see, for example, Refs. [3–6]. In Figure 1a the ν_e ramp at times less than zero is indicative of the accelerating rate of electron capture in the collapsing core. The rebound of the inner core into the supersonic outer core creates a strong shock wave (t = 0), accompanied by the ν_e neutronization burst (the spike of Figure 1a), and the sudden turn-on of the $\bar{\nu}_e$ and 'ν_μ' radiation.

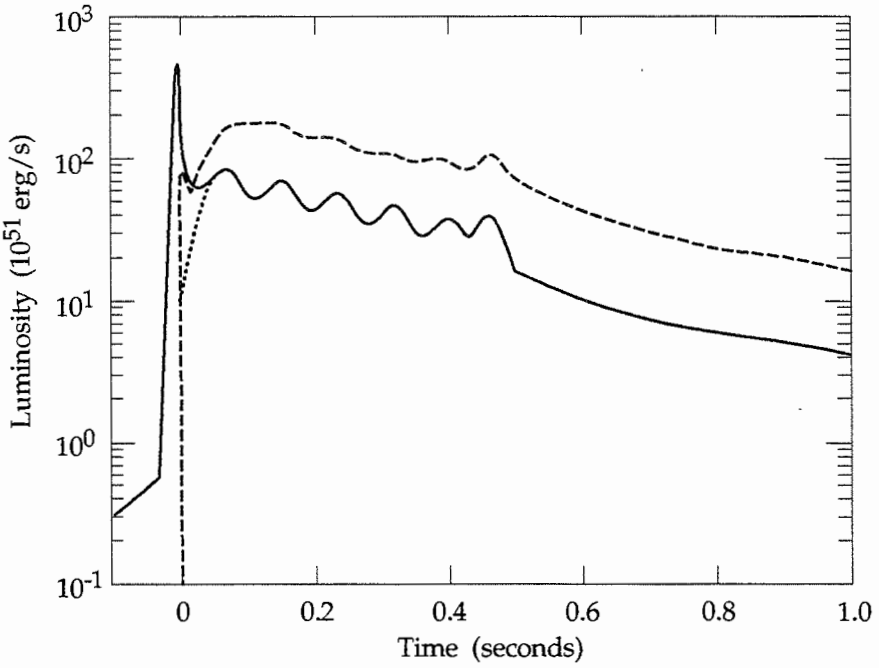

Figure 1a : Luminosity curves for ν_e (solid), $\bar{\nu}_e$ (dots), and 'ν_μ' (dashes) for the first second of emission

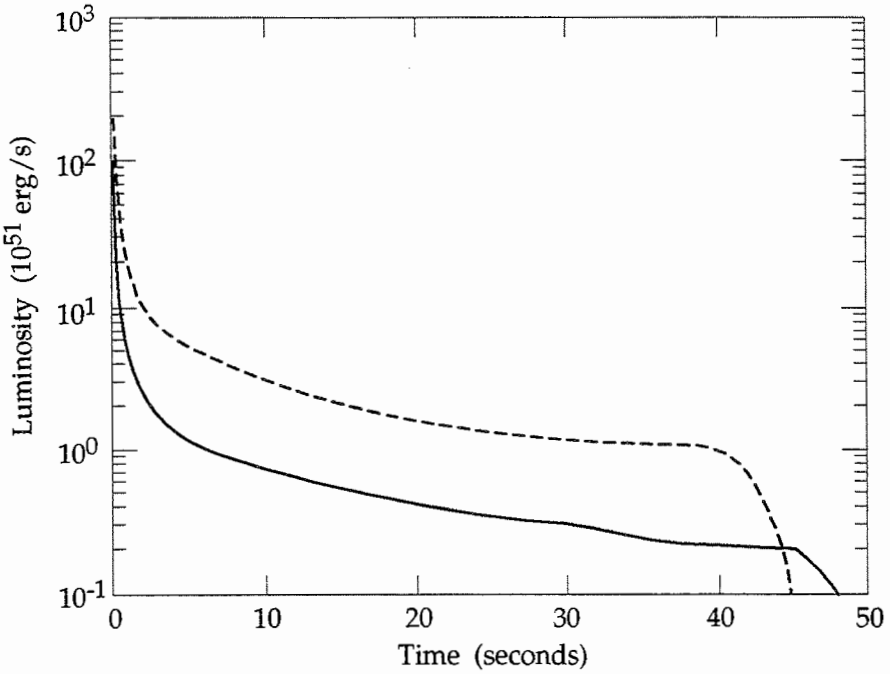

Figure 1b : Luminosity curves for ν_e,$\bar{\nu}_e$ (solid) and 'ν_μ' (dashes) for the first 50 seconds of emission

Immediately after the burst, the ν_e spectrum makes a sudden transition to a more thermal distribution (see Figure 2a), with an average energy of about 10 MeV. The $\bar{\nu}_e$ spectrum is harder, with an average energy of 13 MeV. Since the muon and tau neutrinos and their antiparticles interact at these temperatures only via neutral current interactions, their neutrinosphere lies somewhat deeper within the core. Their spectra is therefore hotter than either the ν_e or $\bar{\nu}_e$ spectra, about 16 MeV. Within 20 ms of bounce, hydrostatic equilibrium is achieved and a protoneutron star is formed; the ν_e and $\bar{\nu}_e$ luminosities now merge. At this stage the protoneutron star is fattened by accretion of the outer core matter. Either the shock wave continues into the outer stellar envelope or it stalls, only to be revived within hundreds of milliseconds or seconds by neutrinos from the core; these are the so-called prompt and delayed mechanisms, respectively, of core collapse. In this patchwork model, the bounce shock fizzles into an accretion shock, and subsequent neutrino heating of the shocked envelope reenergizes the shock into a supernova at 450 ms.

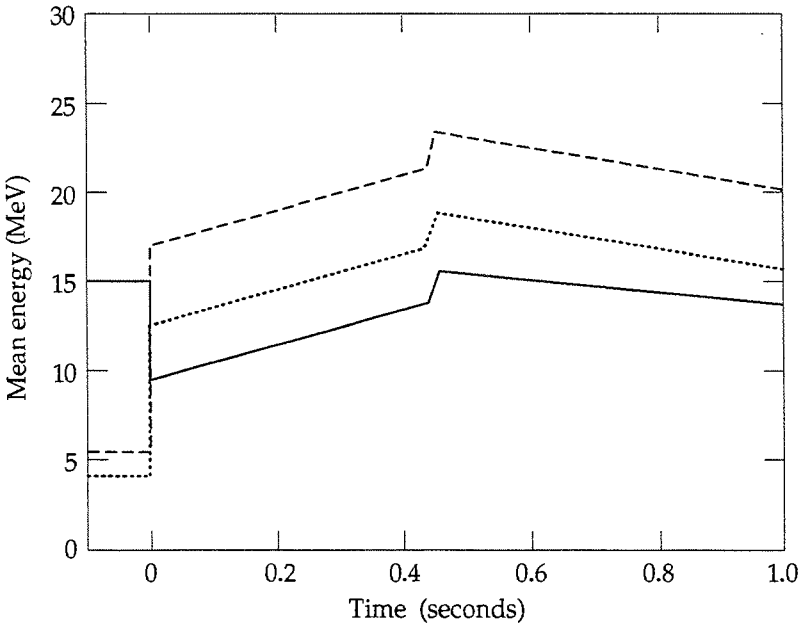

Figure 2a : Average energy for ν_e (solid), $\bar{\nu}_e$ (dots), and 'ν_μ' (dashes) for the first second

Oscillations in the mass accretion rate modulate the neutrino luminosities, as indicated in Figure 1a, between 30 and 420 ms. At 450 ms the explosion which causes the ejection of the outer envelope and the optical supernova display occurs. Accretion shock may delay the explosion by 0.5 seconds to some several seconds; its inclusion here serves to display a possible structure of neutrino emission, rather than being a necessary prediction of the Standard Model. Quick spectral hardening, on the other hand, is predicted to accompany explosion (see Figure 2a) whether it is prompt or delayed. While the first 100 ms are rich in diagnostic structure, the protoneutron star then begins a long cooling phase which may account for most of the energy emitted. During cooling the neutrino luminosities decay smoothly according to power laws which reflect the nonlinearity of neutrino transport. The long duration is a consequence of the high densities and high neutrino energies, which imply high opacities in the protoneutron star

interior. It is expected that the thousands of events detected from such a collapse be spread over many tens of seconds to a minute or more, but that as the neutrino energies soften a larger fraction of the emitted luminosity will be shunted below detector thresholds. Finally, the cooling phase ends when the core becomes transparent to neutrinos and the luminosities plummet (t = 46 and 42 s in the model used here for ν_e ($\bar{\nu}_e$) and 'ν_μ' respectively). Again, since the 'ν_μ' opacities are lower than the ν_e and $\bar{\nu}_e$ opacities, it is predicted that the 'ν_μ' emissions should fall off first.

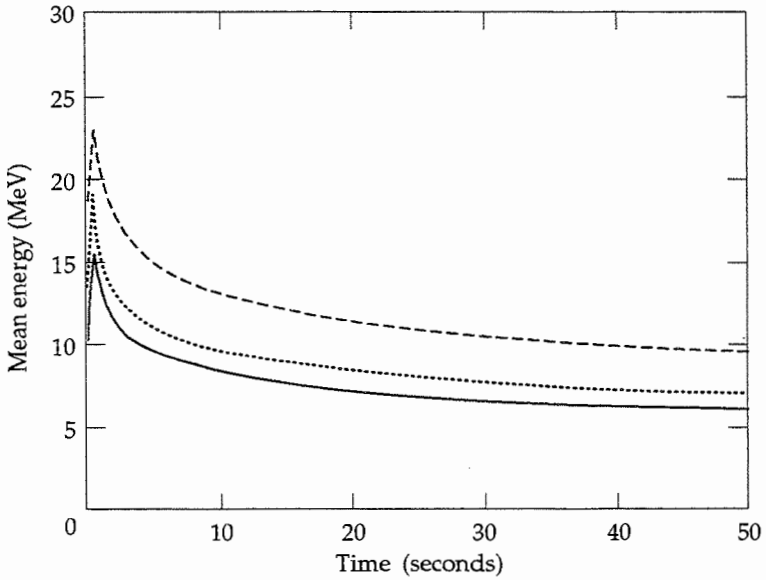

Figure 2b : Same as Figure 2a above for the first 50 seconds of emission

5.1.3 Event rate in the ICARUS detector

We assume the supernova occurs at 10 kpc, a distance which includes 53% of the stars in the galactic disk [7]. (All stars in the Milky Way lie within 30 kpc of the Earth.) For a supernova event at that distance, one would decrease the 10 kpc fluence at the Earth (which behaves as $1/r^2$), and hence the event rates, by a factor of 9 (Figure 3). To calculate the theoretical count rates for this particular supernova in the ICARUS detector, we convolute the luminosities of the various ν species as a function of time (Figure 1) with the neutrino scattering and absorption cross-sections on liquid argon, shown in Figure 4 as a function of energy, and with the average energy spectra as a function of time (Figure 2). The electron recoil threshold energy of 5 MeV is taken into account in the calculation of the scattering cross-sections, whereas for the absorption cross-section a threshold energy of 11 MeV is used. While the neutrino energy spectrum is predicted to be described by a thermal distribution, we have checked that using the mean energy instead does not introduce any appreciable error. The event rates are based on exposure to 5 kton of liquid argon and assume 100% efficiency; the resulting count rates as a function of time are displayed in Figure 5a for the first second and in Figure 5b for the first 50 seconds.

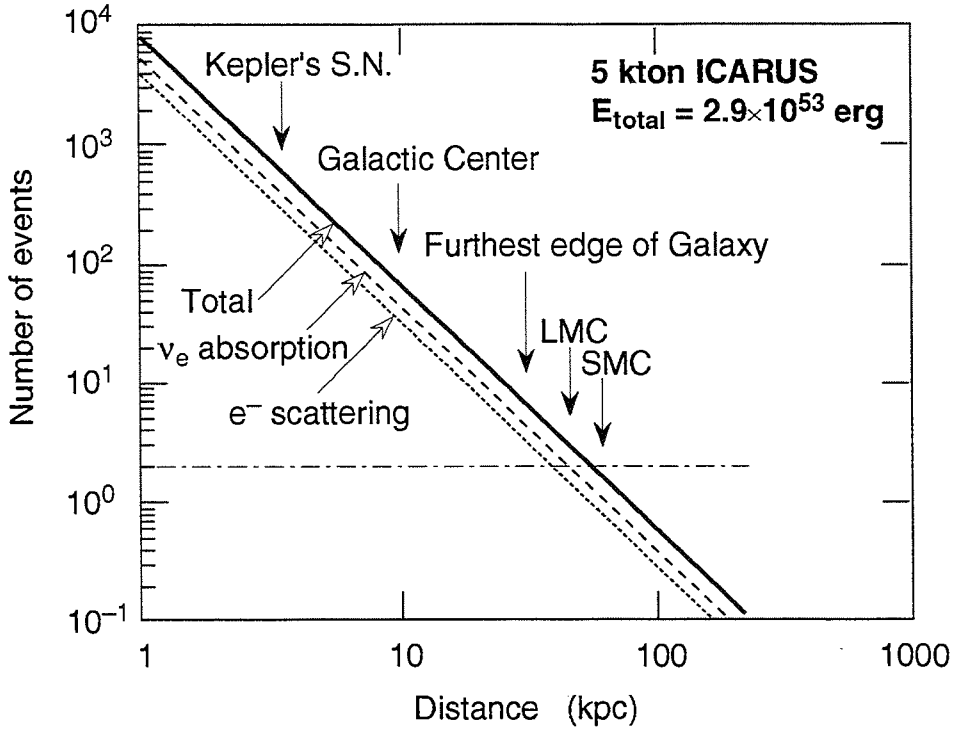

Figure 3: Predicted number of events in one ICARUS module, as a function of supernova distance, based on the supernova model as described in the text. Six species of neutrinos contribute to the electron scattering events. The horizontal dashed-dotted line shows the reach of ICARUS if a coincindence of two events is required.

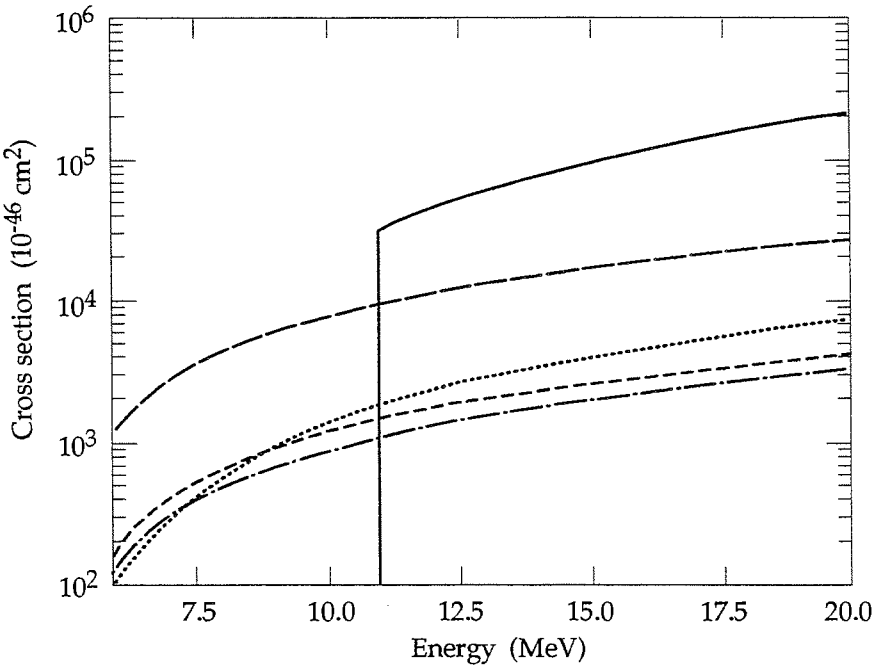

Figure 4 : Cross-sections, including thresholds, as a function of neutrino energy for ν_e absorption (solid), ν_e scattering (long dashes), $\bar{\nu}_e$ scattering (dots), ν_μ, τ scattering (short dashes), and $\bar{\nu}_\mu$, τ scattering (short-long dashes).

The total number of events is integrated to be 76 (44 from ν_e absorption on liquid argon, and 32 from electron scattering by all six species of neutrinos). Of these 76 events, 56 (37 absorption and 19 scattering), or 73%, are expected to take place in the first second. The rich event yield of the first second allows many of the characteristics of the supernova mechanism to stand out clearly: the ν_e neutronization burst, the rapid turn-on of the $\bar{\nu}_e$ and 'ν_μ' radiation, the accretion shock oscillations, the explosion pulse, and the long cooling of the core. The ν_e burst is of particular interest and the sensitivity of ICARUS to this feature is paralleled only by LVD and SNO; the light-water detectors, such as IMB and Kamiokande II, do not have sufficient ν_e sensitivity to detect it. The count rate peaks at 1200 Hz (but lasts only about 20 ms). We therefore expect 9 absorption and 2 scattering events in the ν_e neutronization burst for this supernova collapse. While special triggering will be necessary for readout of such a fast event rate, no problems are expected with data acquisition as ICARUS has effectively no dead time. Accretion shock modulation of the ν_e luminosity, depending on its amplitude and period of oscillation, may also be discernible by bunching, or pulses of about 5 events. The explosion peak should be easily detected, as well as the gradual drop in count rate, on account of ICARUS's low energy threshold.

The overall electron scattering rate in ICARUS, when compared with the event rate of ν_e absorption, will provide one of the first direct confirmations of the existence of the ν_μ and ν_τ components in the supernova emission. The light-water neutrino detectors, on the other hand, are largely insensitive to these neutrino species. Another advantage of the neutral-current sensitivity of ICARUS is the fact that the forward-peaked electron scattering events will point back to the direction of the supernova, thus providing confirmation of their origin.

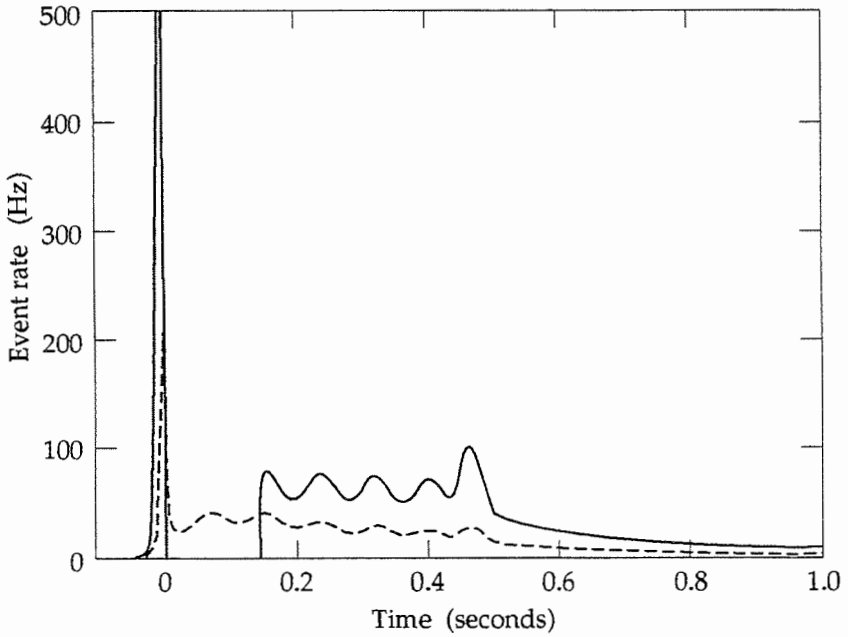

Figure 5a : Even rate for neutrino absorption channel (solid) and scattering (dashes) as a function of time for the first second. Spike at t = 0 peaks at 1200 Hz.

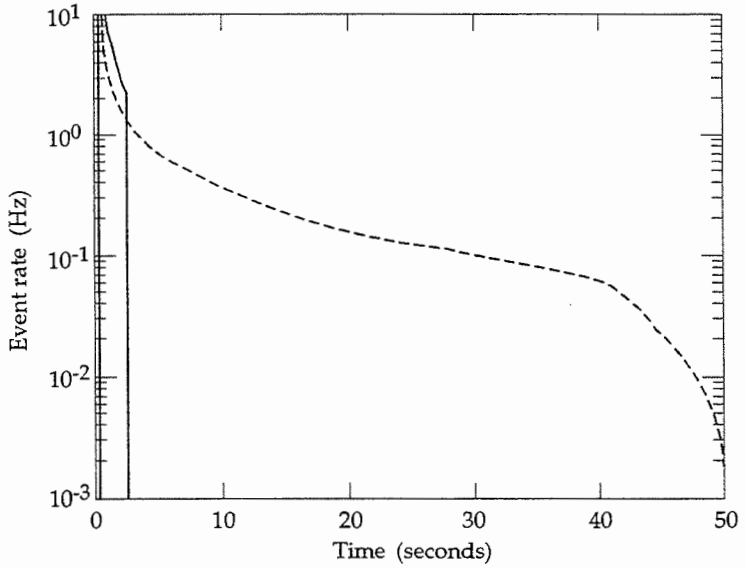

Figure 5b : Same as Figure 5a above for the first 50 seconds

The time structure of the luminosity of the next detected stellar collapse, and the absence or presence of structure within it, will yield a wealth of information on the explosion mechanism as well as on neutrino properties. ICARUS may contribute nearly a hundred events to the thousands that will be collected by the international effort. ICARUS's neutral-current sensitivity will render a part of its contribution complementary to those of other detectors. On account of the good energy and angle resolution of the detector, its accurate timing, and effectively zero dead time, these events will be rich in information on the energy, timing, angle, and flavour content of the explosion. Of particular consequence is the fact that ICARUS can be expected to be sensitive to the initial ν_e neutronization burst, important for the study of effects of a finite neutrino mass, as well as the ν_μ and ν_τ components in the supernova emission.

If we consider that two events in coincidence are sufficient to detect the occurence of a supernova, Figure 3 shows that the sensitivity of ICARUS extends to the entire Milky Way galaxy and includes the Large Magellanic Cloud. About one event is expected from a supernova in the Small Magellanic Cloud.

5.1.4 The tau-neutrino mass

The observation of neutrinos from a supernova allows us also to study the nature of neutrinos. In the case of SN1987A Spergel and Bahcall [8], analysing the neutrino events observed by Kamiokande II and IMB, concluded that $m_{\nu e} \leq 16$ eV while the best limit to date is $m_{\nu e} < 7.2$ eV. With the larger event statistics and the more accurate measurement which ICARUS can perform, it is possible to obtain interesting information on the ν_τ mass for which the present limit, recently improved by the Beijing electron–positron collider measurement, is still fairly high at 31 MeV. The detection of a finite ν_μ or ν_τ mass differs from that of the ν_e in that there is no predicted sharp burst of these species on which mass effects may produce their telltale signature. The distribution of the ν_μ and ν_τ events in time is broad (Figure 5) and they

are few in number (of the 32 electron scattering events predicted at 10 kpc, only 5 are expected to be due to ν_τ or $\bar{\nu}_\tau$). Although subject to the usual broadening, flattening, and smearing effects due to a finite ν_τ mass, for example, such effects would probably go unnoticed in so small an event sample. Moreover, ICARUS provides no direct way of distinguishing among the various neutrino species in the electron scattering channel. An indirect method could make use of the ν_e component from the absorption process.

If, however, the time-of-flight difference for the massive neutrino with respect to a massless one is of the order of or greater than the duration time of the supernova emission, then separation of the massive neutrino events from the other species (assumed massless) is automatically achieved. The time-of-flight difference is given by:

$$\Delta t = \frac{d}{c}\left(1 - \frac{1}{\sqrt{1-\frac{m_\nu^2}{E_\nu^2}}}\right) \cong 0.5\ \mathrm{s}\left(\frac{d}{10\ \mathrm{kpc}}\right)\left(\frac{m_\nu}{10\ \mathrm{eV}}\right)^2\left(\frac{10\ \mathrm{MeV}}{E_\nu}\right)^2$$

where d is the distance to the supernova, E_ν is the neutrino energy, and m_ν the mass. For an average ν_τ energy of 15 MeV, the above expression may be rewritten in the following way:

$$m_\nu = 150\ \mathrm{eV}\left(\frac{10\ \mathrm{kpc}}{d}\right)^{1/2}\left(\frac{\Delta t}{50\ \mathrm{s}}\right)^{1/2}.$$

For ν_τ masses greater than 150 eV, the ν_τ events are sufficiently separated from all the others, allowing ICARUS to set an upper bound (Note that while the upper mass limit sensitivity becomes greater with increasing distance, the total number of ν_τ events, of course, decreases as $1/d^2$). Hence for a supernova collapse at a distance of 10 kpc, it would be possible for ICARUS to set an upper limit on the mass of the ν_τ down to 150 eV, a spectacular progress compared to the present 31 MeV limit. We also point out that, given the supernova direction, ICARUS can determine the incident ν_τ energy for each event. Then, should the gap of time separating the ν_τ events from the massless neutrino events become large with respect to the time duration of the supernova burst, so that the differences in emission times may be neglected, ICARUS can not only set a ν_τ mass limit, but can use each ν_τ event to make a precise determination of the ν_τ mass. For very large ν_τ masses, however, we expect their supernova emission characteristics (number, energy, and luminosity curve) to differ greatly from those predicted here in the massless case.

A more refined analysis is needed, making use of both elastic and absorption channels, to possibly improve further the sensitivity of ICARUS and reach the mass region favoured by mixed dark-matter models where the ν_τ would contribute significantly to the closure of the universe.

5.2 Detection prospects for relic supernovae neutrinos

5.2.1 Origin of the relic supernova flux

A diffuse isotropic background of neutrinos from past supernovae is believed to exist, and to consist of ν's and $\bar{\nu}$'s in approximately equal proportions. While neither the flux nor the energy spectrum can be predicted with any certainty, the observation of such neutrinos is of great astrophysical importance and would yield valuable insight into the early evolution of the universe, the definition of the epoch of galaxy formation, as well as the rate of supernova occurrences now and in the early universe. Moreover, from the experimental point of view, the predicted mean energy of the relic supernovae spectrum lies tantalizingly in a narrow window just above the background of terrestrial antineutrinos and just below those of atmospheric origin (Figure 6).

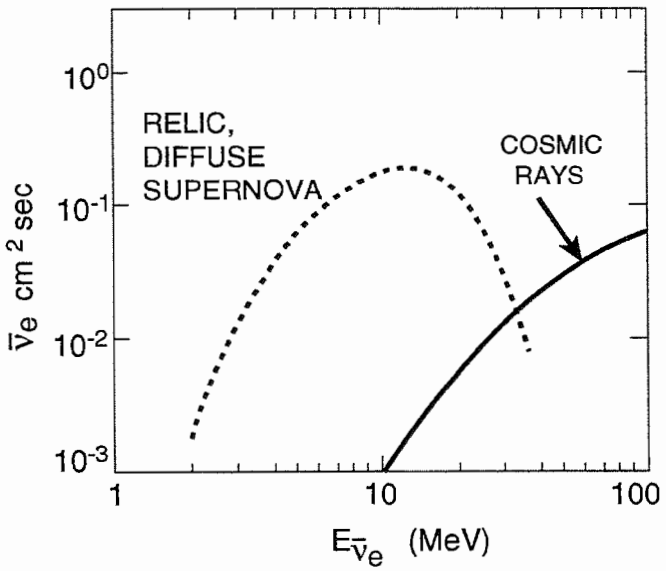

Figure 6 : The relic neutrino energy window. The dotted line is only a qualitative indication of the expected shape of relic neutrinos, however, the normalization is arbitrary.

5.2.2 Theoretical estimates of the relic supernova flux

Depending on the specific assumptions one makes, quite different values of the integrated flux are obtained. One may start with the fact that Type II supernovae are the only known source in the universe of copious numbers of neutrinos, and that Type II supernovae are found exclusively in spiral and irregular galaxies. Then one method of evaluating the present neutrino flux at Earth is to assume a constant rate of Type II supernova occurrence per unit galactic luminosity (based on the estimated rate in the present universe). One then sums over all such galaxies in the observable universe. Both the energy E(t) of the neutrino emitted at time t, as well as the duration of the neutrino burst $\tau(t)$, must be appropriately redshifted to obtain the luminosity at Earth at the present time. One such estimate [5] based on the luminosity density of spiral galaxies gives a flux $\phi_{\bar{\nu}_e} \sim 1.0$ cm^{-2} s^{-1}. An analogous method is to assume instead a constant rate of Type II supernovae

per unit galactic mass [9], again based on the current frequency, which implies a flux $\phi_{\bar{\nu}_e} \sim 16\ cm^{-2}\ s^{-1}$.

Now the mean neutrino energy resulting from the cooling of a Type II supernova to a neutron star depends only on the initial iron core mass [4]; predictions for the energy spectrum itself are model-dependent. For ν_e and $\bar{\nu}_e$ this mean energy is typically 10–16 MeV; all other species of neutrinos have a slightly greater average energy. Expansion of the universe will, however, broaden and degrade the energy spectrum. This has been studied in detail [10] for various cosmological models with the conclusion that the net effect of expansion is to degrade the mean neutrino energy by a factor of 1/2 (for $\Omega = 0$) to 3/5 (for $\Omega = 1$). The predicted mean ν_e and $\bar{\nu}_e$ energy for the relic supernovae signal is therefore 6–10 MeV.

The above method for estimating the relic supernovae flux is clearly limited by the current low rate of massive star formation and collapse; this rate may have been larger when the universe was young and the galaxies were just forming. An alternative method, but one with greater uncertainty, is to estimate the total number of stellar collapses that have ever occurred in the universe and to assume that all collapses of stars above a critical mass will produce the ν and $\bar{\nu}$ energy spectrum characteristic of a Type II supernova. A large fraction of this neutrino luminosity will then result from stellar collapses from around the time of galaxy formation. This method, its merits, and its drawbacks, has been discussed in detail in Ref. [5]. By assuming a critical mass of 8 solar masses, these authors calculate the time-integrated number density of such collapses (for Hubble constant $H_0 = 55\ km\ s^{-1}\ Mpc^{-1}$ and Ω_b, the ratio of the baryon density in the universe to its closure value, equal to 0.1), which yields $\phi_{\bar{\nu}_e} \sim 250\ cm^{-2}s^{-1}$. While the fact that the rate of massive star collapses may have been much greater in the early universe than at the present time serves to increase the estimate of the flux in this case, on the other hand, the redshift factor appropriate to the epoch of galaxy formation is highly uncertain, but certainly much larger than those factors used for the method of constant galactic rate discussed above. In particular, the mean neutrino energy could be degraded by a factor of 1/4 or more, in which case a large fraction of the flux would become invisible against the background of terrestrial neutrinos (i.e., below 3 MeV [9]).

5.2.3 Event rate in the ICARUS detector

For the purpose of evaluating the feasibility of detecting these relic supernovae neutrinos in the ICARUS detector, one may adopt the most optimistic value within the range of reasonable fluxes, but is nevertheless forced to conclude that the prospect seems unlikely. By assuming a flux of $250\ cm^{-2}\ s^{-1}$ for each of the six species of neutrinos, all of energy 9 MeV, one obtains a total of only 0.6 electron scattering events in liquid argon based on an exposure of 5 kton $\times$ year. This estimate includes the effect of a recoil electron threshold energy of 5 MeV, but no efficiencies. Owing to the lack of free nucleons in liquid argon, the estimated number of nuclear absorption events is only about 0.8 per year, but the inclusion of the detection threshold at 11 MeV for this channel reduces this number to zero.

Furthermore, by assuming that ICARUS is sensitive to the minimum detectable number of relic supernovae events in five years' running time, we

may estimate the best possible 90% C.L. upper limit on the flux which the 5 kton ICARUS may set. For six species of neutrinos, each of 9 MeV, contributing to 2.3 electron scattering events per year, one obtains a total flux limit of $\phi_{\nu\bar{\nu}} < 10^3$ cm^{-2} s^{-1}. Of course, taking into account realistic detector efficiencies and background considerations will serve only to increase the value of this upper limit. As it is, this estimate implies an electron antineutrino flux ($\phi_{\bar{\nu}_e} < 190$ cm^{-2} s^{-1}) to be compared to the recently published Kamiokande II result [11]: $\phi_{\bar{\nu}_e} < 580$ cm^{-2} s^{-1} at 90% C.L. for $E_{\bar{\nu}_e} = 9$ MeV.

For future reference, we note here that subsequent developments in particle physics and astrophysics may alter these conclusions, given the rather large uncertainties on supernova models. For example, in these estimates of the relic supernovae flux, consideration has been limited to Type II supernovae, whereas it has been speculated [5] that gravitational collapse events associated with black hole formation may also be copious producers of neutrinos. In the collapse of supermassive stars directly to black holes, a substantial fraction of the rest mass energy of the star may be emitted in the form of neutrinos, with or without the ejection of the star's outer envelope that results in a visible supernova. Woosley, Wilson, and Mayle predict, however, that the emitted neutrino energy spectrum may be somewhat softer than that of the typical Type II supernova, and moreover, that such collapses are probably associated with very large redshift factors.

Clearly the experimentalist's conclusion is to explore as carefully as possible the neutrino energy window just below the atmospheric neutrinos whose flux will be measured with improved precision by ICARUS. This is an area where surprises are possible.

5.3 References

[1] For a review, see J. N. Bahcall, *Neutrino Astrophysics* (Cambridge University Press, Cambridge, 1989).

[2] A. Burrows, D. Klein, and R. Gandhi, Phys. Rev. **D45** (1992) 3361.

[3] A. Burrows, Ann. Rev. Nucl. Part. Sci. **40** (1990) 181.

[4] R. Mayle, J. R. Wilson, and D. N. Schramm, Ap. J. **318** (1987) 288.

[5] S. Woosley, J. Wilson, and R. Mayle, Ap. J. **302** (1986) 19.

[6] H. A. Bethe, Rev. Mod. Phys. **62** (1990) 801.

[7] J. N. Bahcall and R. M. Soneira, Ap. J. Supp. **44** (1980) 73.

[8] D.N. Spergel and J.N. Bahcall, Phys. Lett. **200B** (1988) 366.

[9] L. L. Krauss, S. L. Glashow, and D. N. Schramm, Nature **310** (1984) 191.

[10] G. S. Bisnovatyi-Kogan and Z. F. Seidov, Ann. NY Acad. Sci. **422** (1984) 319.

[11] K. S. Hirata, University of Tokyo Ph.D. thesis, ICRR Report 239–91–8 and M. Koshiba, Phys. Rep. **220** (1992) 229.

V. RESULTS FROM A THREE-TON PROTOTYPE

We reproduce in this chapter the paper 'A three-ton liquid argon time projection chamber' that reports on the construction and operation of the prototype detector. The paper has been published in Nuclear Instruments and Methods **A332** (1993) 395. We add at the end of the chapter some considerations on the μ^+/μ^- discrimination.

1. Introduction

The role of bubble chambers in elementary particle physics has been of fundamental importance due to their capability to give high-resolution, unbiased, three-dimensional images of ionizing events. Bubble chambers can accomplish simultaneously the two basic functions of target and detector, due to the high density of the liquid medium. This characteristic has been essential for a number of experiments. Electronic detectors, contrary to bubble chambers, can be triggered and read out at fast rates. They replaced the bubble chambers for this reason. Owing to the low density of the gaseous medium they employ, the target and detector functions must be separated. This separation is a drawback for a class of experiments looking for rare contained events, e.g. proton decay and neutrino interactions. The ideal detector for these applications would be a liquid detector with high spatial resolution and electronic readout (the electronic bubble chamber).

A precise proposal for the liquid argon time projection chamber (Liquid Argon-TPC) was made by C. Rubbia in 1977 [1]. The detector is continually sensitive, self-triggering, and able to provide three-dimensional images of any ionizing event like an electronic bubble chamber. Particle identification is available by measuring the ionization charge per unit length (proportional to dE/dx) and the range of the stopping particles. The detector is also a superb calorimeter of very fine granularity and high accuracy. The ICARUS Collaboration proposed [2] in 1985 a multi-kiloton liquid argon TPC to be run in the Gran Sasso Laboratory to search for rare underground phenomena ranging from proton decay to real-time solar neutrino observations, as well as neutrino oscillations and relic supernovae neutrinos.

A brief description of the operating principles of the liquid argon (or other cryogenic liquid) TPC follows. Simple techniques have been developed [3,4] to obtain liquid argon at a level of purification (<1 ppb of O_2 equivalent) such that free electrons, as those produced by an ionizing event, can drift over distances of several metres. Any ionizing event taking place in a volume of several cubic metres of ultrapure liquid argon, where a uniform electric field is applied, will produce ion–electron pairs. A fraction of them, depending on the field intensity and the density of ion pairs, will not recombine and will immediately start to drift parallel to the field in opposite directions. The motion of both the electrons and the ions induces a current on any electrode present in the volume or around it. The current intensity is proportional both to the flux of the electric field across the electrode due to the drifting charge and to the speed of the charge. The speed of the electrons is five orders of magnitude greater than that of the ions, therefore only electrons give an appreciable contribution to the induced current.

No amplification is present in the liquid medium near the wires. This has an advantage and a disadvantage. The disadvantage is that the ionization charge to be detected is extremely small. Typically, 8000 electrons per millimetre are produced by a minimum-ionizing particle and a large fraction of these recombines, especially at low field intensities. The problem can be solved with low-noise FETs that have been commercially available for the past few years. The advantage is that the drifting electrons can be used many times to induce signals on different wire planes. This allows a three-dimensional readout as proposed by E. Gatti et al. [5]. In practice the readout is performed with a chamber consisting of a number of parallel wire planes located at the end of the sensitive volume (assuming the drift direction pointing to the end). We call z the coordinate along the electric field with x and y the coordinates on the plane of the chamber. The absolute z coordinate is given by a measurement of the drift time, provided that the t=0 time and drift speed are known. The drifting electrons reach and cross in sequence the following wire planes: 1. a plane of wires running, e.g. in the y direction, functioning as the screening grid; 2. a plane of wires running again, e.g. in the y direction, located at a distance of some millimetres below the screening grid where its function is to measure the x coordinate; 3. a plane of wires running in the x direction, located at a distance of some millimetres below the previous plane; its function is to measure the y coordinate. The electric field intensities in the sensitive volume above the screen grid and in the gaps between the grids must be arranged to have a complete transparency of the grids.

The sequence of wire planes can continue if more coordinates are needed and the angles between wire directions can be chosen at will. For our prototype detectors we have chosen two orthogonal coordinates (x and y) as described above; we have chosen the wire pitch and the distance between the planes to be 2 mm to have the best possible spatial granularity. Our 3-D pixel (our 'bubble') is a 2 mm per side cube. The last grid need not be transparent; we use it to finally collect the drifting electrons.

An electron drifting in the sensitive volume above the screen grid does not give any current in the coordinate planes (in the case of perfect shielding). A positive induced current starts in the x coordinate plane when the electron crosses the screen grid, becomes negative when the electron crosses the coordinate plane, and ends when the electron crosses the y coordinate plane. We call the x coordinate plane the 'induction plane'. The current on the y coordinate plane has similar behaviour, with the exception that only the positive current is present; when the electrons reach the plane they fall on the wires. We call this plane the 'collection plane'. We integrate the current from each wire of the coordinate planes and sample the charge with flash ADCs at a frequency that provides several measurements for each pulse.

We built and operated in a 5 GeV pion beam a small liquid argon TPC to make preliminary tests of the basic technological points after having optimized the geometry of the chamber planes by computation of the field and simulation of the signals. The maximum drift distance was 24 cm; the chamber had a screening grid and a single coordinate plane with an 8×8 cm^2 area; the geometry is shown in Figure 1. The results have been published elsewhere [6–8]. Here we simply summarize the most important ones:

1. Ultrahigh purity liquid argon can be easily obtained using commercial Oxisorb [9] cartridges and molecular sieves along with high-vacuum components and procedures. Free-electron lifetimes in the range of several milliseconds were routinely obtained corresponding to potential drift distances of metres.

2. We obtained very neat images of ionizing events operating the single plane both in the induction mode and in the collection mode.

3. We observed the effect of the diffusion and of the field dependence of the free-electron yield and found them to be in agreement with theory.

4. We evaluated the energy resolution in the MeV region and found it to be very good (of some per cent), in agreement with the measurements of other groups [10]

5. We measured the spatial resolution in the drift coordinate to be 60 μm for 5 GeV tracks.

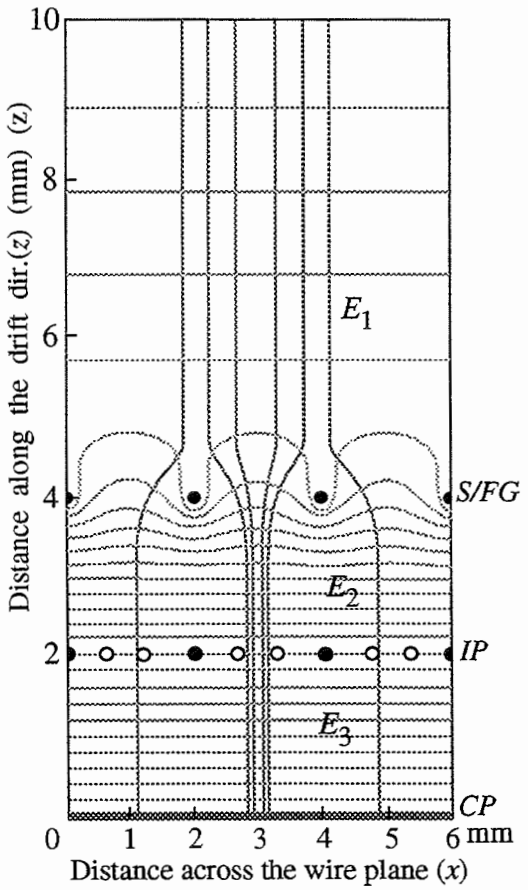

Figure 1 : The electric field map near the wire chambers. *S/FG* is the screening/focusing grid, *IP* and *CP* the induction and collection planes respectively. In the induction plane sense-wires are open circles, screen wires closed circles.

The ICARUS research programme is very complex and ambitious and cannot be realized in one step since it involves the introduction on a large scale of several innovative technologies. After obtaining the important results we have just mentioned, in 1989 we organized the ICARUS programme to follow a series of steps: 1) an initial phase of research and development, 2) the construction and operation of a detector of approximately 200 tons for solar neutrino studies [11] (ICARUS 1), and 3) the final multi-kiloton detector.

Step 1 is an intensive R&D programme based on a reasonable scale prototype detector aiming to solve the main technological problems:

a) The liquid argon must be kept ultrapure even in the presence of a large number of feedthroughs for the signals and the high voltage, and with wire chambers, cables, etc. in the clean volume. The contamination of electronegative molecules must be kept to around 0.1 ppb to allow drifts on long distances (metres) without capture of the ionization electrons;

b) All the materials employed in the construction of the detector must be extremely clean and non-degassing and the feedthroughs between pure argon and the outside world must be completely tight to avoid contamination due to leaks;

c) The wire chambers must be able to perform non-destructive readout with several wire planes with a few mm pitch; they must be built out of non-contaminating materials and must stand the thermal stress of going from room to liquid argon temperatures; the precision and the reliability of the mechanics must be high and a good knowledge of the electric field in the detector must be granted;

d) In order to obtain a good signal-to-noise ratio, low-noise preamplifiers must be developed. It must be remembered that we work with no amplification in the liquid; the signal is very small, of the order of 10 000 electrons for a minimum-ionizing track in a 2 mm wire pitch;

e) Given the large amount of digitizations of the three-dimensional image, software architectures and algorithms must be developed for data reduction.

To study these points, we decided to build a prototype detector with a sensitive mass of two tons (total argon mass is about three tons), corresponding to about 1/100 of that of the ICARUS 1 detector. In designing the different components of the prototype we had to be aware at all times that the technical solutions must be appropriate for the final detector.

The three-ton prototype detector has been taking data for one and a half years. We will describe here its main characteristics, its behaviour, and the principal conclusions we can draw from our experience. Preliminary results have been reported elsewhere [8,12], detailed discussions on the measurements performed with the detector will be reported in a subsequent paper.

The paper is organized as follows: in Sections 2–5 we describe the mechanics of the dewar, the electrodes and the wire chambers along with their respective cleaning procedures; in Section 6 the purification system and the purity monitor are described; in Section 7 we discuss the internal low-capacitance cables; in Section 8 the signal and the high-voltage feedthroughs; in Section 9 the analog and digital electronics; in Section 10 the readout organization and the filtering algorithms. We will then report some results of the operation of the detector and show examples of cosmic-ray events and of low-energy events induced by a radioactive source. Finally in Section 12 we will present our conclusions.

2. Mechanics of the dewar

The cryostat, shown schematically in Figure 2, consists of two coaxial vertical stainless steel (AISI 304L) vessels [13]. The shape of both the external (1 in Figure 2) and the internal (2) vessels is a cylinder with hemispherical bottoms. The two cylinders are connected by an annular flange (3 in Figure 2) on the top of the dewar. Another circular flange [14] (4) hermetically seals the inner volume of the dewar; this flange hosts the feedthroughs for the signal and the high-voltage (7) cables, and those for the argon circulation pipes and for all the necessary services (pressure metres, liquid argon level indicators, thermometers, etc.). The outer vessel has a diameter of 1.5 m, a height of 3.3 m and a wall thickness of 3 mm. The inner vessel has a diameter of 1.05 m, a height of 3.08 m and a wall thickness of 3 mm. The total internal volume is 2.61 m^3.

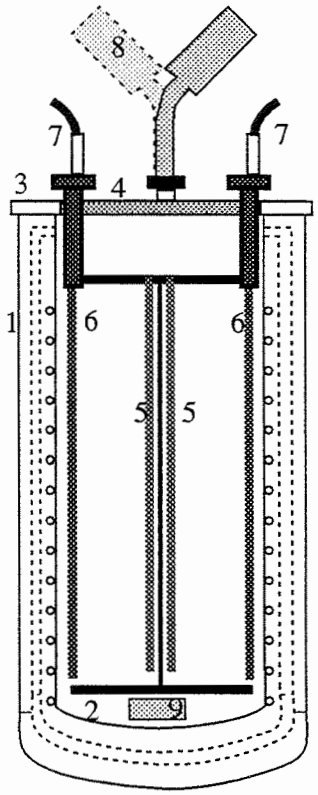

Figure 2 : Schematic view of the mechanics of the detector. 1 is the outer vessel, 2 the inner vessel, 3 the annular flange, 4 the circular flange, 5 the wire chambers, 6 the cathodes, 7 the high-voltage feedthroughs, 8 the boxes containing the preamplifiers (two out of eight shown), 9 the purity monitor.

The preamplifiers must be located as close as possible to the signal feedthroughs to reduce to a minimum the input capacitance, and hence the noise. They are hosted in eight cylindrical boxes (8) connected with tubes to the upper flange (only two out of eight are shown in Figure 2). The tubes are bent for lack of space. The boxes are refrigerated by Peltier valves at the optimum temperature. The signal feedthroughs are flushed with cold nitrogen gas to keep them in a dry environment to reduce the risk of discharges.

The evacuated volume (10^{-3} mbar obtained with a rotative pump) between the two vessels is filled with a superinsulator, consisting of two copper screens (shown dotted in Figure 2) surrounding completely the inner vessel, wrapped with several layers of aluminized Mylar sheets.

The cryogenic system of the detector has to perform four functions:

i) cool-down of the inner vessel before filling with pure liquid argon;

ii) continuous cooling of the liquid argon during operation of the chamber for extended periods of time;

iii) recirculation and continuous purification of a fraction of the argon to eliminate possible contamination;

iv) warm-up of the inner vessel before emptying the liquid argon.

The cryogenic system consists of the components illustrated in Figure 3. The liquid argon for cooling is supplied by a dump tank of 40 litres in volume (2 in Figure 3) situated above the cryostat. This tank can feed by gravity the copper serpentine surrounding the cryostat. An argon storage dewar fills the dump tank automatically three times per day. A level-indicator coupled with an electromagnetic valve controls the filling of the tank. Filling starts when the level falls below some preset value and stops automatically when the tank is full.

The consumption of cooling argon is 4–5 litres per hour when the inner vessel is full of pure liquid argon at 87 K. The cooling of the inner vessel can be performed by liquid argon circulating in a copper serpentine coiled around the vessel.

The ultrapure liquid argon in the dewar, even in absence of any leak, can be contaminated by outgassing of the walls and of the various materials (electrodes, chambers, spacers, cables, high-voltage resistors, etc.) contained in the dewar. In practice, as will be discussed below, the main outgassing sources are the parts of the system that are not in direct contact with the liquid and have, as a consequence, higher temperatures. The closing flange and the signal cables in particular have large surfaces in the clean volume at almost room temperature and are the main source of outgassing. To keep the liquid argon at the necessary purity we have provided a recirculation system. The naturally evaporating argon is brought through a pipe (3 in Figure 3) to a purification system (4 in Figure 3) similar to the main one that will be described in Section 6, but with two Oxisorb/Hydrosorb cartridges in parallel to decrease impedance. The argon is then recondensed in a serpentine (5) in the 40-l tank. The hydraulic circuit just described is ultraclean. As we will show, the recirculation system proved to be an essential part of the apparatus necessary to maintain the purity of the argon.

In case of failure of the cooling system, the liquid argon inside the cryostat will be vented through a rupture disc rated at about 2 bar absolute and eventually through the pumping system previously described.

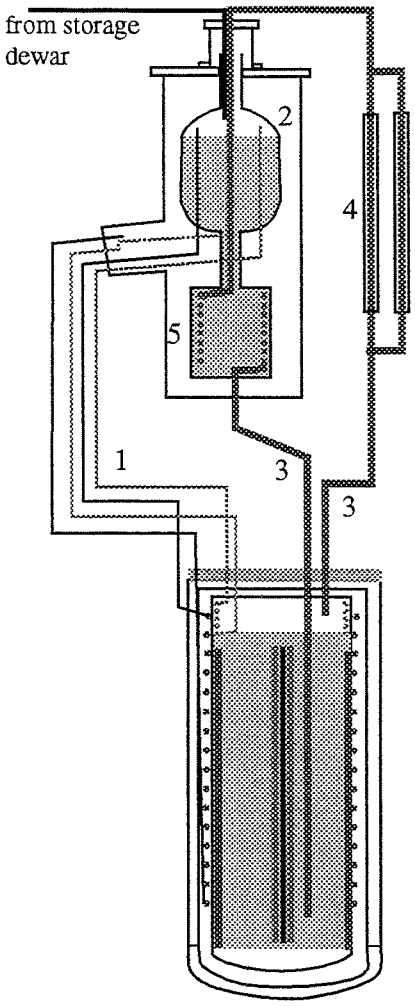

Figure 3 : The cryogenic system shown enlarged with respect to the dewar. 1 are the pipes used for cool down and continuous cooling, 2 is the 40-l dump tank, 3 are the pipes for ultrapure argon recirculation, 4 is the purification system, 5 the condensation system.

3. The configuration of the inner electrodes

Because this prototype should also be used to test the feasibility of the technological solutions to be adopted in ICARUS 1, the internal configuration of this dewar should follow very closely the one proposed for the 200-ton detector.

The inner volume of the dewar is split into two independent semi-cylindrical sections (each one a mirror image of the other) by means of a stainless steel septum placed vertically along a diameter of the dewar. This septum is held in position between two horizontal circular metal plates. These plates (one at the top and one at the bottom) and the central septum form a solid structure independent of the surrounding dewar in which we insert the elements of the detector. The structure is suspended from the upper flange by means of four rods. A small part at the top of the volume is excluded from this sectioning because it is needed as a service area to allow input/output for

the electronics and high voltage for the detector sections and to monitor the liquid argon level.

Both sections are equipped with identical drift chamber systems (5 in Figure 2). Each wire chamber covers a surface equal to 2.4×0.9 m^2 and is supported by frames on each side of the central septum. The drift volume is defined by the chamber itself, a system of 'racetracks' [14] consisting of 10 tubular rods of 2 cm in diameter (not shown in Figure 2) and a cathode. The racetrack rings are separated from each other by 5 cm; their distance from the wall of the dewar is at least 5 cm. The racetrack system is connected to the high-voltage power supply with each ring set at the appropriate voltage by means of a resistor chain. We use specially designed, thick-film resistors finished with glass. Values range between 50 and 100 MΩ.

The purpose of the racetrack system is to establish a well-defined and uniform electric field over the entire detection volume so that the electrons may be correctly and efficiently drifted onto the wire plane.

The cathode is a vertical metal plate (6 in Figure 2) 2 cm thick, 30 cm wide and 2.4 m high, at a negative voltage of 45 kV maximum. The distance between cathode and wire chamber is 42 cm (maximum drift distance). The maximum electric field in the drift volume is then 1 kV/cm. Figure 4 represents the electric field configuration in a horizontal cross-section of the dewar volume. The wire chambers, the racetracks and the cathodes are also shown.

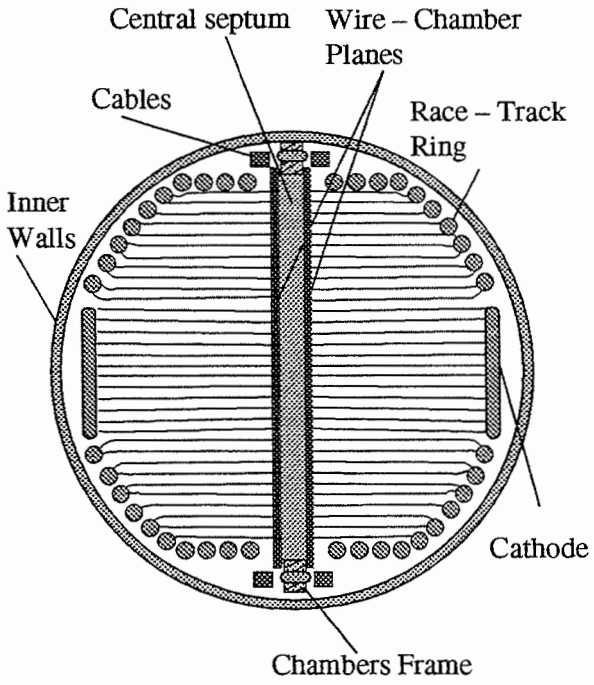

Figure 4 : Top view of the field lines in the drift region

The high-voltage power supply can deliver a maximum voltage of 150 kV, stable within 10^{-5}, and a maximum current of 0.5 mA. It is connected to the high-voltage cable through a 10 MΩ resistor that, associated with the cable capacitance (1.5 nF), is used as a filter. Under these conditions no additional noise due to the high-voltage ripple is observed at the sense-wires.

The total useful volume for signal detection is equal to 1.45 m^3 corresponding to 2 tons of liquid argon.

4. Cleaning of the components

Cleanliness of the internal vessel and of all the components in the dewar is of primary importance in preserving the purity of the liquid argon. The main operations we performed on the dewar were: degreasing by a bath of water with detergent at 50°C excited by ultrasound; washing with demineralized water (at 90°C); drying and thermal outgassing by means of hot (80°C) water circulating in the serpentine, while evacuating the dewar with a two-stage LEYBOLD [15] pumping system. It consisted of a primary rotative pump (type D40B, speed 40m^3/h, max vacuum 10^{-4} mbar) followed by a liquid nitrogen cold trap, to avoid back-diffusion of mechanical oil, and of a magnetic, oil-free, turbo-molecular pump (type TURBOVAC 340M, speed 300 l/s, max vacuum $\approx 10^{-8}$ mbar) directly connected onto the dewar through a DN 100 flange. The pressure and the residual gas composition were continually checked by means of a mass spectrometer (LEYBOLD type QUADRUVAC PGA 100) also connected on the top flange of the dewar. Following a similar procedure in the tests made with the small-scale chambers, we reached a degassing rate at room temperature of 10^{-12} mbar l $cm^{-2}s^{-1}$ compatible with what we expected from stainless steel surfaces and found it to be perfectly adequate for ultrapure argon. After two weeks of bake-out we reached a residual pressure at room temperature of 5×10^{-8} mbar and a total degassing rate of 1.5×10^{-11} mbar/s corresponding again to a specific degassing rate of 3.3×10^{-12} mbar l $cm^{-2}s^{-1}$.

We then opened the flange and introduced all the detector elements as well as the necessary probes. The bake-out was performed again by circulating water at 80°C in the serpentines, with purified argon gas now in the dewar to have thermal contact between the walls and internal parts. After two weeks, the residual pressure in the evacuated dewar was 5×10^{-8} mbar at room temperature and the total degassing rate was 3×10^{-9} mbar/s. This value is more than two orders of magnitude greater than that reached with the empty dewar; the increase is due to the large surfaces of the detector elements (mainly the chambers and the cables) and the higher outgassing rate from the Kapton surfaces of the cables. When the system is in operation, most of these materials are at liquid argon temperature and then the degassing rate is reduced. We then decided to start the filling operations.

5. Mechanics of the chambers

There are two wire chambers on each side of the central septum. Each chamber consists of three planes of wires. As mentioned in the introduction, going from outside to inside, the first plane is a screening/focusing grid followed by the induction plane and finally by the collection plane.

We have studied the geometry of the wire planes both by simulation and by construction and operation of a prototype liquid argon TPC. The results have been published in Reference [7] where the optimized geometry is fully discussed.

We recall here only that the induction plane is made by doublets of sense-wires (each doublet is read out by one amplifier) separated by 0.6 mm; the centres of two adjacent doublets are separated by 2 mm and there is a screen wire between them. The ratio of the electric fields above the screening grid (E_1) and between it and the induction plane (E_2) are chosen to focus the field lines in between the two sense-wires of the doublet as shown in Figure 1. This geometry has two advantages: i) the charge induced by a drifting electron is almost independent of its position in the drift cell, and ii) an electron drifting in one cell induces only a small fraction (<6%) of the total charge in the contiguous cells. The collection plane is made of sense-wires at a 2 mm pitch separated by screen wires. The fields above (E_2) and below (E_3) the induction plane are chosen to assure complete transparency of the induction plane. The condition on the three field intensities is: $E_3=E_2=5\,E_1$.

The wires (stainless steel, 100 μm in diameter) are kept in position and under tension on the frame of the chamber by a structure made out of MACOR [16] bars. They are held by small conical tubes crimped around them, while the tubes are held in turn by the holes drilled in the MACOR bar. Their diameter is 150 μm. In the case of the doublets of the induction plane we insert both wires in the same tube (300 μm in diameter).

The complicated structure and the closeness (0.6 and 0.7 mm in the induction plane, 1 mm in the collection plane) of the adjacent wires forced us to drill two different rows in the MACOR bars. The wires then pass over combs to assure their correct position, as shown in Figure 5 for the induction. MACOR combs are also used every 80 cm in the induction plane, where the wires are longer, to reduce the gravitational sag as well as the electrical instability.

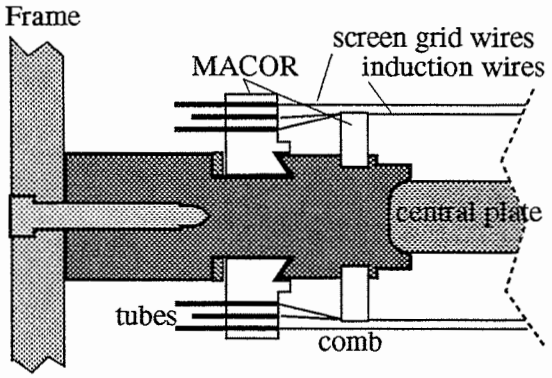

Figure 5 : Detail of the MACOR pieces holding the wires of the screen grid and induction planes

The wires of the collection plane are strung at 500 g, those of the induction plane at 750 g.

Wires and tubes were cleaned in acetone, alcohol, and hexane baths excited by ultrasound.

Each drift volume has a total of 1800 vertical wires (2.4 m long) of which 900 are sense-wires (corresponding to 450 pairs). The collection plane consists of a total of 2400 horizontal wires (0.9 m long) of which 1200 are sense-wires.

A wire-stretching apparatus was designed and built for the assembly of the two chambers. It is composed of the following items: a trolley taking the wires from one side of the chamber to the other, a piston to define the tension of the wire that consists of some brass weights suspended in dynamic equilibrium on a compressed air cushion and a movable hydraulic nipper to crimp the wire in the copper tube. The tension of each wire was checked both online and after completion of the chamber by inducing resonant conditions in the wire.

The total number of sense-wires (collection plus induction) for the two drift chambers of the detector is 3300. Unfortunately, the surface available for the corresponding feedthroughs is not enough even with the special design described in Section 8. For this reason, we decided to electrically connect each horizontal sense-wire of one chamber together with the corresponding one of the other chamber. The reduced number of feedthroughs (2100) could then be placed more easily on the available area.

The final cleaning of the chamber was performed with separate baths of acetone, methanol, and hexane; the system was then assembled in a clean room.

6. Purification system

The purification system design is based on a systematic study made previously. The contribution to the purification process of different commonly used elements was systematically investigated. The results are published elsewhere [8]. The adopted configuration is shown schematically in Figure 6. It is constructed using two industrial high-flux (100 m^3/h at NTP) cartridges from Messer Griesheim, modified by substituting the original flanges with ConFlat type [17] ones to allow high-vacuum treatment. The first cartridge is HYDROSORB [18] (a mixture of molecular sieves 5A and 13X) where its principal effect is to remove hydrocarbons by physical absorption. The second cartridge is OXISORB [18], used mainly to remove oxygen. All the components of the system are of ultrahigh vacuum grade. Valves are from NUPRO [19] or VAT [20], flanges are the ConFlat type with copper gaskets.

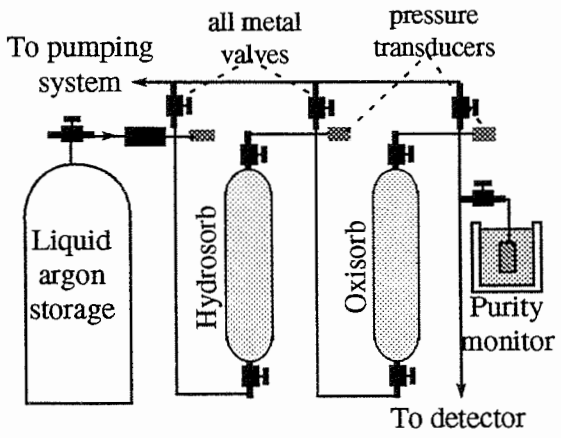

Figure 6 : Schematic view of the purification system

All the components of the system are preliminarily cleaned following the procedures developed at CERN for the high-vacuum LEP components; the system is baked under vacuum (10^{-7} mbar) at 200°C. The new OXISORB and HYDROSORB cartridges are always purged by flushing through them some hundred litres of argon.

We use commercial liquid argon as input to the purification system. After evaporation, the argon gas goes through the two cartridges and on to its final destination. In parallel with the pipe to the detector dewar, we can fill a monitor chamber to measure the free-electron lifetime. During the filling of the detector vessel the flux through the purifier was 7000 l/h (NTP). The free electron lifetime was checked periodically and always found at the limits of the sensitivity of the monitor, i.e. several milliseconds long.

The monitor chambers we use for measuring and controlling the electron lifetime (a second one is on the bottom of the detector dewar) have been described elsewhere [8]. We recall here only that the monitor is a doubly gridded ionization chamber, shown schematically in Figure 7. The anode and cathode are almost completely screened by two grids located 1 cm from each electrode. The field intensities are chosen to insure complete transparency of the grids. The two grids are separated by a 5 cm long drift space. We measure the attenuation due to electronegative impurities of an electron cloud drifting over this distance by comparing the charge leaving the cathode with that reaching the anode.

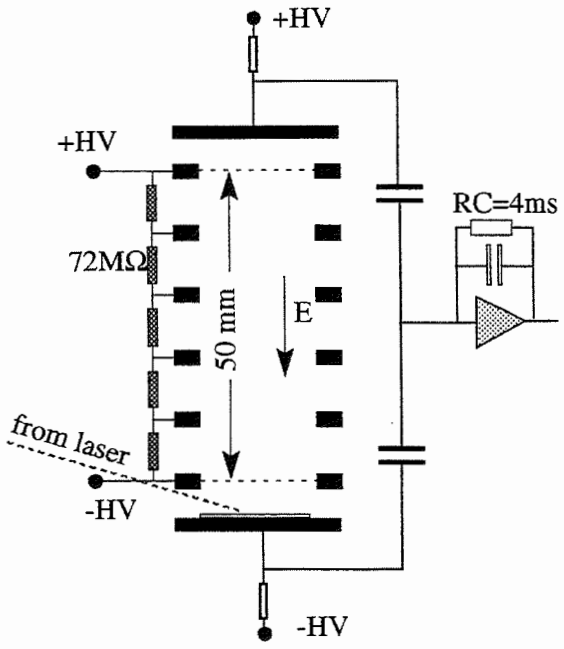

Figure 7 : Schematic view of the purity monitor

The currents from the cathode and the anode feed the same integrating amplifier. Free electrons are produced by a short (20 ns) UV (266 nm wavelength) laser pulse brought to a gold deposit on the copper cathode through an optical fibre. The electron cloud, photoproduced by the light pulse, drifts initially to the first grid producing a positive current in the amplifier. This current vanishes the instant the electrons cross the cathode

grid. The charge integrated by the amplifier is then equal to the charge Q_c produced at the cathode.

While the charge drifts in the uniform field between the two grids, no current is seen by the amplifier. If electronegative impurities are present, its value diminishes. When the charge finally crosses the anode grid it produces a negative current in the input of the amplifier and a negative step in the output (charge) signal; the height of the step is equal to the surviving charge (Q_a) reaching the anode (see Figure 8). As shown in reference [8], if T_w is the drift time and τ the free-electron lifetime, we have simply: $Q_a/Q_c = \exp(-T_w/\tau)$. Obviously the sensitivity is higher for longer drift times, which can be obtained by working with low electric field intensities. The minimum practical field intensity is 50V/cm corresponding to a maximum measurable lifetime of 2–3 ms.

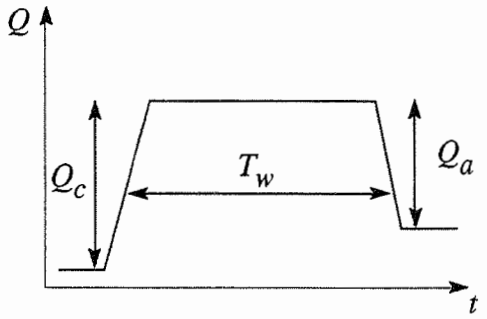

Figure 8 : The charge pulse of the purity monitor

7. Internal cables

As mentioned before, there is no charge amplification at the wires in a liquid argon TPC. As a consequence, the charge signal is very small, typically between one and two femtocoulomb for a 2 mm pitch (or between 6000 and 12 000 electrons). The equivalent noise charge (ENC) from the preamplifiers must be reduced to the physically allowed minimum. The main contribution comes from series noise that is proportional to the input capacitance of the amplifiers located immediately outside the upper flange of the dewar. The input capacitance is the sum of the sense-wire capacitance and the capacitance of the connecting cable. The latter must be reduced as much as possible. The capacitance per unit length is 30 pF/m for the sense-wire doublets of the induction plane, corresponding to a total capacitance (2.4 m length) of 72 pF. The capacitance per unit length of the collection wires is 20 pF/m corresponding to a total capacitance (two together of 0.9 m length) of 36 pF.

In summary, the specifications of the cables are: the capacitance per unit length must be a minimum, the cross talk among channels must be as low as possible, and the materials used should not contaminate the ultrapure argon.

The cable we finally developed is shown schematically in Figure 9. The basic element is a metallized (18 μm Cu) Kapton flexible printed-circuit (75 μm thick; it contains 8 signal strips (127 μm wide) interleaved with 9 screen strips (3500 μm wide) that are connected with the sense-wires and the

screen wires respectively. A cable stack is by made overlapping 32 printed circuits for a total of 256 channels. The printed circuits are separated by 1.5 mm diameter Teflon spacers as shown in Figure 9. Contiguous printed circuits in the stack are staggered by half a period to assure the best screening of the channel strips. The last (upper) flat cable in the stack is made of a continuous screen layer. A female connector is clamped at the end of each flat cable with the pitch matching the pitch of the pins on the feedthroughs.

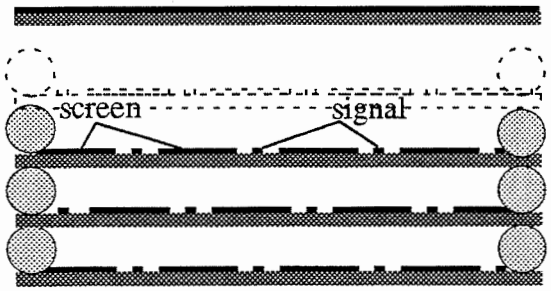

Figure 9 : Schematic view (not to scale) of a section of the stack cable showing the Kapton layers, the copper signal and screen strips, and the Teflon spacers

The capacitance per unit length is low (40 pF/m) giving a total capacitance of the 3.5 m long cables of 140 pF and the cross-capacitance is <2%. The materials are known to be non-contaminating and are easy to clean. On the other hand, there are difficulties in producing long cables and in keeping the layers separate.

Each cable-stack follows a vertical frame of the chamber and goes to a feedthrough matrix (one for each cable stack), through the upper service area.

8. Feedthroughs

As mentioned in Section 5 we have a total of 2100 signal wires that must reach the amplifiers located outside the detector dewar. We also need two feedthroughs for the 45 kV potential of the cathodes for the two semi-cylindrical sectors. We will now describe the two types of feedthroughs.

8.1 Signal feedthroughs

The problems to be solved in designing and building the signal feedthroughs are the following: the feedthroughs must be completely reliable; not one in the more than two thousand needed must leak. The space taken by each channel must be as small as possible, given the high total number and the limited space available on the upper flange. They must withstand a moderately high voltage (1.5 kV) with respect to ground. The materials used should not contaminate the ultrapure argon. The cost must be as low as possible.

After a series of tests, the following solution was adopted. For each cable-stack containing 256 signal strips plus screen strips a feedthrough matrix is provided. Each matrix contains a total of 350 feedthroughs and is located on the upper flange, in correspondence with one of the eight tubes going to one box containing the preamplifiers.

The matrices are made with the printed circuit board technique. Each of them is a sandwich of one 1.6 mm and two 0.8 mm thick FR4 epoxy foils pierced by metallized holes, as shown schematically in Figure 10. The matrix contains 35 rows of 10 holes each at a 2.54 mm pitch; the distance between two rows is 1.27 mm. Pins are soldered in the holes to ensure vacuum tightness. The two lateral pins in each row are used for the screen strips, while the central eight are used for the signal strips of each flat Kapton cable. After soldering, the plate with the pins is washed in separate baths of acetone, alcohol, and hexane excited by ultrasound.

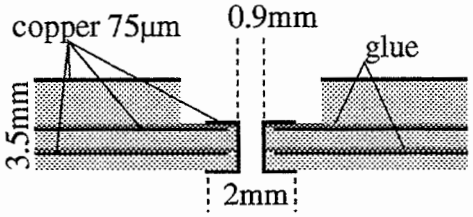

Figure 10 : Schematic view of one of the signal feedthrough holes in the printed circuit

Each plate is tested for vacuum tightness and for electrical insulation, verifying that pins can stand a maximum potential difference of 1.5 kV between them and also to ground.

The vacuum between the plate and the dewar flange is assured by an indium gasket.

Figure 11 is a schematic representation of the electrical connections showing the resistors to the voltage supply, the blocking capacitors, and the preamplifiers (sense-wires and screening wires are brought to the same potential to avoid discharges and microphonic noise).

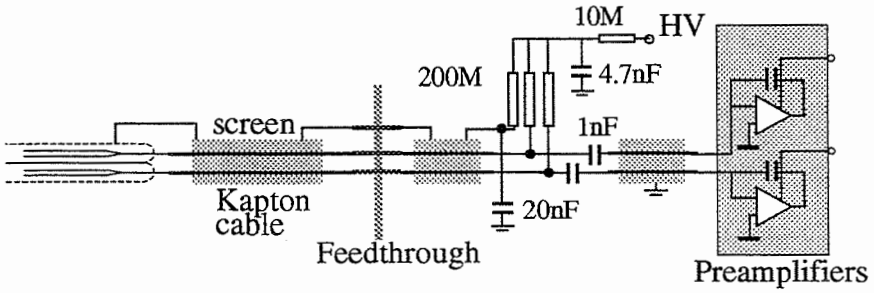

Figure 11 : Schematic view of the electrical connections of sense and screen wires

8.2 High-voltage feedthroughs

Their specifications are the following: they must keep up to 45 kV with respect to ground; they must stand the temperature difference between room temperature and 87 K of the liquid argon; humidity condensation and frost formation must be avoided; only non-contaminating material must be used.

After a series of tests, the solution shown schematically in Figure 12 was adopted. The cable from the high-voltage supply first penetrates a stainless steel box containing dry N_2 to avoid frost. The ground screen of the cable is terminated on the outside wall of the box; the copper conductor and the polyethylene insulator of the cable enter the box. Inside the box the

conductor is terminated with an almost spherical stainless steel piece that is in contact with a stainless steel bar contained in a ceramic insulator. The lower part of the insulator is tube-shaped and is contained in a second chamber, immediately following the box, where we maintain a vacuum of pressure less than 10^{-7} mbar.

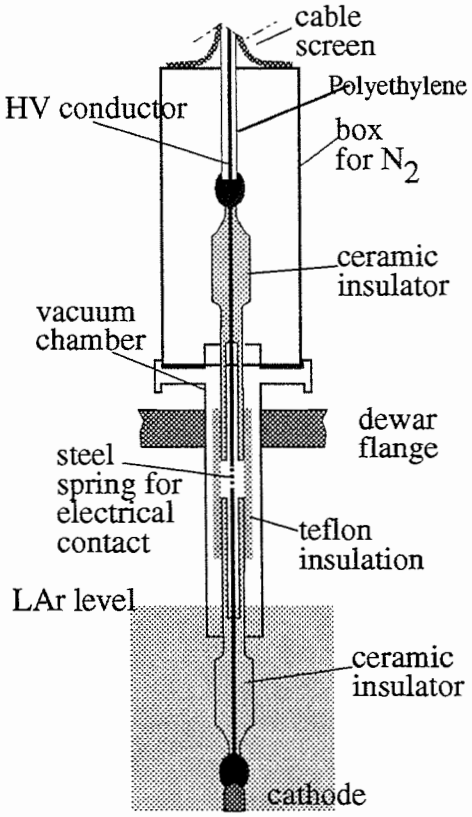

Figure 12 : Schematic view of the HV feedthrough

The stainless steel bar ends in this box (to allow opening of the system) and is taken in safe electrical contact with a second, similar, steel bar contained in a second ceramic insulator by a stainless steel spring. The insulator leaves the vacuum chamber inside the dewar and the bar leaves the insulator inside the liquid argon, in a safe high-electrostatic rigidity environment, and, through a second spheroidal steel piece, is connected to the cathode.

The system has been tested for safety up to 100 kV.

9. Electronics

9.1 Analog electronics

The analog electronics chain is divided into three parts located in separate cabinets: the charge sensitive preamplifier and associated high voltage decoupling network, the amplifier / differential line driver, and the line receiver / FADC driver as sketched in Figure 13.

The sense-wires are connected to the analog chain by the internal Kapton cables and the feedthroughs described in the previous sections.

On the high-voltage decoupling network, sketched in Figure 14, the following functions are implemented: the high-voltage distribution to the sense-wire and commons, the preamplifier input decoupling, and the charge injection through a test capacitance. The network, serving eight sense-wires, is made on a ceramic hybrid circuit and is able to stand voltages up to 1.5 kV with leakage currents in the nanoampere region. The value of the resistors R is 200 MΩ and the decoupling capacitors C_b =1 nF, 2 kV.

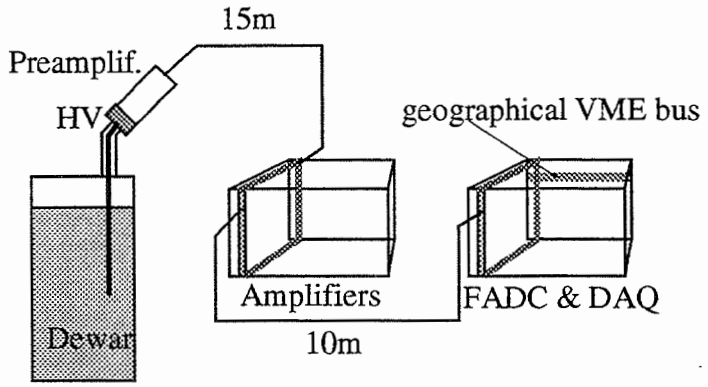

Figure 13 : Analog electronics physical layout

The calibration capacitances (C_t) are made using ceramic as a dielectric and have a value of 3.5 pF ±1.5%. As their accuracy is not good enough for calibration purposes, each capacitance on the hybrid is measured with a precision better than 0.5% and a calibration constant is associated with every sense-wire.

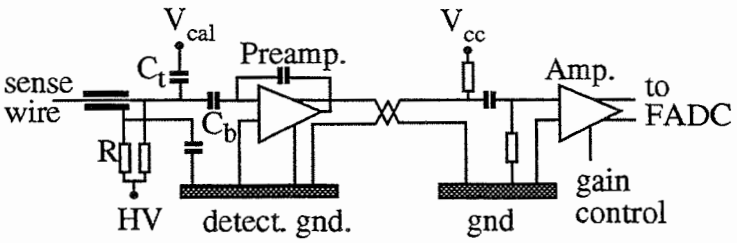

Figure 14 : Front-end electronics

The preamplifier is made using the very well known j-FET input stage with unfolded cascode architecture [21]. Calculations made on the equivalent noise charge [22] demonstrate that in our detector the serial noise is dominant because of the rather high input detector capacitance (100 pF range).

The preamplifier schematics and its main characteristics are given in Figure 15. The actual circuit, made with hybrid technology, uses a single power supply of 12 V and a negative reference voltage of –7 V. The total power consumption is 100 mW. The circuit is a current integrator with a feed-back equivalent capacitance of 0.25 pF, a decay time-constant of about 0.5 ms and an equivalent input impedance of 200 Ω.

The input stage J1-J2, is a cascade made with two high transconductance j-FETs allowing good performance with respect to the serial noise. The j-FET J3 is a current generator delivering a 5 mA current to the input stage. The following bipolar transistors (T1, T2, T3) act as a non-inverting amplifier with a gain of ten. This increases the open loop gain,

hence reducing the input impedance. The output stage (T4), delivers a signal current of 8 μA/fC superimposed on the power supply DC current. The two currents share the same twisted-pair on each preamplifier avoiding any unexpected coupling between channels through the power supplies.

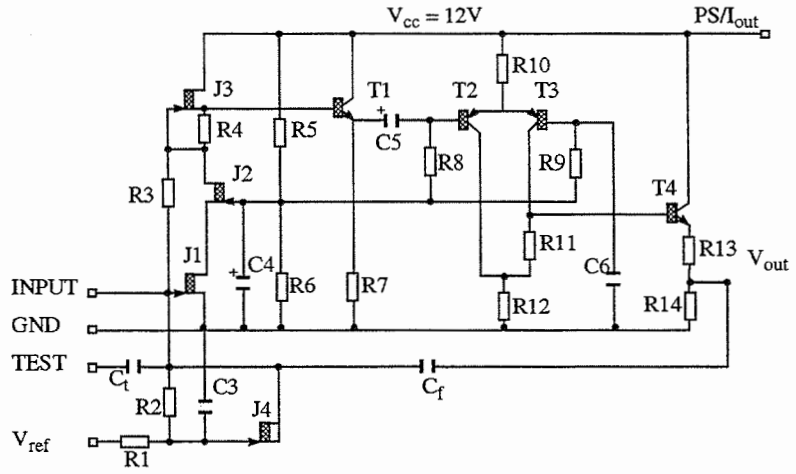

Figure 15 : Schematic of the preamplifier

This architecture presents the same advantages as a classical differential voltage transmission without the need of an additional differential output stage.

We measured the noise of the amplification chain, shaping with a filter of the CR-RC-RC type (with a maximum at 2 μs) as a function of the input capacitance. The circuit shows a noise slope of 2.5 electrons per picofarad starting at 330 electrons at zero detector input capacitance.

Since the information to be digitized is the charge collected or induced on the sense-wire, the shaping is not implemented. Under these conditions the ENC is about 800 electrons for a 100 pF input capacitance, representing a typical value for collection wires.

The preamplifiers are mounted, in sets of 256 channels, inside water-cooled Faraday cages.

The amplifier section is based essentially on a commercial video amplifier with voltage gain control. Its output stage delivers (in differential mode on 120 Ω) a DC-free signal of typically 18 mV/fC to the digitization board.

The FADCs are located on the data acquisition board. Their input line receivers are made with standard fast operational amplifiers having a DC-coupled differential input on 120 Ω and a voltage gain of 5.45. Two additional single ended control inputs are implemented, the first to set the ADC pedestal over the entire range and the second to inject a fast test pulse. The circuit uses the internal FADC reference to shift the DC input level to the voltage required by the FADC under all temperature conditions.

The analog chain gain is set to achieve a sensitivity of about 400 e/count corresponding to a signal of about 30 counts for the minimum collected charge.

9.2 The digital readout

The ICARUS detector readout system behaves as a large multichannel wave-form recorder. It effectively stores the charge information collected by each sense-wire during a time corresponding at least to the maximum drift time of the electrons (1.6 ms). The high resolution that has to be achieved, both in space and time sampling, brings the size of a single event to over hundreds of kilobytes. The useful signal occupies only a small fraction of the data sample. Although in the initial phases of the experiment the complete information is useful for troubleshooting and debugging purposes, this is the real bottleneck of the whole data-taking system, overloading both the online and offline processing.

To improve performance in the future, the detector readout will be divided into a number of subsystems with independent and identical readout structures to increase the acquisition rate. The way to reduce the dimension of the event is to implement real-time hardware solutions that will be able to detect valid data regions (amounting to only a few kilobytes) and save them on mass-storage devices. Of course, this step can only be performed when the studies on the signal extraction algorithms have been consolidated.

All the digital electronics was custom designed for the ICARUS prototype keeping in mind the final large detector [23]. It is a VME-based system performing a full 1.6 ms long digitization and recording of each signal from the analog stage.

The current signals coming from each of the sense-wires are analogically integrated and filtered as described in the previous paragraph. The charge output of the analog stage is continually digitized and stored for each channel.

The digital conversion module, one for each channel, is a surface-mounted module that consists of the following stages:

i) an analog amplifying section which converts the differential input signal and performs the suitable scaling;

ii) an 8-bit FADC driven by a controllable speed clock. The clock speed can be chosen to be between 2.5 and 20 MHz. The full-scale range is set to 300 mV, equivalent to a charge of 100 000 electrons on the sense-wire. A DAC-controlled baseline allows shifting of the zero level of the ADC to work properly with bipolar signals (e.g. to control the undershoot region of front-end amplifiers). The 8-bit resolution bounds the maximum signal-to-noise ratio to 64 dB (quantization distortion). This fits our present needs as it is far beyond the actual analog noise;

iii) an 8 kbyte memory block. This memory can be subdivided in a number (from 2 to 16) of ring buffers; the FADC output cycles over one buffer switching to the next free one as a trigger comes. This procedure keeps the dead time of the recording to a negligible level (below one clock period) as long as buffers are made free fast enough. Write access cycles are interlaced with read cycles, allowing random access to data from one buffer while running the acquisition on another buffer. The interlacing was chosen instead of dual port memories for reasons of cost.

FADC modules are grouped by 16 on single boards (FM16); these boards fit on a VME-like crate (up to 20 boards on the same crate, giving 320 digital channels).

9.3 Board control and synchronization

To simplify the drive and the synchronization of the high number of ADCs, a parallel structure has been implemented at the crate level: one slot of each crate contains a module (RTX) which distributes the clock and drives the address lines common to the entire FADC set. As a result, all the FADCs in the crate are at any given time performing the same operation, and all the sampled values are stored at the same relative address into the memory buffers.

The RTX module also provides an interface to a proprietary 50-lines bus which chains up to 8 crates to a VME interface (MANAGER). By means of sixteen VME registers supplied by the MANAGER, any VME master may select a specific RTX, set up acquisition parameters, or read the memory contents of the specified channels. The memory content of the selected channel is mapped to the standard VME address space; a read request in that address space will be dispatched by the MANAGER through the proprietary bus and acknowledged as the RTX returns the value.

10. Data acquisition and data filtering

10.1 Functional overview

The protocol to control the digitizer behaviour is based on a two-FIFO queue structure for each RTX. To start acquisition, at least one entry must be submitted to the first queue (FIFO A) which contains the buffers that are available for writing. When a trigger comes, an entry is created on the second queue (FIFO B) reporting the trigger absolute time and the starting point in the ring buffer. The next free buffer, if any, is popped from the FIFO A to continue the acquisition. As long as the event processing software frees buffers at speeds comparable to the trigger rate, the system has no dead time.

10.2 Readout architecture

All the readout system is VME-based. The present set-up is the following:

i) a dedicated VME/VSB 68040 CPU runs the data-acquisition software, which performs ADC control and reading and builds event records on a VME memory module;

ii) a VME-connected workstation polls the event buffer for events, dumping them on tape;

iii) another VME-connected workstation performs the event display, either from the event buffer to monitor acquisition, or directly from the ADCs.

One step to improve the acquisition rate will be to add more dedicated CPUs that will process a portion of the digital channels. Full event reconstruction then can be left to offline processing. This kind of architecture will also allow for independent acquisition on the different ADC subsets. In order to reduce VME bus occupation in this environment, a VSB interface is being implemented on the MANAGER. With this upgrade, every CPU will access its own ADC subset via VSB without interfering with each other, while the VME accesses will be reserved for CPUs' synchronization and event transfer to tape.

10.3 Event imaging

The event display provides two bidimensional images, one for each wire plane. The two coordinates of one view are proportional to the wire number and to the drift time respectively. Each line, corresponding to a channel, reports the charge induced on the sense-wire as a function of time. The sampled charge value is given as the pixel shade, the darker the pixel the higher the charge. Figure 16 shows an example of the resulting image in the collection view. The shape of the signal corresponding to a track is approximately a step function, giving a bad-looking image. Appropriate operations of filtering must be applied.

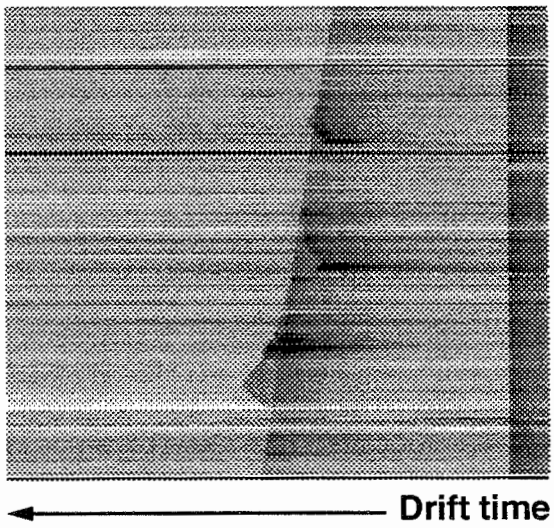

Figure 16 : The collection image of a cosmic-ray track before filtering

An eventual three-dimensional reconstruction will be based on the association of signals occurring at the same time on both wire planes. Ambiguities are possible and could be resolved either by charge consistency or by introducing more induction planes.

10.4 Data filtering

Two different approaches were followed when developing the offline processing algorithms:

1 - A quick procedure was needed to improve event display during the visual scanning activity. The collection signal must be differentiated and the low-frequency noise, mainly due to microphonic pickup, must be reduced as much as possible.

2 - Offline analysis requires a non-biased signal extraction. This in turn implies enhancement of the signal-to-noise ratio and reduction of baseline fluctuations.

A good solution for the first task was found with the SLAD (Shift Left And Difference) filter: the signal is delayed by an amount of time equal to the rise time duration and it is subtracted from itself. This operation doesn't affect either the rising shape or the peak height of the signal; thus the processed image data can still be used to evaluate physics parameters. The main drawback of this filter is that the noise is increased by a factor of the square root of two. Because of this the signal extraction efficiency varies with the signal height, which is not acceptable for offline analysis. The signal from the wire passing the point marked with a rectangle in Figure 16 (where two close tracks are present) is shown in Figure 17 together with the filtered one (SLAD-filtered). The SLAD-filtered image is shown in Figure 18; the quality is very similar to that of bubble chamber pictures.

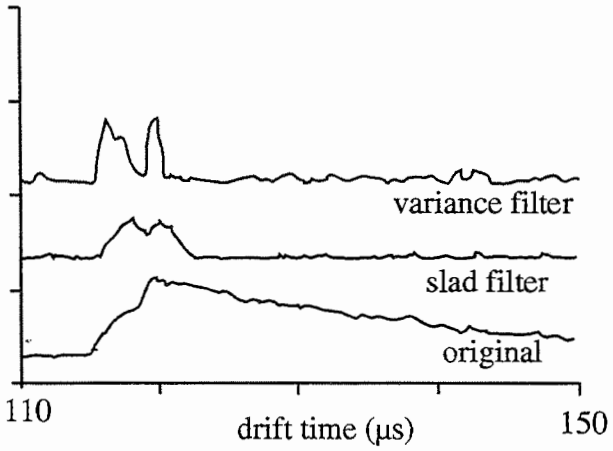

Figure 17 : The signal from the wire in the point marked with a rectangle in Figure 16 as digitized (original) and after filtering by the two algorithms described in the text

A more efficient algorithm, though it consumes much more CPU, matches the requirements of the second approach better and relies on the detection changes in the variance of the signal. The variance is calculated in a window whose length is comparable to the rise-time duration: if no signal is present, its value will equal the noise level. The baseline value of the filter output will thus be constant. Instead, when the window starts to overlap a signal rise front, the variance will rapidly increase. The value reaches the maximum when the window completely covers the signal. The signal-to-noise ratio can be maximized by making the window length equal to the signal rise time. Peak extraction is then simply performed by fixed threshold

discrimination on the pulse height (e.g. three times noise variance) and pulse width. Those two parameters and the window length can be tuned to make signal extraction uniform with respect to the pulse height or to optimize the multiple track separation. Figure 17 also shows the variance filtered signal and Figure 18 the variance filtered image; in both cases the window is nine samples long. The efficiency and the reliability of the algorithm will be discussed elsewhere.

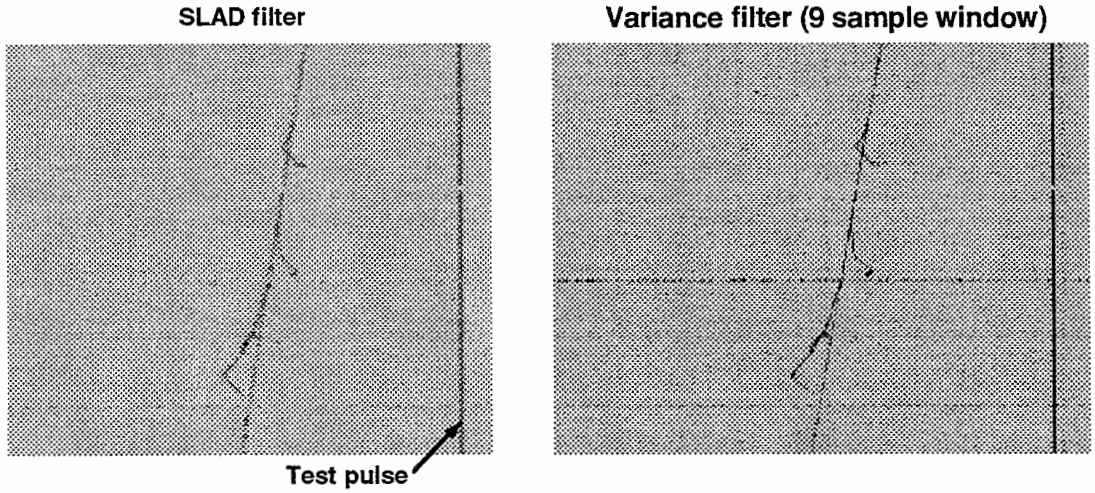

Figure 18 : The image of Figure 16 after SLAD (left) and variance (right) filtering. One noisy channel is visible in the variance-filtered image.

11. Operation and results

In this section we will summarize the principal results we have reached while assembling and operating the three-ton prototype liquid argon TPC. Detailed results on the measurements of the relevant physical parameters will be reported in a separate paper. We will start with a schematic chronological account of the assembly and test phases.

The final assembly of the complete system, including the wire chambers, the argon purification system, the recirculation system and the readout electronics began in January 1991 and was completed in May 1991.

We started with a preliminary filling of the detector with ultrapure argon to verify:

1. the reliability of the mechanics (wire chambers, feedthroughs, electric contacts) under thermal stress;

2. the liquid argon purity level reachable in large volumes for a high gas flow through the purifier;

3. the reliability, the efficiency of the recirculation system, and the consumption of liquid argon.

The liquefaction process was performed in a few steps: (a) cleaning of all the detector pieces in solvents and demineralized water as described in Section 4; (b) evacuation of the dewar down to 10^{-7} mbar and bake-out at 90°C for 15 days; (c) cooling down to liquid argon temperature using pure argon gas to uniformly thermalize the detector for seven days. (d) liquefaction

of commercial liquid argon into the experimental dewar passed through Oxisorb and molecular sieves at a speed of eight litres per hour as described in Section 6.

The results concerning the liquid argon purity were very satisfactory. The electron lifetime measured with the internal purity monitor (described in Section 6) was higher than 3 ms in 300 litres of liquid argon liquefied at a speed of eight litres per hour. It was stable under the action of the recirculation system (running at a speed of four litres per hour).

The purity of the gas phase on top of the liquid was also measured by condensing a small fraction of it into the external purity monitor. The resulting 100 μs electron lifetime, very different from the lifetime in the liquid phase, strongly supports the hypothesis that most of the impurity is produced by outgassing from the warmer surfaces (dewar walls and Kapton cables) in contact with the gas phase and perhaps by small leaks from the more than 2000 feedthroughs. The recirculation system acts efficiently against this process because it extracts the gas phase at the top of the detector, purifies it, and recondenses it back at the bottom of the dewar.

Serious problems were found concerning the wire chambers. A MACOR bar on one of the two chambers broke under the mechanical and thermal stresses. A few wires (about 10 out of more then 8000) of the collection plane of the other chamber lost their tension during cooling down to liquid argon temperature due to bad clamping of the copper pins. This implied that, by applying the voltage on them, short circuits were found between wire planes due to electrostatic attraction. This in turn made it impossible to continue the test.

The liquid argon was evacuated in five days and the detector was brought back to room temperature. The wire chambers were extracted: the one with the broken MACOR was no longer usable and on the other chamber the faulted wires were cut away. We placed in front of the unusable chamber a small chamber that we had previously used in the small-scale tests with the same geometry as the large chambers. The two coordinate planes had 32 sense-wires, each 8 cm long.

The actual filling was started in April. It took 16 days to fill the dewar with 2000 litres of purified liquid argon. The electron lifetime was continually monitored: it was about 1 ms at the beginning, increasing steadily during liquefaction and reaching a stable value of about 3 ms at the end due to the presence of the recirculation system.

A test was done by stopping the recirculation system. The lifetime immediately dropped down to less than 1 ms within 4 hours. Restoration of the purity was achieved in 12 hours by reactivating the recirculation system.

No major defects were found on the wire chamber except a short circuit on some screen wires of the induction plane. This had only the effect of limiting the electric field applicable to the drift region to 700 V/cm.

As a next step we started connecting the analog electronic chain (preamplifiers, HV, decoupling capacitors, test capacitors) onto the signal feedthroughs at one end and the digital boards at the other. The implementation of the complete data acquisition chain for the 272 channels that were available was then completed.

At the end of June the first tracks from cosmic rays were seen on the online display. The detector was operative and we started to collect data. At the same time we worked to improve various parts of the system, in particular the readout electronics. The test capacitances were calibrated to within 1% accuracy and the crosstalk between channels was reduced to below 2%. Software was developed to optimize the data reduction for speed and efficiency and to enhance the signal-to-noise ratio of images for offline analysis (Section 10).

The electron lifetime in the detector is continually recorded and controlled with the internal purity monitor: no significant change in the electron lifetime has ever been found, it fluctuates between 2.5 and 3 ms. At present we do not know if the lifetime is limited to this value because the purifier filters have reached their maximum efficiency, or because the recirculation speed is too low to extract more impurities. We are building a set-up where we will be able both to test other purification methods and to change the recirculation speed.

A large amount of data has been collected with the 3-ton prototype using cosmic-ray and gamma-ray sources to study the response of the detector to a wide range of energies (from a few MeV to several GeV).

In the data-taking we have used two main triggers, one for cosmic-ray events (non-contained events) and one for events from the source (contained events).

The trigger for non-contained events was made up of three scintillators, placed two on the top and one on the bottom of the dewar in coincidence with the signals from two groups of 16 horizontal wires each, one group at the top and one group at the bottom of the wire chamber. The trigger for muons stopping in the detector was the same, but without the lowest scintillator and with the lowest group of wires in anticoincidence.

The trigger for low-energy contained events was an internal trigger built with the signals from the groups of 16 contiguous collection wires. To trigger on a region of the chamber we use an OR of the corresponding groups of wires with those at the borders in anticoincidence (to select contained events). In this way we can easily trigger down to 1 MeV in energy deposition.

Figure 19 shows one of the first events we collected with the small chamber; it is a cosmic ray (probably a muon) crossing the detector triggered by the external counters in delayed coincidence with the grid signal of the chamber. The track crosses the detector almost parallel to the wire planes (drift times almost constant) at about 45° to the direction of the wires (images in the two views are very similar). The two views xz (induction) and yz (collection) are shown. As can be seen, the images are very neat: the S/N is 6 in the induction plane, 10 in the collection plane as expected with an E.N.C. ≈ 1000 electrons. The electric field intensity was 330V/cm corresponding to a drift speed of 1.35 mm/μs; the clock of the FADC was set to a 200 ns period; one pixel is then 2×0.27 mm^2, but the two scales of the figure are the same (each frame corresponds to 71 mm horizontally and 62 mm vertically).

The signal induced on the screening grid (7×8 cm^2, all wires connected together) is fed to an integrating amplifier. In the lower part of the

figure the charge signal from the screen grid is shown together with the logic signal from the external trigger (the external $t = 0$). The signal from the screen grid grows initially very slowly when the charge is still far away and the solid angle under which it sees the grid is small and slowly varying. When the charge crosses the grid the current inverts and becomes larger in value: the charges are now crossing the narrow (2 mm) gap between the screen and the induction plane, and the fraction of the electric flux of the charge field collected by the screen varies rapidly (fast signal).

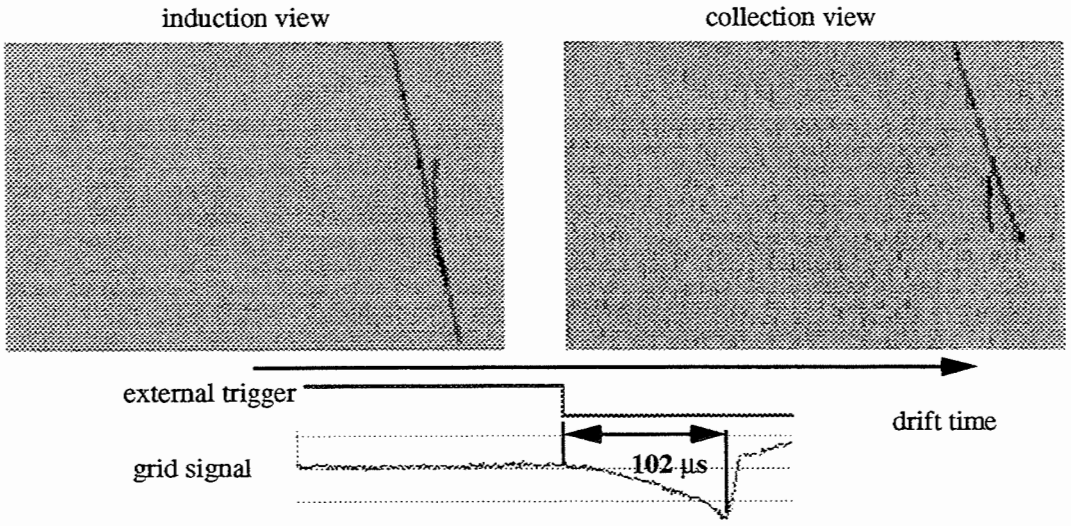

Figure 19 : The two images of a cosmic-ray track. Vertical heights are 32 wires with 2 mm pitch. In the lower part the external trigger and grid signal are shown

The fast signal is proportional to the inducing charge and, hence, to the energy deposited. In the present case this is the energy released by a minimum-ionizing particle in 6 cm, that is 13.2 MeV. As can be seen in the figure the noise is at a very low level.

An important piece of information that can be extracted from the screen grid signal is the event time ($t = 0$). In the present case we know the time of the event from the external trigger; if we do not know it (as for contained events) we can evaluate the instant when the signal becomes different from the baseline. In the example this can be done rather precisely, within a few microseconds (corresponding to an uncertainty in the absolute event position of a few mm).

Unfortunately, the situation is more difficult for more complicated events (with tracks at different angles) and for larger area grids (with increased noise), but the example shows that the induced signal on suitably designed electrodes can be used in a physics experiment for $t = 0$ information (an alternative that is obvious in theory but not in practice is using the scintillation light). Further R&D work is necessary and under way on this point.

Figure 20 shows the collection view in the large chamber of a stopping muon and of the decay electron (32 MeV energy). Again the quality of the image (approximately 40×40 cm^2 wide) is of bubble chamber grade.

The separation between the electron and muon track is due to the 3 μs muon lifetime. The gray level of the pixels codes the pulse height, proportional to the collected charge. The increase in ionization near the stopping point is easily noticed. For contained events with a track stopping in the detector without decay or decaying without visible products, the increase of the ionization yields the direction of the track.

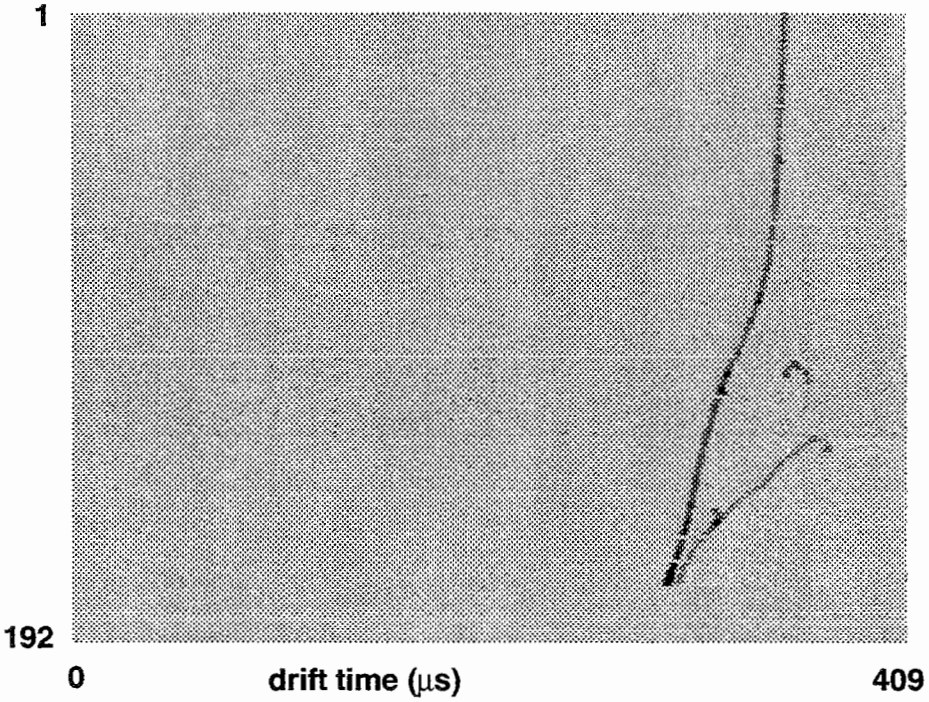

Figure 20 : A stopping muon and decay electron track. Collection view. The dimensions of the image are approximately 40×40 cm^2. The gap between muon and electron tracks is due to the 3 μs long life of the muon.

Figure 21 is a plot of the average collected charge vs. the distance from the end point for samples of stopping muons at two different electric field intensities. The increase near the end point is clearly visible. Notice that the collected charge is not proportional to that delivered by the ionizing particle (Birk's law); at higher values of dE/dx the recombination is more important especially at low field intensities. The effect is visible in Figure 21 where for comparison the expected curve in absence of recombination is also shown. We are systematically analysing a high statistics sample of stopping muons to study the recombination process.

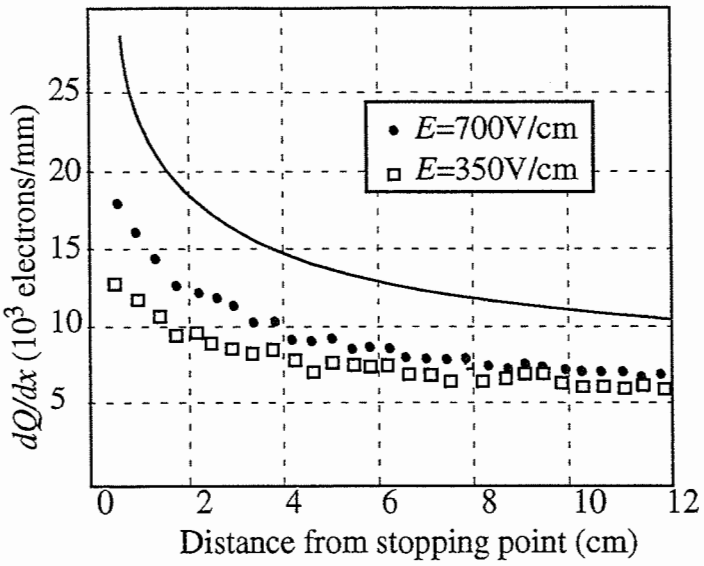

Figure 21 : Average collected charge as a function of the distance from the end point of stopping muons. The curve is the result of a Monte Carlo calculation not including recombination.

As a further example we show in Figure 22 the collection view of an electromagnetic shower. Very fine details of the event are noticeable; the shower contains both an electromagnetic and a hadronic component; a stopping muon and the decay electron are also visible. In particular, the small black dots are not noise but part of the real events; they are due to gammas with energy around 1 MeV.

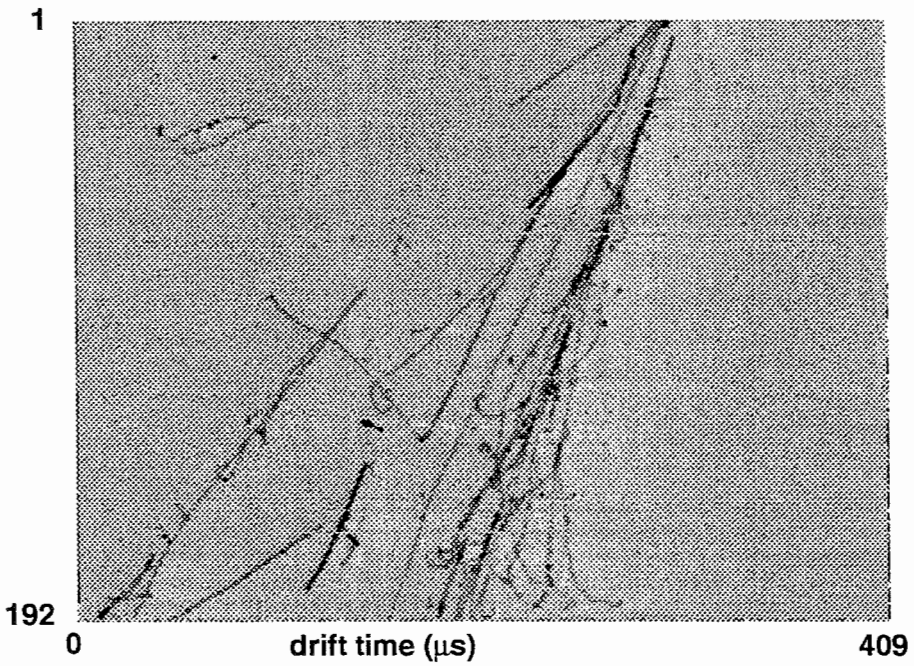

Figure 22 : Collection view of a cosmic-ray induced shower

11.1 Electron lifetime

The electron lifetime value given by the purity monitor has been checked by means of cosmic-ray muons vertically crossing the drift volume. The events have been selected by requiring that there be no evidence of large multiple scattering or delta rays ensuring that they were minimum-ionizing particles.

The distribution of the charge deposited along the tracks is measured for each drift-time slice with a binning of 20 μs; the most probable value is extracted and plotted as a function of the drift time as shown in Figure 23. An exponential fit to this plot directly gives the free electron yield (the intercept) and the electron lifetime (the slope). The fits shown in Figure 23 give at 350V/cm, $\tau = 2.2 \pm 0.2\ \mu\sigma$ for the lifetime and $Q = 10860 \pm 150$ electrons for the free charge on 2 mm, and at 200V/cm $\tau = 2.1 \pm 0.2\ \mu\sigma$ and $Q = 9630 \pm 150$ electrons. The lifetime measurement has been repeatedly performed, giving a stable value of about 2.5 ms that agrees with the data from the purity monitor.

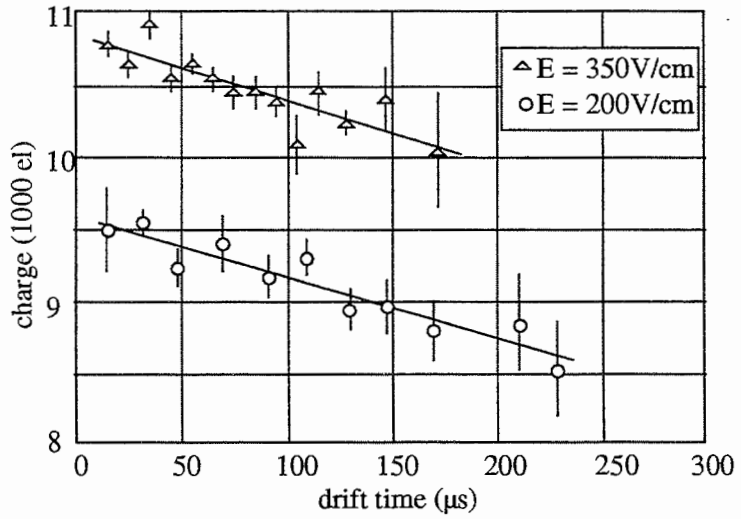

Figure 23 : Maximum collected charge per 2 mm vs. drift distance for minimum-ionizing particles

From the analysis of through-going cosmic muons it has already been possible to extract several parameters characterizing the detector: electron lifetime, free electron yield, electron diffusion, energy resolution, spatial resolution, and particle identification capability.

As for the γ source events, the analysis is still preliminary and concerns for the time being only the self-trigger capability and the energy resolution. In the future we want to exploit this source to simulate solar neutrino events to verify the reconstruction capability of the event kinematics.

Figure 24 shows an example of a low-energy event from the radioactive source. The two views of a Compton electron whose energy is about 5 MeV are shown. The trigger was the internal one described above while the electric field in the drift region was 350V/cm. The images are very clear, particularly after noise reduction by the filtering algorithms.

We are evaluating the energy resolution of the detector at low energy both by studying the fluctuation in the energy loss per unit length of minimum-ionizing tracks and by analysing the events from the γ source.

Spatial resolution is evaluated by studying the residuals of a linear fit for tracks of minimum-ionizing particles. Angular resolution for electrons with energy of some MeV, interesting for solar neutrino experiments, is under study with events from the γ source.

Detailed discussion of these results will be presented in a separate paper.

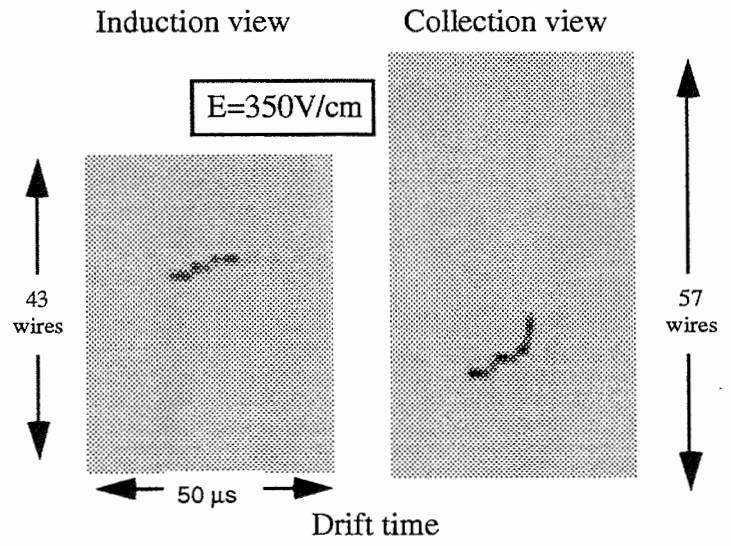

Figure 24 : The two views of a 5 MeV electron

12. Conclusion

The experience with the 3-ton prototype, equipped with complex mechanical and electrical apparata immersed in the liquid and with hundreds of feedthroughs, has shown that the ultrapure liquid argon technique is reliable. Ultrapure liquid argon can be obtained using commercially available components and ultrahigh vacuum techniques; procedures to keep the purity in an operational detector for long periods of time have been developed and fully tested.

Three-dimensional high-granularity images of the ionizing events have been obtained with a suitable geometry of the wire chambers. Both coherent and incoherent noises have been reduced enough to obtain good contrast images, especially after suitable filtering. Bubble-chamber-quality images have been obtained.

The important physical parameters of the detector, free electron yield, recombination probability, drift velocity, diffusion coefficient, free electron lifetime, and their possible dependence on the electric field intensity are under study. Up to now, they are found to be in agreement with the theoretical models.

In summary, a novel detector is now available for physics, even if some technical improvements are still necessary and, in fact, under way:

a) liquid phase purification to speed up the filling of very large volumes. Recently we have succeeded in purifying commercial liquid argon

in the liquid phase obtaining free-electron lifetimes of several milliseconds at a rate of 500 l/h. We have not yet tested the maximum rate reachable. The results are being published elsewhere [24];

b) doping of the liquid argon to achieve linear dependence of dE/dx on the ionization without compromising spatial resolution;

c) design of very large wire chambers mechanically reliable during the cool-down to liquid argon temperature. We have now developed a new design of the wire chambers that foresees the construction of separate modules that will be systematically tested before being assembled;

d) development of preamplifiers to be used immediately near the wires, i.e. in the liquid to eliminate the capacitance of the cables and to reduce the noise. We have built and tested in liquid argon some hybrid amplifiers based on a full j-FET design. The output signal is again of the current type. The ENC is very satisfactory and work is in progress to optimize layout and electrical connections;

e) study of the best $t = 0$ system, specially optimized for the solar neutrino search.

13. References

[1] C. Rubbia, CERN–EP Internal Report 77–8 (1977).

[2] ICARUS Collaboration, ICARUS a Proposal for the Gran Sasso Laboratory, INFN/AE–85/7, Frascati, 1985.

[3] W.A. Huffman, J.M. Losecco and C. Rubbia, IEEE Trans. Nucl. Sci. **NS–26** (1979) 64.

[4] H.H. Chen and J.F. Lathrop, Nucl. Instr. and Meth. **150** (1978) 585; H.H. Chen and P.J. Doe, IEEE Trans. Nucl. Sci. **NS–28** (1981) 454; P.J. Doe, H.J. Mahler and H.H. Chen, Nucl. Instr. and Meth. **199** (1982) 639.

[5] E. Gatti et al., IEEE Trans. Nucl. Sci. **NS–26** (1970) 2910.

[6] E. Buckley et al., Nucl. Instr. and Meth. **A275** (1989) 364.

[7] E. Bonetti et al., Nucl. Instr. and Meth. **A286** (1990) 135.

[8] A. Bettini et al., Nucl. Instr. and Meth. **A305** (1991) 177.

[9] Oxisorb is a trade mark of Messer Griesheim GmbH.

[10] M. Miyajima, T. Takahashi, S. Konno, T. Hamada, S. Kubota, E. Shibamura and T. Doke, Phys. Rev. **A9** (1974) 1438; E. Shibamura, A. Hitachi, T. Doke, T. Takahashi, S. Kubota and M. Miyajima, Nucl. Instr. and Meth. **131** (1975) 249; E. Aprile, W.H.M. Ku, J. Park and H. Schwartz, Nucl. Instr. and Meth. **A261** (1987) 519; E. Shibamura, Proc. of the JCLRD International Conference, p. 198, Tokyo 1992.

[11] ICARUS Collaboration, ICARUS I: An Optimized Real Time Detector of Solar Neutrinos, LNF – 89/005 (R).

[12] P. Benetti et al. Nucl. Instr. Meth. **A315** (1992) 223; P. Benetti et al., Proceedings of the Conference Calorimetry in High Energy Physics, p. 278, Word Scientific, 1992; P. Benetti et al., Proceedings of the Dallas Conference on High Energy Physics, 1992.

[13] The cryostat has been produced by Zanon Spa. Schio (Italy).

[14] Produced by CINEL Srl. Padova (Italy).

[15] Leybold–Heraus GmbH. Köln (Germany).

[16] MACOR is a trade mark from Corning Glass Inc.

[17] ConFlat is a trademark of Varian, USA.
[18] HYDROSORB & OXISORB type R20, Messer Griesheim GmbH, Düsseldorf, Germany.
[19] NUPRO company, Ohio, USA.
[20] VAT, Aktiengesellschaft CH–9469 Haag Switzerland.
[21] V. Radeka, IEEE Trans. Nucl. Sci. **NS–21** (1974) 51.
[22] C. Bacci et al., Nucl. Instr. and Meth. **A273** (1988) 321; S. Centro, Nucl. Instr. and Meth. **A315** (1992) 404.
[23] The digital system has been produced by CAEN Spa. Viareggio (Italy).
[24] ICARUS Collaboration, Argon Purification in the Liquid Phase, DFPD 93/EP/15, to be published.

14. Properties of stopping muons in liquid argon

In the study of atmospheric neutrinos, it is most important to distinguish between neutrinos and antineutrinos in order to have the maximum sensitivity in the search for possible oscillations, since only either neutrinos or antineutrinos can have enhanced oscillations in matter, but not both. Most muons produced in ICARUS by atmospheric ν_μ's or $\bar{\nu}_\mu$'s will stop in the detector since their energy is in the range 106 MeV to 1 GeV, with an average around 200 MeV. A 200 MeV muon, for instance, will travel about 95 cm in the liquid argon while the diameter of the vessel is 16 metres.

A μ^+ stopping in the liquid argon will then decay into an $e^+\nu_e\bar{\nu}_\mu$ (Figure 1) while a large fraction of the μ^-'s is captured by an argon nucleus giving an event of a very different topology (Figure 2) from that of a μ^+.

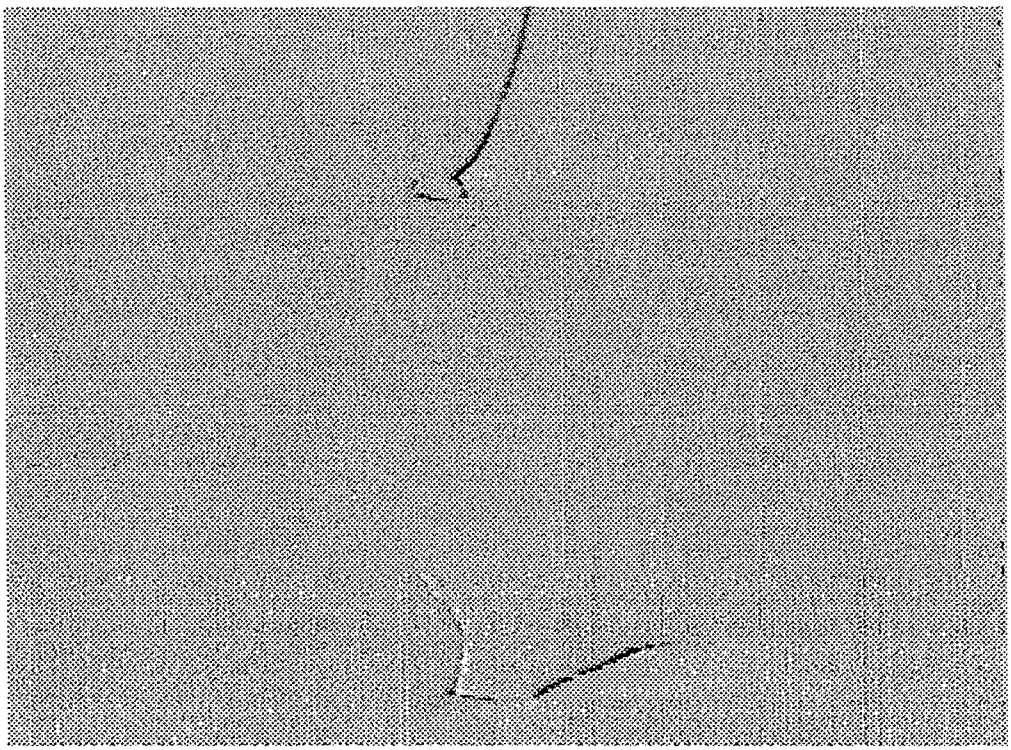

Figure 1 : Collection wire view (top) and induction wire view (bottom) of a cosmic-ray stopping muon observed in the 3-ton ICARUS prototype. The subsequent decay into an electron is clearly visible.

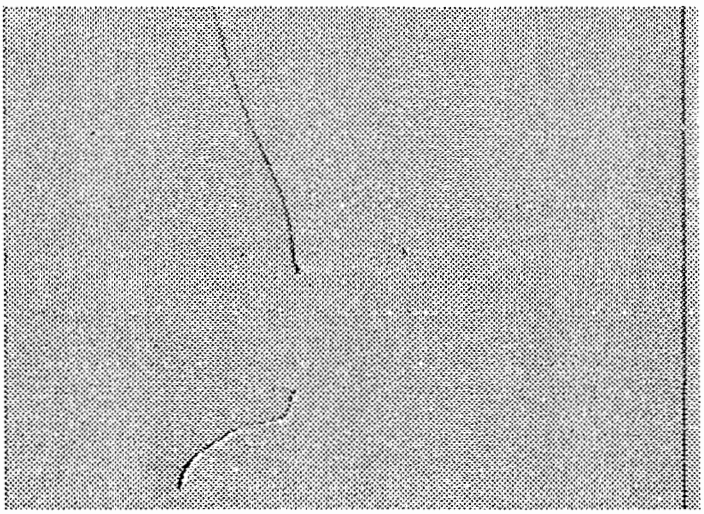

Figure 2 : Collection-wire view (top) and induction-wire view (bottom) of a cosmic-ray stopping muon observed in the 3-ton ICARUS prototype. This muon is then captured by an argon nucleus before it can decay into an electron, it is therefore a μ^-.

The rate for the μ^- capture process by nuclei of different charge was first calculated by Primakoff [1] and measured for the first time by J.C. Sens [2] where he measured the capture rate Z_{eff} and the Pauli suppression term for various nuclei. A detailed review of results on muon capture can be found in the work of C. Rubbia [3]. A specific measurement for argon was performed in 1973 by A. Bertin et al. [4] who obtained: W = (1.20 ± 0.08)× 10^6 s^{-1}.

As a result the probability of capture of a μ^- in argon is found to be:

$$P_{cap} = \frac{W_{cap}}{W_{cap} + W_{decay}} = 0.725^{+0.013}_{-0.014}$$

where W_{decay} is the muon decay rate taken as $4.55 \times 10^5 s^{-1}$. It has been argued that atomic binding modifies the decay rate of muons, however, even though the effect has been observed experimentally [5] it remains small and the corrections do not exceed a few per cent. If we take 5% as an upper limit in the case of argon, the probability of capture would only increase from 72.5% to 73%.

The capture probability for muons stopping in liquid argon has been confirmed by our study of cosmic ray events in our 3-ton prototype.

We conclude that the discrimination of μ^+ from μ^- from the behaviour in liquid argon will be a useful tool in the study of atmospheric neutrinos.

ICARUS may even go one step further in trying also to distinguish ν_e from $\bar{\nu}_e$, which could be done if e^+'s can be distinguished from e^-'s. Knowing that most cosmic muon decays observed in our prototype detector are due to μ^+'s, we decided to use them as a source of e^+'s. We searched for annihilation of a decay e^+ with an e^- from the argon atom, forming positronium at rest which then decays into two 511 keV photons back-to-back with respect to the location of the positronium. The attenuation length of 511 keV photons in argon is 8.6 cm. Therefore we expect to find, within a sphere of about 15 cm radius, Compton electrons around the point where an e^+ came to rest in the

liquid argon. These Compton electrons should be aligned with the point where the e^+ came to rest and annihilated. Indeed we find such events (Figure 3), and even though we have not yet made a full study of the efficiency, we believe that it will be possible to recognise $\bar{\nu}_e$ events from ν_e events, at least in part of the cases.

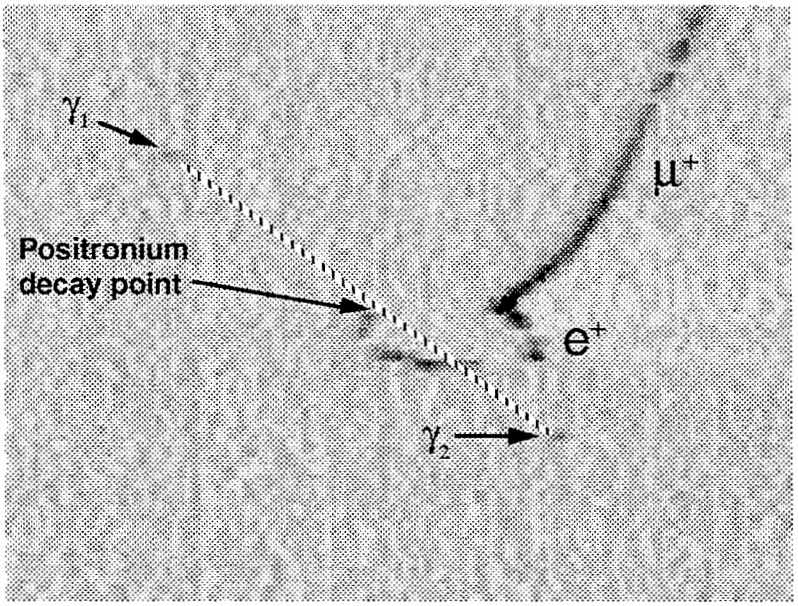

Figure 3 : This is the same cosmic stopping muon event as the one of Figure 1, but the view has been enlarged to show the subsequent decay of positronium into two photons. Compton electrons γ_1 and γ_2 are respectively 5.2 and 4.4 cm away from the point where the positronium decayed.

The ICARUS liquid argon TPC is a truly modern version of the bubble chamber, where redundancy is available to allow event identification without background. Equipped with such a powerful tool, we expect spectacular progress in the search for proton decay and in the study of the solar neutrino puzzle.

15. References

[1] H. Primakoff, Theory of Muon Capture, Rev. Mod. Phys., **31** (1959) 802.

[2] J.C. Sens, Capture of Negative Muons by Nuclei, Phys. Rev. **113** (1959) 679.

[3] C. Rubbia, Weak Interaction Physics, *in* E.H.S. Burhop (ed.), High Energy Physics, vol. 3, p. 308, Academic, New York, 1969.

[4] A. Bertin et al., Nuclear Capture of Muons in Argon and Neon, Phys. Rev. **A7**, Comments and Addenda, (1973) 2214.

[5] R. A. Lundy et al., Experimental Evidence for the Influence of Atomic Binding on the Decay Rate of Negative Muons, Phys. Rev. Lett. **3** (1958) 102.

VI. CONCLUSION

The overall conclusion of Volume I of the ICARUS proposal for Gran Sasso may be summarized in a few statements.

1) The R&D phase of ICARUS has been very successful, demonstrating that a new tool for detecting cosmic and rare underground signals is available. It represents a technological breakthrough; it is essentially an electronic 'bubble chamber'. The device can be triggered from the event information itself, it is continuously sensitive and a precise ionization measurement improves the particle identification capability and makes it possible to determine, in addition, the direction of particles.

For all physics issues under consideration ICARUS is a truly second-generation experiment.

2) The physics programme is unique in that it addresses several of the most fundamental issues of modern high-energy physics: proton decay will test unification theories and open a new window on the physics of the early universe; atmospheric neutrino, long baseline neutrino (with a CERN neutrino beam) and solar neutrino studies are concerned with the nature of some of the main building blocks of matter. In addition cosmological studies, such as the observation of supernova or any unexpected source of neutrinos, can be performed.

The proton decay study by ICARUS is complementary to the Superkamiokande approach. The larger mass of the water-Cherenkov detector is compensated by the high-resolution imaging technique allowing physics at the single-event level.

If the MSW mechanism is relevant for the solar neutrino deficit, it should also occur for atmospheric neutrinos interactions with the Earth. ICARUS will perform the first high-resolution imaging study of atmospheric neutrino events whose energy range is particularly well suited for the detection technique used.

Our point of view is that the proton decay search, atmospheric and long baseline neutrino studies constitute by themselves a strong motivation to build the large-scale detector planned for installation in Hall C at the Gran Sasso Underground Laboratory as soon as possible.

The direct observation of solar neutrinos and supernova neutrinos are all additional bonuses from the above priority programme.

It should also be noted that further improvements of the present analysis should come from our ongoing study of determination of the charge of the stopping muons and of the electrons observed in ICARUS.

3) The physics programme for ICARUS at Gran Sasso is now well defined. The scientific impact of the new detector technology developed has been evaluated in detail. The engineering design for the Gran Sasso detector is in preparation and will be described in Volume II of this proposal.